NASA/TM–20240012670
NESC-RP-19-01468

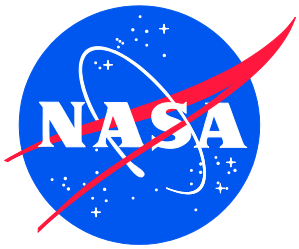

Commercial Crew Program (CCP) Post-flight Reference Radiation Environments

Christopher J. Mertens
Langley Research Center, Hampton, Virginia

Guillaume P. Gronoff
Science Systems and Application Inc., Hampton, Virginia

Yihua Zheng
Goddard Space Flight Center, Greenbelt, Maryland

Janessa Buhler
Kennedy Space Center, Florida

Emily Willis
Marshall Space Flight Center, Huntsville, Alabama

Maksym Petrenko
Goddard Space Flight Center, Greenbelt, Maryland

Daniel Phoenix
Analytical Mechanics Associates, Hampton, Virginia

Chinwe Didigu
Adnet Services, Inc.. Reading, Pennsylvania

Insoo Jun
Jet Propulsion Laboratory, Pasadena, California

Joseph Minow/NESC
Marshall Space Flight Center, Huntsville, Alabama

October 2024

NASA STI Program Report Series

Since its founding, NASA has been dedicated to the advancement of aeronautics and space science. The NASA scientific and technical information (STI) program plays a key part in helping NASA maintain this important role.

The NASA STI program operates under the auspices of the Agency Chief Information Officer. It collects, organizes, provides for archiving, and disseminates NASA's STI. The NASA STI program provides access to the NTRS Registered and its public interface, the NASA Technical Reports Server, thus providing one of the largest collections of aeronautical and space science STI in the world. Results are published in both non-NASA channels and by NASA in the NASA STI Report Series, which includes the following report types:

- TECHNICAL PUBLICATION. Reports of completed research or a major significant phase of research that present the results of NASA Programs and include extensive data or theoretical analysis. Includes compilations of significant scientific and technical data and information deemed to be of continuing reference value. NASA counterpart of peer-reviewed formal professional papers but has less stringent limitations on manuscript length and extent of graphic presentations.

- TECHNICAL MEMORANDUM. Scientific and technical findings that are preliminary or of specialized interest, e.g., quick release reports, working papers, and bibliographies that contain minimal annotation. Does not contain extensive analysis.

- CONTRACTOR REPORT. Scientific and technical findings by NASA-sponsored contractors and grantees.

- CONFERENCE PUBLICATION. Collected papers from scientific and technical conferences, symposia, seminars, or other meetings sponsored or co-sponsored by NASA.

- SPECIAL PUBLICATION. Scientific, technical, or historical information from NASA programs, projects, and missions, often concerned with subjects having substantial public interest.

- TECHNICAL TRANSLATION. English-language translations of foreign scientific and technical material pertinent to NASA's mission.

Specialized services also include organizing and publishing research results, distributing specialized research announcements and feeds, providing information desk and personal search support, and enabling data exchange services.

For more information about the NASA STI program, see the following:

- Access the NASA STI program home page at http://www.sti.nasa.gov

- Help desk contact information:

https://www.sti.nasa.gov/sti-contact-form/
and select the "General" help request type.

NASA/TM–20240012670
NESC-RP-19-01468

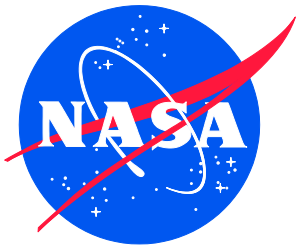

Commercial Crew Program (CCP) Post-flight Reference Radiation Environments

Christopher J. Mertens
Langley Research Center, Hampton, Virginia

Guillaume P. Gronoff
Science Systems and Application Inc., Hampton, Virginia

Yihua Zheng
Goddard Space Flight Center, Greenbelt, Maryland

Janessa Buhler
Kennedy Space Center, Florida

Emily Willis
Marshall Space Flight Center, Huntsville, Alabama

Maksym Petrenko
Goddard Space Flight Center, Greenbelt, Maryland

Daniel Phoenix
Analytical Mechanics Associates, Hampton, Virginia

Chinwe Didigu
Adnet Services, Inc.. Reading, Pennsylvania

Insoo Jun
Jet Propulsion Laboratory, Pasadena, California

Joseph Minow/NESC
Marshall Space Flight Center, Huntsville, Alabama

National Aeronautics and
Space Administration

Langley Research Center
Hampton, Virginia 23681-2199

October 2024

Acknowledgments

The NAIRAS model extension from the atmosphere to space and the transition of the model to the NASA Goddard Space Flight Center's (GSFC's) CCMC were funded by the NESC assessment TI-19-01468. The improvements in solar energetic particle (SEP) event spectral fitting and geomagnetic vertical cutoff rigidity modeling were funded by the NASA Science Mission Directorate, Heliophysics Division, Space Weather Science Applications Program. Data sources used in developing and running the model are credited in Appendix A.

The team thanks Elliott Cramer, Steven Gentz, Robert Hodson, Heather Koehler, Peter Panetta, and Sara Wilson of the NESC and Paul O'Brien/Aerospace Corporation and Kent Tobiska/Space Environment Technologies for valuable comments provided during the peer review of this report.

Available from:

NASA STI Program / Mail Stop 050
NASA Langley Research Center
Hampton, VA 23681-2199

NASA Engineering and Safety Center
Technical Assessment Report

Commercial Crew Program (CCP) Post-flight Reference Radiation Environments

TI-19-01468

Dr. Joseph I. Minow, NESC Lead
Dr. Insoo Jun, Technical Lead

August 8, 2024

Report Approval and Revision History

NOTE: This document was approved at the August 8, 2024, NRB.

Approved: Timmy Wilson Digitally signed by Timmy Wilson Date: 2024.08.27 18:19:05 -04'00' _____

NESC Director

Version	Description of Revision	Office of Primary Responsibility	Effective Date
1.0	Initial Release	Joseph I. Minow, NASA Technical Fellow for Space Environments, MSFC	08/08/2024

Table of Contents

List of Figures

List of Tables

Technical Assessment Report

1.0 Notification and Authorization

Commercial Crew Program (CCP) contractors conduct pre-flight radiation evaluations required to predict the number of single event effects (SEE) and total ionizing dose (TID) expected during a mission. Radiation environment inputs to these analyses are derived from conservative design environments with a goal to assure that vehicle avionics can meet performance requirements during a mission. CCP is interested in comparing pre-flight TID and SEE evaluations with observations during flight and post-flight analyses using the actual radiation environment experienced by hardware on CCP vehicles during the mission. Flight data from radiation sensors are not always available for the CCP vehicles, so an alternative approach using space weather tools is required to provide the post-flight radiation environments. CCP requested a NASA Engineering and Safety Center (NESC) technical assessment to provide access to appropriate tools capable of providing the flight radiation environment data required for CCP contractors to conduct post-flight radiation assessments.

This assessment was approved to proceed with an Out of Board on July 18, 2019. The assessment plan was approved at the NESC Review Board (NRB) on March 19, 2020.

The key stakeholders are Steve Sullivan, CCP Chief Engineer. The operational Nowcast of Aerospace Ionizing RAdiation System (NAIRAS) model deployed at the Community Coordinated Modeling Center (CCMC) by this assessment team can also be used by any NASA spaceflight, suborbital flight, and atmospheric flight programs and project operating in the Earth's upper atmosphere and low Earth orbit (LEO) to obtain best estimates of the radiation environments encountered during their flights.

2.0 Signatures

Significant Contributors:

CHRISTOPHER MERTENS
Digitally signed by CHRISTOPHER MERTENS
Date: 2024.08.21 19:32:52 -04'00'

Dr. Christopher Mertens

Signature and concurrence received via email dated 08/16/2024, attached.

Dr. Guillaume Gronoff

YIHUA ZHENG
Digitally signed by YIHUA ZHENG
Date: 2024.08.23 12:38:43 -04'00'

Dr. Yihua Zheng

Janessa Buhler
Digitally signed by Janessa Buhler
Date: 2024.08.22 09:19:59 -04'00'

Ms. Janessa Buhler

EMILY WILLIS
Digitally signed by EMILY WILLIS
Date: 2024.08.21 18:10:44 -05'00'

Dr. Emily Willis

Maksym Petrenko
Digitally signed by Maksym Petrenko
Date: 2024.08.22 10:25:15 -04'00'

Dr. Maksym Petrenko

Signature and concurrence received via email dated 08/19/2024, attached.

Dr. Daniel Phoenix

Chinwe Didigu (affiliate)
Digitally signed by Chinwe Didigu (affiliate)
Date: 2024.08.20 10:04:18 -04'00'

Ms. Chinwe Didigu

Submitted by:

Jun, Insoo
Digitally signed by Jun, Insoo
Date: 2024.08.24 08:54:17 -07'00'

Dr. Insoo Jun, Technical Lead

Joseph Minow
Digitally signed by Joseph Minow
Date: 2024.08.26 06:42:24 -05'00'

Dr. Joseph Minow, NESC Lead

Signatories declare the findings, observations, and NESC recommendations compiled in the report are factually based from data extracted from program/project documents, contractor reports, and open literature, and/or generated from independently conducted tests, analyses, and inspections.

3.0 Team Members

Name	Discipline	Organization (include host Center)
Core Team		
Joseph Minow	NESC Lead	LaRC/NESC
Insoo Jun	Technical Lead	JPL
Christopher Mertens	Space Radiation, NAIRAS Principle Investigator	LaRC
Guillaume Gronoff	NAIRAS Software	LaRC/RSES
Daniel Phoenix	NAIRAS Software	LaRC/RSES
Yihua Zheng	Space Weather Modeling	GSFC
Maksym Petrenko	Space Weather Modeling	GSFC
Chinwe Didigu	Space Weather Modeling	GSFC/Adnet Systems Inc.
Emily Willis	Space Environments	MSFC
Janessa Buhler	Space Environments	KSC
Business Management		
Laura Evans	Program Analyst	LaRC/MTSO
Assessment Support		
Melissa Strickland	Project Coordinator	LaRC/AMA
Linda Burgess	Planning and Control Analyst	LaRC/AMA
Dee Bullock	Technical Editor	LaRC/AMA

3.1 Acknowledgements

The NAIRAS model extension from the atmosphere to space and the transition of the model to the NASA Goddard Space Flight Center's (GSFC's) CCMC were funded by the NESC assessment TI-19-01468. The improvements in solar energetic particle (SEP) event spectral fitting and geomagnetic vertical cutoff rigidity modeling were funded by the NASA Science Mission Directorate, Heliophysics Division, Space Weather Science Applications Program. Data sources used in developing and running the model are credited in Appendix A.

The team thanks Elliott Cramer, Steven Gentz, Robert Hodson, Heather Koehler, Peter Panetta, and Sara Wilson of the NESC and Paul O'Brien/Aerospace Corporation and Kent Tobiska/Space Environment Technologies for valuable comments provided during the peer review of this report.

4.0 Executive Summary

The Nowcast of Aerospace Ionizing RAdiation System (NAIRAS) model is a real-time, global, physics-based model originally developed to predict exposure from cosmic radiation to air travelers from both galactic and solar sources. A prototype operational NAIRAS model has provided tabular and graphical data products via its public web site for about 10 years. The new version 3 of the NAIRAS model has been developed that incorporates an extension of the model domain from the atmospheric ionizing radiation environment to the space radiation environment. The new modeling components of NAIRAS version 3 include the addition of trapped radiation belt proton (TRP-p) and electron (TRP-e) sources, an altitude-dependent and rigidity-dependent geomagnetic shielding of galactic cosmic rays (GCR) and solar energetic particles (SEP), and a SEP heavy-ion model. New output products of differential and integral particle flux have been developed for the characterization of single-event effects (SEE), expanding the application of NAIRAS from human radiation exposure assessment to allowing end-users to quantify radiation environment risks to aviation and spacecraft microelectronic systems. The NAIRAS model has transitioned to prototype operations at the Community Coordinated Modeling Center (CCMC) where the model now operates in two modes: 1) real-time global predictions of the atmospheric radiation environment, and 2) a run-on-request (RoR) service allowing the user to select a specific time period for the global dosimetric calculations, or to upload an aircraft, balloon, or spaceflight trajectory file to provide predictions of the dosimetric and particle flux quantities along the flight path. The new features of NAIRAS version 3 are described in this report and example results of the new output products for low Earth orbit (LEO), medium Earth orbit (MEO), and cislunar radiation environments are presented. The impact of the new features of NAIRAS version 3 are summarized below.

The development of NAIRAS version 3 has led to significant model accuracy improvements, revealed new insights into the space radiation environment, and greatly expanded the applications and user base of the model. The comparisons of NAIRAS with dosimeter measurements taken during the NASA Radiation Dosimetry Experiment (RaD-X) flight campaign led to improvements in the atmospheric ionizing radiation transport procedure which reduced the uncertainty in the model to below 30% at altiudes from 0 to 40 km. Preliminary validation studies at LEO and MEO are very engouraging, which have shown that the model uncertainty for daily dose rates is less than 60%. The new SEP spectral fitting algorithm is also an important model improvement, and the excellent agreement between NAIRAS predictions and dosimeter measurements at LEO during the June 2015 SEP event is the first validation of NAIRAS during a SEP event. The development of the SEP heavy-ion model component showed that the heavy-ions contribute significantly (~40%) to the total SEP effective dose at large depths (50 g/cm^2) within the International Space Station (ISS) for approximately one half of the top ten largest SEP events, and contribute a factor of 2 to 3 to the total SEP effective dose for astronaut extravehicular activity (EVA) exposure at LEO for all 10 of the largest SEP events. The integration of the TRP-e model into NAIRAS has shown that the outer belt TRP-e contribute to astronaut effective dose during EVA at LEO. The integration of the TRP-e model was also found to be necessary for validating and understanding NAIRAS model performance for much of the readily accessible dosimeter measurements in the geospace environment. The model validation studies have also revealed several areas of improvements needed in modeling the trapped radiation environment, in particular.

The primary products and deliverables generated by this assessment are the real-time and RoR versions of the improved NAIRAS code deployed on the CCMC servers where they are available for use by the Commercial Crew Program (CCP), other NASA programs, and users external to NASA. In addition, the assessment team identified 12 findings and 2 observations that led to 5 topics for future NAIRAS Software team work that would improve the NAIRAS code.

The next phase of NAIRAS model development will focus on providing a real-time capability to support ISS operations for astronaut EVA, especially during SEP events. Future efforts will also be directed at extensive validation studies, with the aim of improving the various model components of NAIRAS. The preliminary validation results shown in this paper for LEO and MEO are encouraging. Different approaches to improving the trapped proton and electron environments have been identified. Validation studies and analysis in future work will also include comparing NAIRAS to the Hybrid Electronic Radiation Assessor (HERA) dose measurements onboard the Artemis 1 flight.

The NESC team has published two peer-reviewed journal papers, one NASA Technical Publication, and has given numerous presentations at scientific conferences, workshops, and technical meetings, such as Mertens et al. (2023a, 2023b, 2024) and the presentations listed in Section 13.0. Nearly 400 NAIRAS RoR jobs were submitted from the CCMC interface in 2023. The RoR jobs were submitted by national and international users for both human radiation exposure and SEE applications at altitudes from commercial aviation flight levels to near geostationary orbit.

5.0 Assessment Plan

The NESC assessment team modified NASA's existing NAIRAS radiation environment model, originally developed for computing radiation dose for aviation flight crews, to provide the reference radiation environments for CCP flights. The NAIRAS model uses real-time radiation data from satellites and other space and terrestrial environment data to constrain the GCR and SEP environments at locations within the temporally and spatially dependent radiation shielding provided by the Earth's atmosphere and geomagnetic field.

Original NAIRAS output before the changes implemented in this assessment was dose rate in aircraft and crew along flight trajectory, which can be used by CCP to evaluate shielding analysis applications. In addition to the original dosimetric outputs which are retained in the updated version of NAIRAS, the CCP needs charged-particle flux and fluence as a function of energy and linear energy transfer (LET) along a user-provided flight trajectory to evaluate TID and SEE rates.

The NESC team implemented NAIRAS in a stable, operational environment at the CCMC and modified the software to give tailored output in formats required for input to CCP contractor radiation analysis tools. Modification of the NAIRAS model was the responsibility of NASA Langley Research Center (LaRC) space radiation personnel who were the developers of the original NAIRAS model. The NAIRAS code deployment at the CCMC was the responsibility of CCMC personnel with experience in deploying complex space science and operational space weather models. In addition, the CCMC has developed extensive tool sets for interrogating complex model outputs that were utilized in providing options for users to access and post-process NAIRAS model outputs.

6.0 Problem Description and Background

The NAIRAS is composed of coupled physics-based models that transport cosmic radiation through the heliosphere, Earth's magnetosphere, the neutral atmosphere, and aircraft or spacecraft shielding. Two extraterrestrial sources of ionizing radiation are included: 1) ubiquitous GCRs originating from outside the solar system, and 2) SEPs originating from transient solar storm events (Mertens et al., 2010a, 2012, 2013). The transport through the magnetosphere incorporates the dynamical response of the geomagnetic field to space weather variability in the interplanetary medium (Kress et al., 2010; Mertens et al., 2010a). Transport of cosmic radiation through material media (i.e., the atmosphere and/or aircraft or spacecraft shielding) is calculated with the deterministic High charge (Z) and Energy TRaNsport (HZETRN) code (Wilson et al., 1991, 2005; Slaba et al., 2020b). Thus, the NAIRAS model computes ionizing radiation particle flux spectra from the primary sources and the secondary radiations produced from nuclear interactions between the radiation source ions and the constituents of the intervening material media. The secondary particles consist of heavy-ion fragments from GCR and SEP ions, projectile and target light-ions, neutrons, pions and muons, and electromagnetic cascade particles (i.e., electrons, positrons, and gamma ray photons) (Mertens, 2016a) produced by interactions of the material media with both GCR and SEP primary particles. Secondary electromagnetic particles are also produced by interactions between the TRP-p and TRP-e and the intervening material media. The particle flux spectra are the fundamental physical quantities from which important response functions are calculated (e.g., dosimetric quantities and various flux quantities) that are useful for characterizing SEE.

The NAIRAS model was originally developed to provide real-time predictions of dosimetric quantities to quantify human radiation exposure at aviation altitudes (Mertens et al., 2010a, 2012, 2013). The model has been running on the LaRC computer cluster and output graphical and tabular data products are hosted on Space Environment Technologies, Inc. server/website (http://sol.spacenvironment.net/~nairas/). The key features of the real-time NAIRAS model are: 1) global maps of characteristics of the atmospheric ionizing radiation environment are provided at an hourly cadence on a 1x1 degree latitude/longitude grid, 0 to 90 km in altitude at 1-km increments; 2) both GCR and SEP sources of atmospheric ionizing radiation are included in real-time; 3) computation of radiation transport through material media is physics based using the deterministic HZETRN code; and 4) the temporal and spatial variations in geomagnetic transmission of GCR and SEP primary particle spectra due to coupling between the magnetosphere and the interplanetary plasma environment are also included in real time.

The focus of this report is the description of the new developments incorporated into NAIRAS version 3. The model altitude domain has been extended above the neutral atmosphere into the geospace and free-space radiation environments for the assessment of SEE in spacecraft microelectronic systems. The model domain extension necessarily required the addition of a TRP-p model to the suite of NAIRAS radiation environment model components. Moreover, in the geospace environment the vertical cutoff rigidity alone is not adequate to parameterize the geomagnetic transmission of free-space GCR and SEP primary particle spectra through the magnetosphere, which is the customary approximation for the atmospheric ionizing radiation environment. Thus, the NAIRAS model was updated to include an altitude-dependent and rigidity-dependent geomagnetic transmission function. New differential and integral flux quantities have been developed and added to the model output for the characterization of SEE. Thus, the new output quantities have expanded the application of the NAIRAS model from human radiation exposure assessments to the quantification of radiation effects on spacecraft microelectronic systems (Mertens et al.,2023a). Since the time of that paper, the SEP heavy-ion and TRP-e belt model components have been added to NAIRAS. SEP heavy-ions are important for predicting both human radiation exposure and SEE assessment in the geospace and free-space environments. The TRP-e belt model is important for assessing astronaut radiation exposure during EVAs in LEO and validating the NAIRAS model against measurements obtained from lightly shielded detectors in geospace. Thus, this paper provides a complete description of NAIRAS version 3. The NAIRAS code has been transitioned to prototype operations at the CCMC where the new version 3 capabilities are available to the public (Mertens et al., 2023b).

The new developments in NAIRAS version 3 are presented in the remainder of the report. The new data products for SEE assessment and the user interface are described in more detail in Section 7. The model improvements and enhancements are summarized in Section 8. Examples of the new output quantities for LEO, MEO, and cislunar spaceflight trajectories are presented in Section 9. Summary and conclusions are provided in Section 10.

7.0 NAIRAS Output Products and User Interface

The NAIRAS code has been transitioned to prototype operations at CCMC where the model operates in two independent modes: 1) real-time global predictions of the atmospheric radiation environment, which are updated hourly, and 2) a RoR capability allowing the user to select a specific time period for the global dosimetric calculations, or to upload an aircraft, balloon, or

spaceflight trajectory file to provide simulations of the dosimetric and particle flux quantities along the input flight path. The NAIRAS RoR service operates in quasi real-time in the sense that the RoR job can be submitted for a flight that occurred the previous day.

The graphical products from the real-time, global operation mode are available via the CCMC Integrated Space Weather Analysis System (iSWA). A screenshot of an example of the NAIRAS real-time products from iSWA is shown in Figure 1.

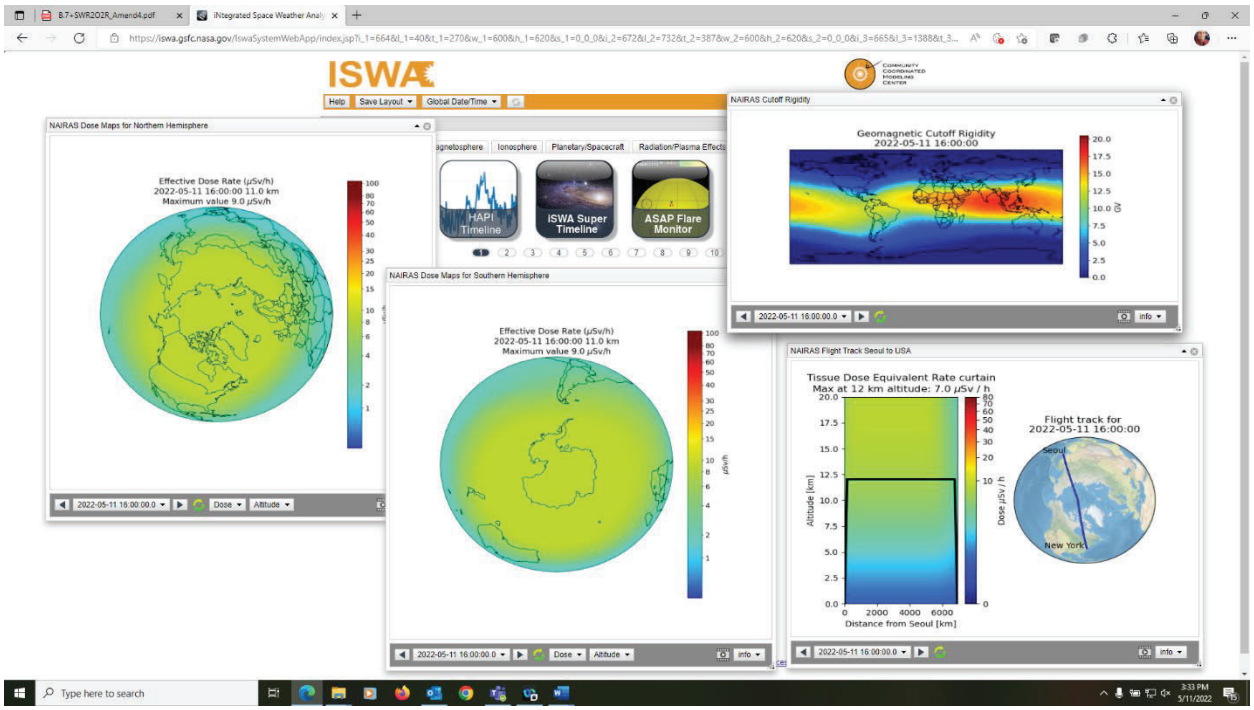

Figure 1. Screenshot of example NAIRAS real-time graphical products at CCMC/iSWA located under the Radiation/Plasma Effects tab (https://iswa.gsfc.nasa.gov/IswaSystemWebApp/). The left panel is northern hemisphere effective dose rate (μSv/h). The bottom center panel is southern hemisphere effective dose rate (μSv/h). The upper right panel is vertical geomagnetic cutoff rigidity (GV). The right bottom panel shows a vertical slice of dose equivalent rate (μSv/h) for a high-latitude commercial flight from New York, New York USA to Seoul, South Korea.

The left panel in Figure 1 is effective dose rate over the northern hemisphere for a representative hourly prediction. Dose rates from a southern hemisphere view are also shown in the bottom center panel. The user can select prior hourly predictions going back to year 2020 when NAIRAS became operational at iSWA. The user can select five dosimetric quantities: absorbed dose in silicon, absorbed dose in tissue, dose equivalent, ambient dose equivalent, and effective dose. The definitions of these quantities and their relevance in characterizing the ionizing radiation environment are summarized in Mertens (2016a). The user can select five barometric altitudes for displaying the dosimetric quantities: 5 km, 11 km, 15 km, 20 km, and 40 km. The cruising altitude of small aircraft and commercial flights are largely bound by the altitude range 5 to 11 km. Corporate aircraft cruising altitudes are typically between 12 and 15 km. High-flying military aircraft operate at approximately 20 km. The highest altitude of 40 km provides a reasonable proxy for free-space ionizing radiation exposure behind the typical shielding of an aircraft/spacecraft (~ 3 to 5 g/cm^2 aluminum-equivalent (Singleterry et al., 1999; Hu et al., 2009; Townsend et al., 2018), which when converted to an equivalent atmospheric depth corresponds

to ~ 40 km in the U.S. Standard Atmosphere. The upper right panel is the vertical geomagnetic cutoff rigidity for the representative hourly dose predictions in this example. The right bottom panel is a vertical slice of dose equivalent rate for a commercial flight from New York, USA to Seoul, South Korea.

The RoR capability allows the user to run the NAIRAS model for customized application scenarios and time periods. These features are summarized in Table 1. The global dosimetric run option mirrors the execution of the real-time mode of the NAIRAS model for a user-specified time period. The input is simply start and end datetime for the model run. The output quantities are the same five dosimetric quantities provided by the real-time run mode. Hourly output files of the dosimetric quantities calculated at each model grid point described previously are written out over the duration of the user-input start/end datetime interval. For SEP events, the user has the option to select a few pre-defined higher-resolution time intervals (e.g., 5 minutes, 15 minutes, and 30 minutes). This class of run option capability provides global context and situational awareness of the atmospheric ionizing radiation environment. Furthermore, retrospective scientific analysis and verification and validation of the NAIRAS model real-time mode can be readily performed.

Table 1. RoR Capability Summary and Description

Run Option	Output Quantities		User Input
Global Dosimetric	Absorbed dose in silicon, absorbed dose in tissue, dose equivalent, ambient dose equivalent, effective dose		Start/End Date-Time
Flight Trajectory	**Dosimetric and Flux/Fluence**		Trajectory file (date/time/lat/lon/alt)
	Dosimetric	Same as above	Shielding depths for dosimetric calculations
	Flux/Fluence		Shielding depths for flux/fluence calculations
		Integral • GCR/SEP LET • SEP proton • TRP-p proton • TRP-e electron	Lower LET/energy bounds
		Differential • GCR/SEP LET • TRP-(p/e) LET • SEP proton • TRP-p proton • TRP-e electron	N/A (full model differential spectra written to output)

The RoR flight trajectory run option allows the user to upload a trajectory file. The model output products are calculated at each trajectory point. Also available to the user are the output quantities time-integrated over the duration of the flight. The trajectory file can correspond to an aircraft, balloon, or spacecraft flight. The key input fields of the trajectory file are: date, time, geographic latitude and longitude, and altitude. The datetime format of the trajectory file can be either Gregorian or modified Julian datetime. The user can select any combination of dosimetric, differential, integral, and flux/fluence quantities listed in the Table 1. The dosimetric outputs are

the same five quantities available from the real-time NAIRAS operation mode or from the RoR global dosimetric run option. The flux and fluence output products are quantities useful for assessing SEE and validating the model. Differential and integral LET flux and fluence quantities are calculated from both GCR and SEP radiation sources. These quantities are useful since heavy-ion SEE cross sections are typically parameterized as a function of LET. TRP-p and TRP-e differential and integral LET flux and fluence quantities are also included for model validation against LET spectral measurements. Differential and integral proton flux and fluence quantities are calculated from the SEP and TRP-p radiation sources, and differential and integral electron flux and fluence quantities are calculated from the TRP-e radiation source. For the calculation of the integral LET (GCR/SEP) and integral particle (SEP/TRP-p/TRP-e) flux and fluence quantities, the user can select as many output quantities as desired, which are defined by the user-specified threshold LET (GCR/SEP) or proton (SEP/TRP-p) or electron (TRP-e) energy of the associated integral quantity.

Moreover, for the RoR flight trajectory run option, the user can input as many aluminum-equivalent shielding depths as needed for the selected output quantities calculated by the model. Two separate sets of shielding depths can be specified for the dosimetric and flux/fluence quantities. The two sets of shielding depths help efficiently manage the amount of model output data. There are typically a limited number of shielding depths required for dosimetric quantities corresponding to crew and/or onboard dosimeter locations. However, there may be many radiation-sensitive electronic components for which the user needs to compute the flux/fluence quantities at the individual component shielding depths. The flux/fluence quantities provide the key radiation environment inputs to SEE assessment models. Thus, these two sets allow detailed model comparisons to onboard dosimeters or crew member locations, characterized by unique shielding environments, and radiation environment characterization at the shielded location of individual microelectronic components via the flux/fluence quantities that can be imported into SEE assessment applications.

8.0 NAIRAS Model Improvements

The NAIRAS model updates and enhancements in version 3 are described in this section. For each model component, a summary of the previous version is given followed by a more detailed description of the new features and improvements. The key model components are described in the subsections, which are ordered according to the chain of transport and interactions from radiation source to output radiation response functions. The sources and management of the input data driving the model components are described in Appendix A.

8.1 Radiation Source Modules

The NAIRAS model now incorporates four ionizing radiation sources: the extraterrestrial GCR and SEP sources included in the previous version, and the terrestrial TRP-p and TRP-e added in version 3. In addition, the SEP heavy-ion model is a new component in version 3. The model components specifying these four radiation sources are described in the following sections.

8.1.1 Galactic Cosmic Rays

In the NAIRAS model, GCR ions are propagated from outside the heliosphere to 1 AU (astronomical unit) by solving a steady-state, convective-diffusive transport equation including adiabatic energy loss. A hybrid version of the Badhwar and O'Neill 2010 model (O'Neill, 2010), denoted H-BON10, was developed for NAIRAS to solve GCR heliospheric transport (Mertens et

al., 2013). The composition of the GCR gas in the Badhwar and O'Neill model consists of 28 fully ionized nuclear isotopes from hydrogen (Z = 1, A = 1) through nickel (Z = 28, A = 58). The key transport parameter in H-BON10 is the ratio of the diffusion coefficient to the solar wind velocity, in which the time dependence of this ratio is embedded into the so-called solar modulation potential (SMP).

The H-BON10 SMP is parameterized in terms of real-time ground-based neutron monitor count rates obtained from four high-latitude stations. These site are Thule (77.5°N, 290.5°E, R_{vc} = 0.0 GV, where R_{vc} refers to vertical cutoff rigidity), Oulu (65.0°N, 25.5°E, R_{vc} = 0.4 GV), Izmiran (55.5°N, 37.3°E, R_{vc} = 1.7 GV), and Lomnicky (49.2°N, 20.2°E, R_{vc} = 2.8 GV). The SMP is computed using count rates from the neutron monitor stations via derived linear fit coefficients (Mertens et al., 2013). The SMP is dependent on the large-scale structure of the interplanetary magnetic field carried by the solar wind. Thus, the fit coefficients between the SMP and the neutron monitor count rates were derived for solar polar magnetic field polarity states : 1) positive solar cycle (outward directed northern polar field), 2) negative solar cycle (inward directed northern polar field), and 3) transition state (intermediate between positive and negative polarities with high degree of variability). The polarity state of the solar polar magnetic field is determined from field measurements taken by the Wilcox Solar Observatory (WSO) for time periods after 1975. Prior to 1975, the polarity state was determined from sunspot number and the definition of the Hale cycle (Mertens et al., 2013).

Measurements from the satellite-born Payload for Antimatter Exploration and Light-nuclei Astrophysics (PAMELA) experiment was used to derive a temporal-energy dependent correction to the GCR primary proton spectral flux in the H-BON10 model (Adriani et al., 2013). Correction factors were derived for two time periods from a quadratic fit in log energy to the H-BON10/PAMELA proton spectral flux ratio: 1) a time period used as a proxy for solar cycle maximum (November 13, 2006 – December 4, 2006), and 2) for a time period at solar cycle minimum (December 6, 2009 – January 1, 2010). The correction factors for the solar cycle maximum proxy ($r(E,t_{\max})$) and solar cycle minimum ($r(E,t_{\min})$) have the following mathematical form:

$$r(E,t_{\max}) = a_0 + a_1 \ln E + a_2 (\ln E)^2 \tag{1}$$

$$r(E,t_{\min}) = b_0 + b_1 \ln E + b_2 (\ln E)^2 \tag{2}$$

For an arbitrary phase of the solar cycle, the temporal energy-dependent correction factor is computed by a linear weighted average of the two factors in equations (1) and (2), such that:

$$r(E,t) = (1 - w(t)) r(E,t_{\min}) + w(t) r(E,t_{\max}), \tag{3}$$

where

$$w(t) = \frac{\Phi(t) - \Phi(t_{\min})}{\Phi(t_{\max}) - \Phi(t_{\min})}. \tag{4}$$

In equation (4), $\Phi(t)$ is the H-BON10 SMP. PAMELA alpha spectral flux measurements were also analyzed (Adriani et al., 2016). However, no significant differences between PAMELA and H-BON10 alpha spectral flux were found.

The PAMELA-based GCR primary proton spectral flux correction outlined in the previous paragraphs was derived after the initial H-BON10 development reported by Mertens et al. (2013) and prior to the new Badhwar and O'Neill 2020 GCR model (Slaba & Whitman, 2020a), denoted BON2020. A key advantage of the BON2020 model is that the SMP parameterization is calibrated to all the available GCR flux measurements prior to 2020, including PAMELA data that were not available at the time the GCR primary proton spectral flux correction factor in equation (3) was derived, and data from the ISS Alpha Magnetic Spectrometer (AMS-02). An important future update to the NAIRAS model is to develop a hybrid version of BON2020, H-BON2020, which is analogous to the development of H-BON10, that will involve cross correlating the BON2020 SMP with neutron monitor data so the BON2020 SMP can be parameterized in terms of the counts rates from the four high-latitude neutron monitor stations described at the beginning of this section and incorporated into the heliospheric GCR transport module of NAIRAS. Parameterizing the SMP in terms of the neutron monitor count rates enable the NAIRAS heliospheric GCR transport module to function in real-time and RoR version 3 operation modes.

The GCR composition of the H-BON10 model was also expanded in version 3 to calculate LET spectra out to 100 MeV-cm^2/mg, which is required in the assessment of SEE in the space radiation environment. The highest charge and heaviest nuclear isotope in all versions of the Badhwar and O'Neill model is nickel (Z = 28, A = 58), which can produce a maximum LET of 31.9 MeV-cm^2/mg. As a result, the composition of the H-BON10 model was extended beyond nickel to include the ultra-heavy GCR nuclear isotopes. The highest charge and heaviest isotope included in the expanded H-BON10 GCR model is uranium (Z = 92, A = 238), which can produce a maximum LET of 110.2 MeV-cm^2/mg. The composition of ultra-heavy GCR is based on the relative abundances reported by Mewaldt et al. (1988), which were ultimately based on analysis of measurements taken by the NASA High Energy Astrophysical Observatory (HEAO-3) and Ariel 6 satellite missions (Binns et al., 1982; Fowler et al., 1987). The relative abundances of the H-BON10 GCR composition are shown in Figure 2 as relative fluxes at a kinetic energy insensitive to solar modulation. Figure 3 is an example of the H-BON10 GCR spectral flux.

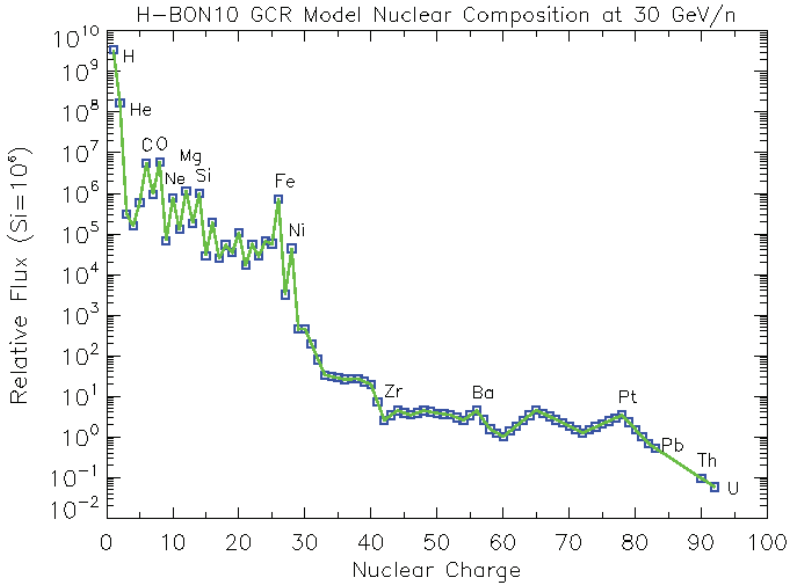

Figure 2. H-BON10 model GCR composition. Relative abundances represented as relative flux at 30 GeV/n, normalized to (silicon) Si = 10^6.

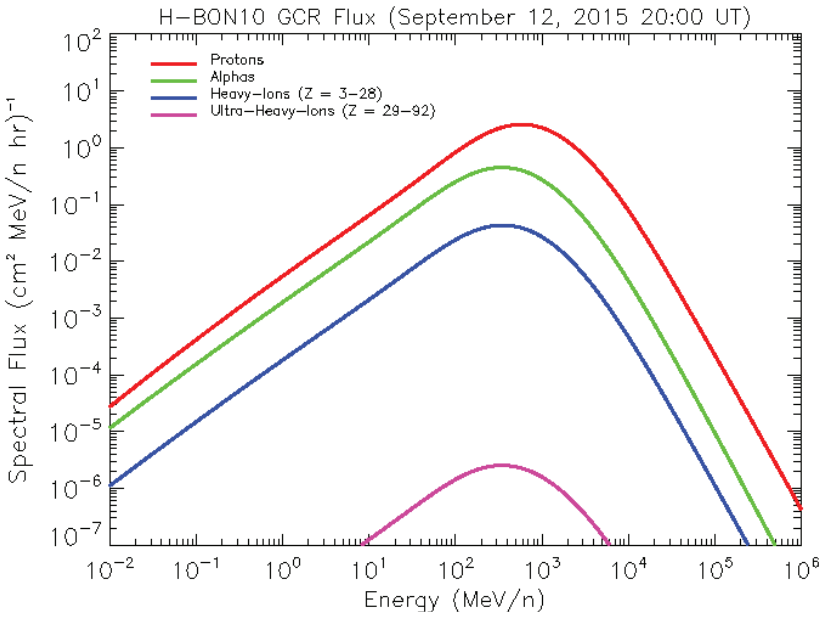

Figure 3. H-BON10 GCR spectral flux computed during the NASA RaD-X flight campaign.

8.1.2 Solar Energetic Particles

8.1.2.1 Protons

The SEP proton spectrum at 1 AU is determined by a fitting procedure using *in situ* measurements of proton flux from the National Oceanic and Atmospheric Administration (NOAA) Geostationary Operational Environmental Satellites (GOES). The spectral fitting algorithm fits analytical representations of the SEP proton spectrum to either GOES differential proton flux measurements (Mertens et al., 2012, 2010a) or GOES integral proton flux measurements, the latter of which is a new feature in version 3. The form of the analytical functions is guided by theoretical understanding of the origin, acceleration, and transport of energetic charged particles from their sources in the solar atmosphere through interplanetary space. The analytical forms are: equation (5) single power-law (Tylka & Lee, 2006), equation (6) Ellison-Ramaty (Ellison & Ramaty, 1985), equation (7) Ellison-Ramaty double power-law (Mewaldt et al., 2005; Tylka et al., 2005), sometimes referred to as a Band function, and equation (8) the Weibull distribution (Townsend et al., 2006, 2003; Xapsos et al., 2000), which are expressed as:

$$dJ / dE = CE^{-\gamma} \tag{5}$$

$$dJ / dE = CE^{-\gamma} \exp(-E / E_0) \tag{6}$$

$$\begin{aligned} dJ / dE &= CE^{-\gamma_a} \exp(-E / E_0) \text{ for } E \le (\gamma_b - \gamma_a)E_0 \\ &= CE^{-\gamma_b} \left\{ \left[(\gamma_b - \gamma_a)E_0 \right]^{(\gamma_b - \gamma_a)} \exp(\gamma_a - \gamma_b) \right\} \text{ for } E > (\gamma_b - \gamma_a)E_0 \end{aligned} \tag{7}$$

$$dJ / dE = Ck\gamma E^{\gamma - 1} \exp(-kE^{\gamma}), \tag{8}$$

respectively. The spectral (or differential) flux (dJ/dE) is in units of $(cm^2\text{-MeV-s-sr})^{-1}$.

The theoretical interpretations of the analytical spectral forms are the following. The single power-law form in equation (5) represents a diffusive acceleration mechanism for charged

particles in a turbulent magnetic field associated with an interplanetary shock (Tylka & Lee, 2006). The constant C is the abundance of a suprathermal seed population injected upstream of the shock, originating from either the solar wind (corona) or flare or both. The power-law index γ characterizes the acceleration in the turbulent magnetic field and is a function of the shock compression ratio. The Ellison-Ramaty form in equation (6) has a similar interpretation. The e-folding (or turnover) energy E_0 represents a high-energy limit to the acceleration mechanism (e.g., escape of the accelerated charged particles from the shock front through spatial diffusion) (Ellison & Ramaty, 1985). The double power-law form in equation (7) is a combination of the single power-law and the Ellison-Ramaty forms, which represent two independent sources of seed populations (e.g., a prompt high-energy source at a flare location (single power-law) and a coronal or solar wind source accelerated by a coronal mass ejection (CME)-induced interplanetary shock) (Mewaldt et al., 2005; Tylka et al., 2005). The Weibull distribution in equation (8) is generally interpreted in statistical theory as a survival probability. An interpretation in terms of physical processes responsible for SEP origin, acceleration, and transport has not been firmly established. In practice, however, this function quite often fits *in situ* charged particle flux measurements better than the other spectral forms (Townsend et al., 2006, 2003; Xapsos et al., 2000).

The free parameters for each analytical form of the SEP proton spectrum are derived by a nonlinear, least-square fit to the GOES proton flux measurements. The spectral fitting algorithm uses a Marquardt-Levenberg iteration technique (Brandt, 1999). The analytical function that yields the minimum chi-square residual, among the four functional forms, in the fit to the GOES proton flux measurements, is the selected SEP proton spectrum at 1 AU that is used in the subsequent SEP transport and radiation response function calculations (Mertens et al., 2010a, 2012).

A new fitting code was developed in NAIRAS version 3 which has the option to fit a SEP proton spectrum to either the differential GOES proton flux channels or the integral GOES proton flux channels. SEP spectral fitting to the GOES differential proton channels has proven to be problematic in practice. The difficulty is encountered at event onset and for weak-to-moderate events due to a combination of high GCR background levels in the high-energy GOES differential proton channels and the energy-dependent arrival times of the SEP protons. Of course, one can always interpolate and extrapolate the GOES differential proton channels. But this approach necessarily requires introducing artificial and subjective criteria in extrapolating beyond the highest energy GOES differential proton channel (~ 600 MeV), which can account for 50% or more of the effective dose in well shielded environments (e.g., aviation altitudes, ISS, Orion Multipurpose Crew Vehicle (MPCV)) (cf., Mertens & Slaba, 2019).

Despite the theoretical and practical problems described in the previous paragraphs, the spectral fitting option to the GOES differential proton channels was software hardened to provide physically sensible results when inferring the SEP proton spectrum. One of the software hardening measures implemented was a criterion on the maximum allowed chi-square residual. If the selected spectral form using the algorithm described in this section does not meet the absolute goodness criterion of maximum chi-square, then the SEP proton spectrum is determined by log-log interpolation/extrapolation of the GOES differential proton flux measurements, with a hard limit set on the extrapolated flux at high energy. This run option was tested extensively for numerous SEP events, from very weak to extremely large events, and for quiet conditions as well. Inferring a SEP proton spectrum from GOES measurements during quiet time provides a

stringent test on the numerical stability of the code. The primary use of this run option is for sensitivity studies and intercomparisons with models that use the GOES differential proton channels to construct the SEP spectrum at 1 AU.

The most important new feature of the NAIRAS version 3 SEP spectral fitting code, however, is the option to infer the SEP spectrum from the GOES integral proton flux channels. Because the GOES integral proton flux measurements are well ordered with respect to energy throughout the time evolution of a SEP event (i.e., monotonically decreasing flux with increasing energy) the SEP proton spectrum can be fit to the GOES integral proton channels without artificial assumptions in the extrapolation to high energy. Thus, it is only the physics embodied in the spectral forms in equations (5) through (8) that inform the extrapolation to high energy. Extensive testing of the new NAIRAS SEP spectral fitting algorithm, by fitting to the GOES integral proton channels, has proven the algorithm to be robust against numerical instability and free from erroneous, non-physical fits while simultaneously consistent with the GOES differential proton channel measurements. An example of a spectral fit to GOES integral proton flux is shown in Figure 4 for the January 20, 2005, SEP event, which was also associated with a ground-level enhancement (GLE 69).

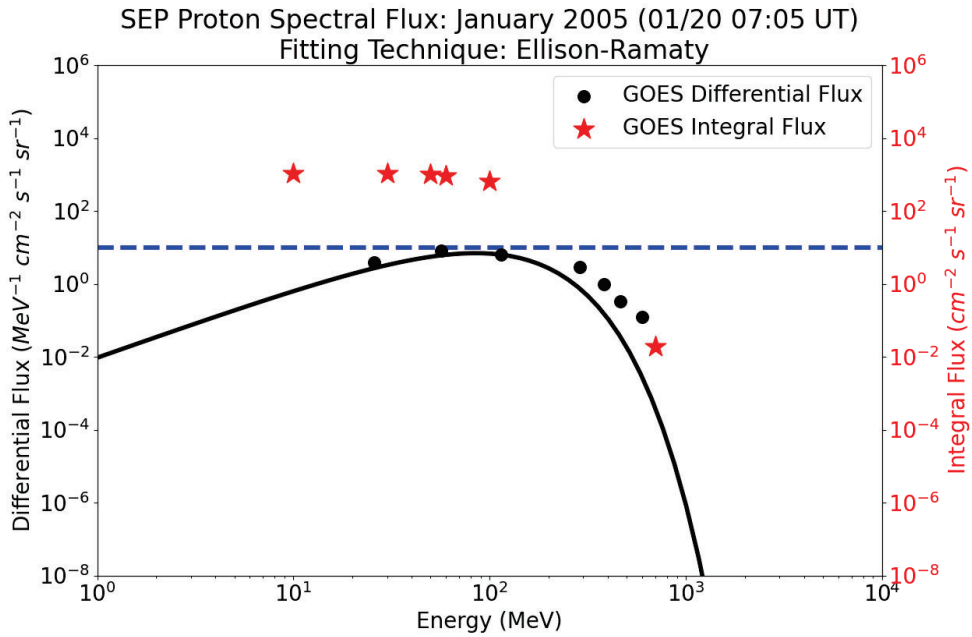

Figure 4. SEP proton spectrum fit (black line) to GOES integral proton flux measurements (red stars). The GOES differential proton flux measurements (black dots) are shown as an independent comparison to the inferred spectrum. The horizonal blue line indicates the NOAA/SWPC SEP event threshold in the >10 MeV proton flux channel.

Despite the several advantages of SEP spectral fitting using GOES integral flux measurements, this approach is more computationally intensive since numerous improper integrals are evaluated for each GOES integral proton channel and at each iteration step in the inversion algorithm. The temporal fidelity of the NAIRAS RoR flight trajectory predictions needed for government and commercial spaceflight missions and the NOAA Space Weather Prediction Center (SWPC) and the International Civil Aviation Organization goals for aviation radiation nowcasts and forecasts are driving the requirement to predict SEP radiation quantities at 5-minute time intervals. This requirement is difficult to meet using the GOES integral flux measurements to infer the SEP

proton spectrum. To circumvent this computational burden, analytical expressions were derived for the Jacobian matrix and vector components of the forward model which are called at each iteration step in the inversion algorithm, based on the set of four analytical SEP spectral forms in equations (5) through (8) used in the SEP spectral fitting algorithm. This update was successful and enabled the option to fit the SEP proton spectrum to GOES integral flux measurements to be used operationally at 5-minute time intervals. The details of the numerical implementation of the SEP proton spectral fitting algorithm are given in Appendix B.

The SEP proton spectral fitting procedure is repeated at each time step throughout the evolution of a SEP event, which is nominally a 5-minute time interval (Mertens et al., 2024). In principle, the selected analytical function can change at each time step. In practice, however, one of the analytical functions tends to dominate the rise, another the peak, and another the later decay phase of the event. Statistics on the fitted analytical SEP proton spectrum over the entire duration of an event are shown in Figure 5 for three SEP events. The Ellison-Ramaty (ER) double power-law (DP) spectrum dominates the time evolution of the Halloween 2003 and January 2005 SEP events, although the Weibull (WB) function is a closer second place in the Halloween 2003 event. For the September 2017 event, the fitted analytical SEP proton spectra are evenly distributed among the ER, DP, and WB functions. Albeit a limited sample size, there is an ordering of the fitted analytical SEP proton spectra with respect to GLE strength. For the January 2005 event (GLE 69), which had the largest GLE of the three SEP events, the fitted SEP proton spectrum is dominated overwhelmingly by the DP spectrum. For the weakest GLE, which was the September 2017 SEP event (GLE 72), the fitted analytical SEP proton spectrum is evenly distributed among the analytical functions which have some form of high-energy cutoff. At intermediate GLE strengths, for which the Halloween 2003 SEP events are representative (GLE 65 to 67), the DP form dominates the fitted SEP proton spectrum but with other analytical spectral representations contributing substantially to the evolution of the event as well. Extending this analysis to a larger sample size may provide fruitful insight to empirically infer characteristics of the origin, acceleration, and transport of SEP events.

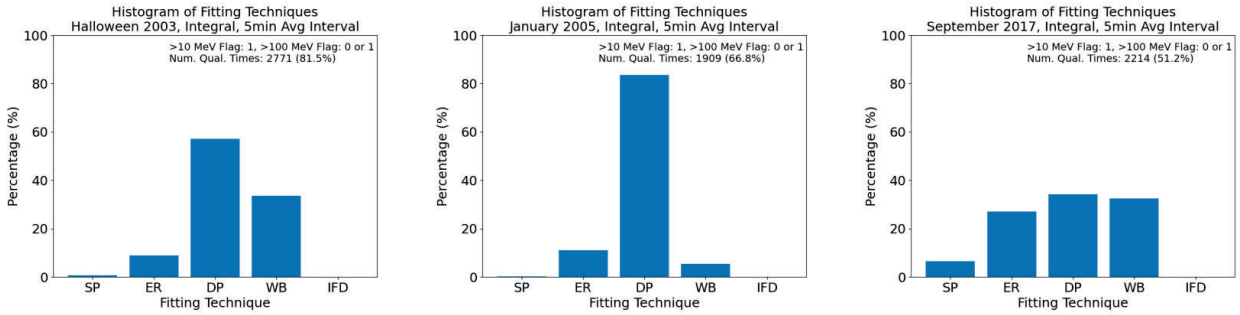

Figure 5. Statistical distribution of fitted analytical SEP proton spectra for the Halloween 2003 (left), January 2005 (center), and September 2017 (right) SEP events. The analytical functions denoted in the panels are single-power law (SP), Ellison-Ramaty (ER), Ellison-Ramaty double power-law (DP), and Weibull (WB). The analytical SEP proton spectra were fitted to GOES integral proton flux measurements using the techniques described in Section 8.1.2.1. The fitting technique denoted IFD refers to integral flux derivative method. The IFD is a numerical technique developed in case the four analytical functions fail to meet the convergence and goodness criteria of the fitting algorithm. However, to date, the analytical SEP proton spectral forms have never failed to meet the stringent fitting criteria (see Appendix B).

8.1.2.2 Heavy Ions

The SEP heavy-ion model is a new component of NAIRAS version 3. The heavy-ion model includes fully ionized nuclear isotopes from alpha particles (Z = 2, A = 4) through uranium (Z = 92, A = 238). The SEP element abundances of the model are compared to the H-BON10 GCR element abundances in Figure 6. SEP heavy-ion spectra are obtained using fixed solar element abundance ratios relative to solar alpha abundance, combined with GOES differential alpha flux measurements to scale the relative abundance ratios to absolute elemental heavy-ion spectra (Mertens et al. 2024). The approach of deriving the SEP heavy-ion abundance ratios is based on similar datasets described by Xapsos et al. (2007).

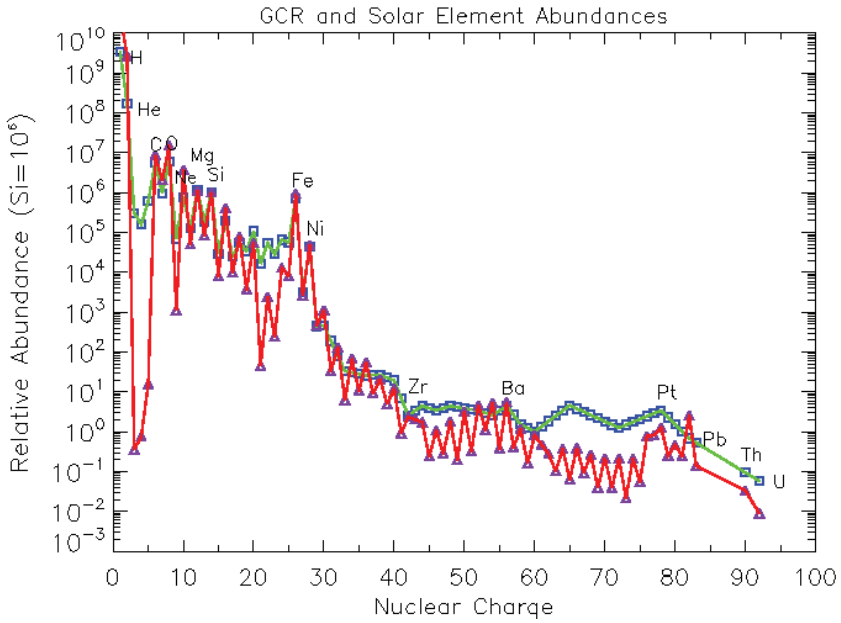

Figure 6. GCR and SEP element abundance ratios from NAIRAS version 3. The GCR element abundances (blue line) are obtained from the H-BON10 model component (Section 8.1.1). The SEP element abundances (red line) are obtained from the SEP heavy-ion model (Section 8.1.2.2). The relative abundances are normalized to (silicon) Si = 10^6.

The SEP heavy-ion abundance ratios are derived from three data sources. The first data source is the Solar Isotope Spectrometer (SIS) instrument onboard the NASA Advanced Composition Explorer (ACE) satellite, which measures differential flux from 13 major heavy-ion elements with Z > 2 from carbon (Z = 6) to nickel (Z = 28) over an energy range from ~ 10 MeV/n to 100 MeV/n (Stone et al., 1998). The abundance ratios of the major heavy-ion elements were derived by dividing the ACE/SIS event-fluence (fitted) spectra by the GOES alpha event-fluence (fitted) spectra over all SEP events from 1997 to 2017 for each of the 13 major heavy-ion elements. The abundance ratio is taken as the average of the spectral fluence ratios over an energy range common to both the ACE/SIS element differential flux measurements and the GOES differential alpha flux measurements.

The second data source is measurements from the International Sun-Earth Explorer-3 (ISEE-3) satellite, which was used to derive solar abundance ratios for seven minor heavy-ion elements. The ISEE-3 satellite observed 49 SEP events over a period of 14 years (Reames, 1998). The ISEE-3 measurements also included the same major heavy-ion elements measured by ACE/SIS. Thus, ISEE-3 abundance ratios were computed between the seven minor heavy-ion elements and

the nearest major heavy-ion element measured by ACE/SIS, and then this ratio was scaled by the corresponding major heavy-ion ACE/SIS to GOES/alpha abundance ratio.

The third data source is photospheric emission measurements, which utilized three-dimentional (3D) time-dependent hydrodynamic models of the solar atmosphere combined with non-local thermodynamic equilibrium radiation transfer models in the remote sensing inverse model (Grevesse, 2019). The photospheric emissions were used to derive the remaining solar heavy-ion element abundance ratios relative to alpha abundance. An additional scale factor of four was applied to the abundance ratio if the first ionizing potential (FIP) of the solar photospheric element is less than 10 eV, which better approximates the solar heavy-ion element abundance in the solar wind and SEP events (Reames, 1998).

The SEP heavy-ion spectra are subsequently computed by multiplying the SEP alpha spectrum by the heavy-ion element abundance ratios described in the previous paragraph. The SEP alpha spectrum, on the other hand, is obtained from the SEP proton spectrum inferred from the GOES proton flux measurements, as described in Section 8.1.2.1, by deriving a normalization factor such that the normalized alpha spectrum agrees with the GOES differential alpha flux measurements in the least-square sense. In this approach, the spectral shape of the SEP heavy-ion spectra is determined by the inferred SEP proton spectrum, while the magnitude of the heavy-ion spectra is determined by the method that combines the GOES differential alpha flux measurements with the pre-computed heavy-ion element abundance ratios.

Results from the SEP heavy-ion model are shown in Figure 7 for the 2000 Bastille Day SEP event. The SEP proton and heavy-ion spectra were inferred at 5-minute intervals over the event duration from July 14, 2000, 03:00 UT (universal time) to July 15, 2000, 14:00 UT using the models and techniques described in Sections 8.1.2.1 and 8.1.2.2. Event fluences are shown in Figure 7. The line denoted heavy-ion spectrum is the sum of the individual fluence spectra of all solar elements with charge and mass greater than alpha particles (Z > 2, A > 4).

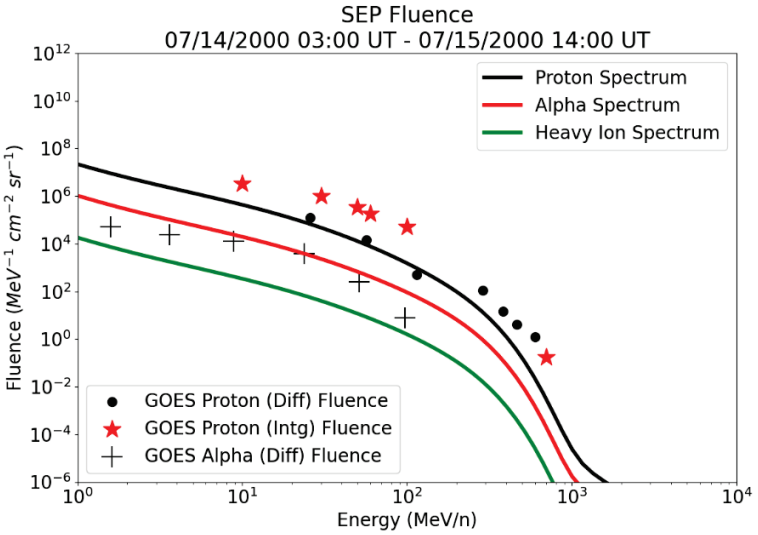

Figure 7. SEP proton spectrum fit (black line) to GOES integral proton flux measurements (red stars). The GOES differential proton flux measurements (black dots) are shown as an independent comparison. The SEP alpha spectrum fit (red line) to GOES differential alpha flux measurements (plus symbol) are also shown. SEP heavy-ion spectrum (green line) is summed over all individual solar heavy-ion element spectra with charge/mass greater than alpha.

The primary motivation for developing the SEP heavy-ion model is to provide LET spectra for characterizing SEE during SEP events. The impact of SEP heavy-ions on the differential and integral flux and fluence quantities are discussed in more detail in Section 9.1. However, analysis has also shown that SEP heavy-ions contribute significantly to SEP effective dose at LEO. Event-total effective dose was computed for 10 large historical SEP events with two different SEP spectral flux boundary conditions: 1) assuming SEP protons only and 2) by including both SEP protons and SEP heavy-ions. The historical SEP events are the top 10 largest SEP events with respect to free-space radiation for a 10 g/cm^2 aluminum sphere (Minow et al., 2020). The SEP effective dose was computed along a LEO flight trajectory similar to the ISS orbit (i.e., 51.6 degree inclination at 400 km). The results of the analysis are summarized in Table 2.

Table 2. Impacts of SEP Heavy-Ions on SEP Effective Dose for LEO Trajectory With 51.6 Degree Inclination at 400 km for the Top 10 Historical SEP Free-Space Radiation Storms

SEP Event Date	Start Time (UT)	Duration (Hours)	Shielding Depth: 2 g/cm^2		Shielding Depth: 50 g/cm^2	
			Total Effective Dose (mSv)	Total Effective Dose Ratio (total/proton)	Total Effective Dose (mSv)	Total Effective Dose Ratio (total/proton)
10/19/1989	12:00	48	40.2	2.24	0.35	1.15
07/14/2000	09:00	48	163.4	2.37	1.81	1.42
11/08/2000	22:00	24	152.8	2.13	1.33	1.28
09/29/1989	09:00	48	23.6	2.73	0.13	1.24
10/28/2003	10:00	48	137.0	2.78	1.15	1.43
11/04/2001	16:00	48	177.5	1.75	1.84	1.16
01/20/2005	06:00	24	16.8	1.88	0.41	1.39
03/07/2012	01:00	48	51.8	2.08	0.69	1.29
04/15/2001	13:00	48	4.6	1.87	0.15	1.52
08/12/1989	14:00	48	17.6	1.68	0.16	1.13

The total-event effective dose for each SEP event presented in Table 2 was computed at shielding depths of 2 g/cm^2 and 50 g/cm^2 of aluminum. Astronaut spacesuit shielding during an EVA is represented by a depth of 2 g/cm^2 of aluminum-equivalent material. A spacecraft shielding of 50 g/cm^2 is representative of the median aluminum-equivalent shielding distribution surrounding the ISS detectors (Badavi et al., 2011; Slaba et al., 2020b). For each shielding depth, the total effective dose from the contributions of including both SEP protons and SEP heavy-ions is shown in one column, and the ratio of this dose to the total effective dose from SEP protons only is shown in the adjacent column. For nearly half of the top 10 largest SEP events (4 out of 10 events), the SEP heavy-ions contribute roughly 40% or more to the event-total SEP effective dose in the typical ISS interior shielding environment. The SEP heavy-ions increase the effective dose for typical astronaut EVA shielding by a factor of 2 to 3 for nearly all of the historical SEP events.

The SEP heavy-ion spectra uncertainty was assessed by comparing event fluences to ACE/SIS data for the SEP events listed in Table 2, which also overlapped SIS operations beginning in 1997. The uncertainty in total heavy-ion fluence averaged over the seven overlapping SEP events is 71%, where total in this sense is defined by the sum of the fluences of the 13 major heavy-ion elements measured by SIS. The total heavy-ion uncertainty is dominated by the alpha fluence as GOES differential alpha flux measurements are larger than the SIS differential alpha flux measurements by 70% on average. The minimum and maximum average model uncertainty of

the remaining 12 heavy-ion elements measured by SIS is 14% for sulfur and 62% for carbon, respectively. The heavy-ion sensor on the GOES-R Series Space Environment In-Situ Suite (SEISS) is an important new measurement asset for refining the assessment of the uncertainty in the NAIRAS SEP heavy-ion model for future SEP events (Kress et al., 2019), with the goal of subsequently improving the model.

8.1.3 Radiation Belt Trapped Protons

The GEOFFB TRP-p belt model was integrated into NAIRAS version 3 to extend the model domain from the atmospheric ionizing radiation environment to the geospace radiation environment (Badavi et al., 2011). GEOFFB is based on the AP8MIN and AP8MAX maps of measured TRP-p fluxes at solar minimum (1965) and solar maximum (1970) for solar cycle 20 (Vette, 1991). GEOFFB interpolates and extrapolates beyond the time periods of the AP8MIN/AP8MAX proton flux databases using parametric fits derived to account for the long-term drift of the South Atlantic Anomaly (SAA) and the effects of solar cycle modulation on the population of TRP-p in the inner radiation belt.

The solar modulation of the inner belt protons is governed mainly by the cosmic ray albedo neutron decay (CRAND) production mechanism and loss by interactions with the neutral atmosphere (Wilson et al., 2002). Thus, the kinetic rate equation for the TRP-p distribution function (f_p) is approximated by:

$$\frac{\partial f_p}{\partial t} \approx P_{\text{CRAND}} - \frac{f_p}{\tau_{\text{atm}}} \ , \tag{9}$$

where P_{CRAND} is the CRAND production rate and τ_{atm} is the atmospheric loss time constant. Under steady-state conditions, the TRP-p distribution function is proportional to the product of the CRAND production rate and atmospheric loss time constant, such that:

$$f_p \approx P_{\text{CRAND}} \bullet \tau_{\text{atm}} \, . \tag{10}$$

Therefore, the strength and temporal variation of the solar cycle modulation of the TRP-p is parameterized in GEOFFB by a variable that is the product of neutron monitor count rate and the 10.7-cm solar radio emission (F10.7) index (Badavi et al., 2011). The rate of secondary atmospheric neutrons detected by ground-based neutron monitors is a proxy for the CRAND production mechanism and its variation with solar cycle. The solar radio emission F10.7 index and its solar cycle variation is a proxy for atmospheric loss of TRP-p and the solar cycle modulation of this loss mechanism due to the upper atmospheric neutral density.

The parameterization of the solar cycle modulation function, and the parameterization of the long-term SAA drift, were calibrated against extensive onboard measurements from the ISS and the Space Transportation System (STS) Space Shuttle Program (Badavi et al., 2011). This approach successfully accounts for solar cycle modulation of the inner belt TRP-p while eliminating unrealistic extrapolations produced by simply incorporating the secular changes in the internal geomagnetic field model (Heynderickx, et al., 1996). Nevertheless, the NAIRAS comparisons with dosimetric measurements at LEO and MEO presented in Sections 9.1 and 9.2 show that the Daly and Evans (1996) altitude interpolation technique adopted by GEOFFB renders the 0.5 attenuation factor introduced by Badavi et al. (2011) unnecessary (Mertens et al., 2024).

The key data inputs that parameterize the solar cycle modulation in the GEOFFB TRP-p model are shown in Figures 8 and 9. Deep-River neutron monitor data (DRNM) were used initially in the development of the solar cycle modulation. DRNM was discontinued in 1995. A normalization factor was determined between DRNM and Oulu neutron monitor data over the period of data overlap (1965 to 1995), and normalized Oulu data have been used as a DRNM proxy to continue the DRNM count rates in the GEOFFB model from 1995 to the present (Wilson et al., 2002). DRNM monthly data from 1960 to 2025 are shown in Figure 8. The data in Figure 8 were extrapolated from years 2020 to 2025 by correlating DRNM to sunspot number (SSN) and using the SSN forecasts provided by NASA Marshall Space Flight Center (MSFC) (https://www.nasa.gov/solar-cycle-progression-and-forecast/#archive). The SSN data were version 2.0, 13-month smoothed data from the Royal Observatory in Belgium (https://www.sidc.be/SILSO/datafiles). The SSN forecasts were 50% percentile projections which were also based on SSN version 2.0. The F10.7 index data are shown in Figure 9, which were obtained from NASA GSFC OMNIWeb (https://omniweb.gsfc.nasa.gov/form/dx1.html). The F10.7 data were also extrapolated from 2020 to 2025 using 50% percentile projection forecasts from NASA MSFC.

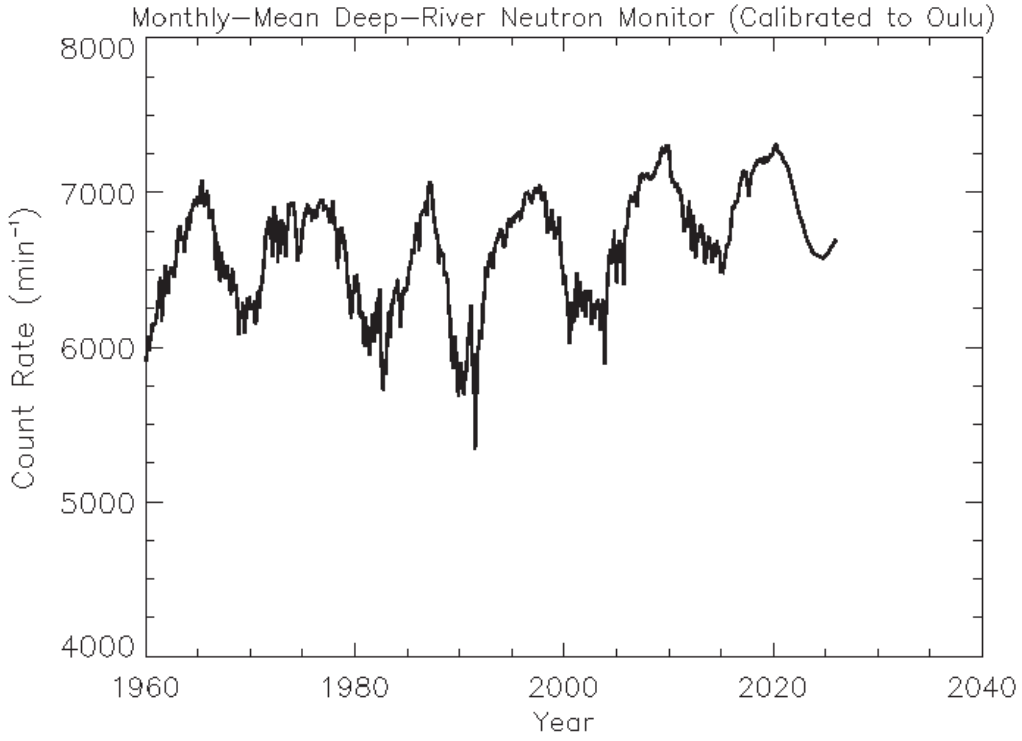

Figure 8. DRNM monthly averaged count rates. After 1995 Oulu neutron monitor data, normalized to DRNM over the period of data overlap (1965-1995), are used to continue DRNM data.

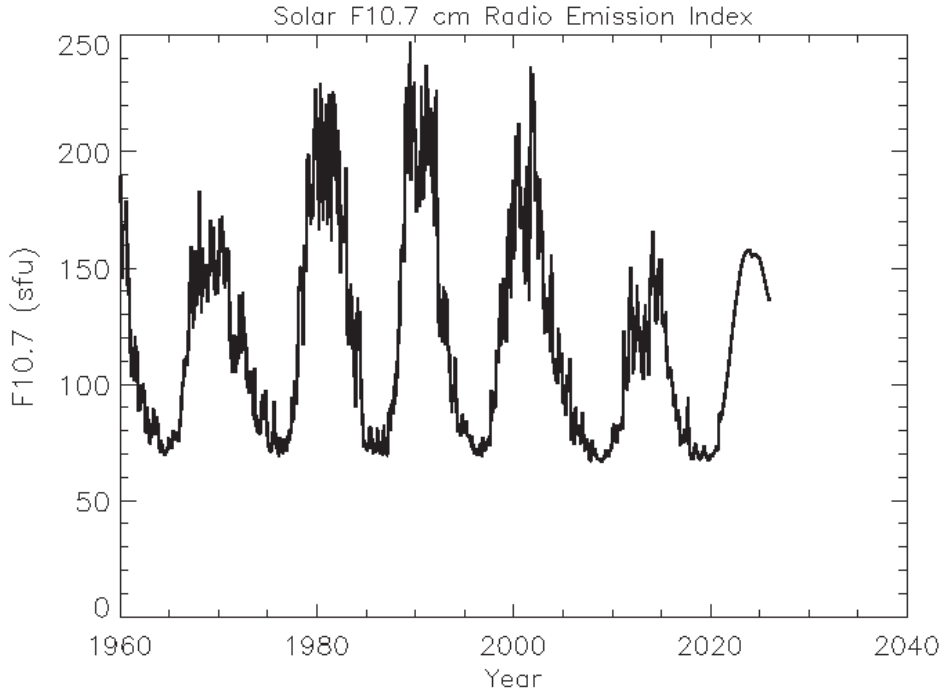

Figure 9. Monthly averaged solar radio emission 10.7 cm (F10.7) index. The F10.7 data are reported in solar flux units (sfu: 10^{-22} m^{-2} Hz^{-1}).

To provide rapid post-flight analysis, the NAIRAS RoR run option was developed so that this service can be utilized within hours after the launch of a spacecraft. The GEOFFB solar cycle modulation parameterization, however, is based on the prior 15-month average (current month inclusive) of the DRNM and F10.7 data. This fact is the reason these two parameters are extrapolated using the solar cycle forecasts of these quantities, as described in the previous paragraph. The maximum monthly error in the solar cycle modulation correction over the period 2021 to 2022 is around 20%. To ensure the extrapolation error does not become too large, a future improvement to the implementation of GEOFFB in NAIRAS version 3 will be to update the DRNM and F10.7 data monthly and rescale the remaining forecast period. The result of this step will be that the current DRNM count rate and F10.7 index are based on a 1-month extrapolation at most.

Based on the previous discussion, the time-dependence of TRP-p spectral flux is formulated as (Wilson et al., 2002):

$$\phi_p(\mathbf{r},E,t) = \phi_{p,\min}(\mathbf{r},E)\exp\left\{-\alpha_p\left[DRNM(t)\bullet F10.7(t)\right]\right\}, \tag{11}$$

where $\phi_{p,\min}(\mathbf{r},E) = \phi_{AP8MIN}(\mathbf{r},E)$. The solar cycle modulation parameter α_p is a function of the product of the DRNM count rate and the F10.7 index, and depends also on the AP8MIN and AP8MAX TRP-p flux databases (i.e., $\phi_{AP8MIN}(\mathbf{r},E)$ and $\phi_{AP8MAX}(\mathbf{r},E)$).

An example TRP-p spectrum from GEOFFB is presented in Figure 10 for November 2, 2003. The spectrum is shown for a geographic location near the central region of the SAA. The altitude of the spectrum is in the lower LEO range close to typical ISS altitudes. The TRP-p flux at this geographic coordinate remains high from low energies to 100 MeV, and diminishes rapidly by 500 MeV and greater.

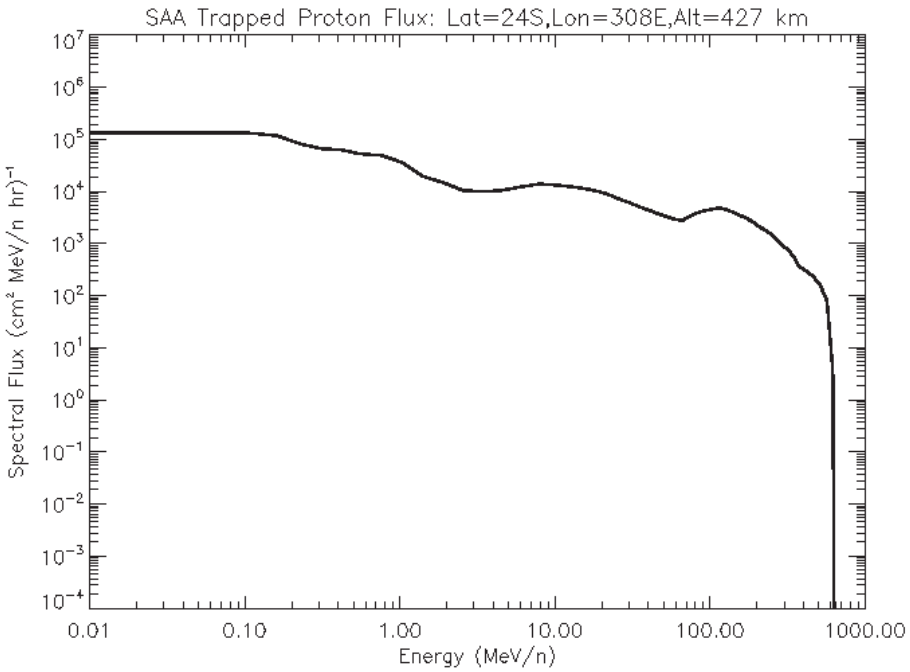

Figure 10. TRP-p spectral flux from the GEOFFB model at a geographic location near the central region of the SAA and at an altitude in the range of ISS altitudes.

8.1.4 Radiation Belt Trapped Electrons

The GEOFFB TRP-e belt model was integrated into NAIRAS version 3 to achieve improved agreement between the model predictions and measurements from a lightly shielded dosimeter outside the ISS. The outer belt electrons map to low altitudes for certain high-latitude regions (https://www.spenvis.oma.be/help/background/traprad/traprad.html), due to the offset and tilt of the internal magnetic dipole moment with respect to Earth's rotational axis. Furthermore, the TRP-e contribute to astronaut radiation exposure at high latitudes during EVA. These points are discussed in more detail in Section 9.1.

Analogous to the TRP-p model, the GEOFFB TRP-e model is based on AE8MIN and AE8MAX maps of measured TRP-e fluxes at solar minimum (1965) and solar maximum (1970) for solar cycle 20 (Vette, 1991). The AE8MIN/AE8MAX flux databases include the inner and outer radiation belt electron distributions. GEOFFB interpolates within and extrapolates beyond the time periods of the AE8MIN/AE8MAX electron flux databases using parametric fits to account for the long-term SAA drift and the effects of solar cycle modulation on the radiation belt TRP-e population. The TRP-e long-term SAA drift parameterization is identical to the parameterization for the trapped protons (Badavi et al., 2011).

The long-term, solar cycle modulation of the TRP-e arises from a dynamical balance between electron injection and trapping in the outer belt zone through the magnetotail and loss by radial diffusion into the atmosphere near the polar regions (Wilson et al., 2002). Thus, the steady-state, kinetic rate equation for the TRP-e distribution function (f_e) has a similar form to equation (9) for the trapped proton distribution function:

$$f_e \approx P_{\mathrm{INJ}} \bullet \tau_{\mathrm{atm}}, \tag{12}$$

where P_{INJ} is the outer belt electron injection rate and τ_{atm} is the time constant for inward radial diffusion followed by loss due to the neutral atmosphere. Contrary to the trapped protons, however, it is assumed in GEOFFB that electron injection and atmospheric loss are both correlated with the F10.7 index. Consequently, the strength and temporal variation of the solar cycle modulation of the TRP-e is parameterized by the F10.7 index only. The input F10.7 index data to the GEOFFB TRP-e model is the same as for the TRP-p model, which is shown in Figure 9.

The time-dependence of the TRP-e spectral flux is given by the following expression (Wilson et al., 2002):

$$\phi_e(\mathbf{r}, E, t) = \phi_{e,\min}(\mathbf{r}, E) \exp\left\{-\alpha_e \left[F10.7(t)\right]\right\}. \tag{13}$$

The solar cycle modulation parameter α_e is a function of the F10.7 index, and depends on the AE8MIN and AE8MAX TRP-e flux databases as well (i.e., $\phi_{AE8MIN}(\mathbf{r}, E)$ and $\phi_{AE8MAX}(\mathbf{r}, E)$). The quantity $\phi_{e,\min}$ is given by $\phi_{e,\min}(\mathbf{r}, E) = 0.1 \bullet \phi_{AE8MIN}(\mathbf{r}, E)$, where the scale factor (0.1) was inferred from comparisons of the NAIRAS model with lightly shielded dosimeter measurements at LEO, the results of which are shown in Section 9.1. Such a large scale factor may indicate that the GEOFFB solar modulation correction approach does not work as well for TRP-e as it does for trapped protons, at least at LEO altitudes. Future validation studies will refine the scale factor by comparing NAIRAS to additional LEO measurements and observations at altitudes above LEO. Furthermore, range straggling is an important process in electron transport (Wilson et al., 1991). An underestimation of electron straggling in the transport code will overestimate the electron flux at a given depth within a material. Future studies will investigate the accuracy of accounting for eletron straggling processes in the NAIRAS radiation transport code using techniques developed by Mertens et al. (2007, 2010b).

GEOFFB TRP-e spectra are shown in Figure 11 for November 2, 2003. The inner belt TRP-e spectrum is shown in the top panel at a geographic location close to the center of the SAA for an altitude near typical ISS altitudes. For comparison, the corresponding inner belt TRP-p spectrum for the same geolocation is also shown. The TRP-e flux is orders of magnitude greater than the TRP-p flux for energies less than about 1 MeV. However, the TRP-e flux decreases drastically for energies greater than about 3 MeV. A TRP-e spectrum is shown in the bottom panel for a high-latitude location where the outer belt electrons map to low altitudes. In the case of the outer belt electrons, the steep decrease in flux occurs at energies greater than about 5 to 6 MeV.

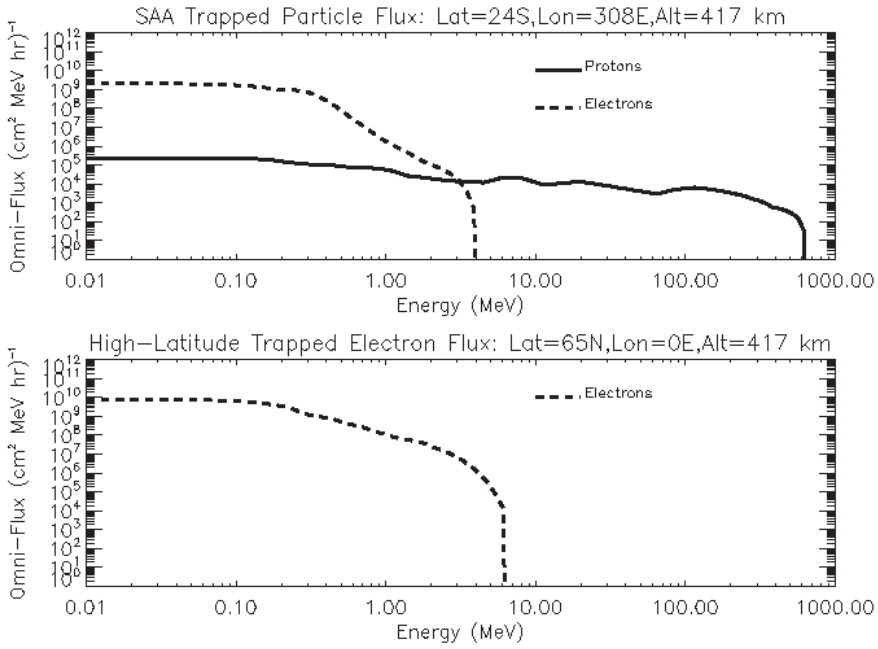

Figure 11. (top) TRP-e and proton spectral flux from the GEOFFB model at a geographic location near the central region of the SAA and at an altitude in the range of ISS altitudes; (bottom) TRP-e spectral flux at a high-latitude location where the outer belt electrons map to low altitudes.

8.2 Geomagnetic Transmission

The geomagnetic field (i.e., internal field plus magnetospheric contributions) provides a form of momentum shielding, or attenuation, with respect to charged particles incident on the geospace environment (e.g., GCR and SEP ions) (Mertens et al., 2012). The incoming charged particles are deflected by the geomagnetic field via the Lorentz force and lower momentum particles can be deflected out to space or towards the Earth's surface, or confined to quasi-trapped orbits. This spectral filtering is quantified by the cutoff rigidity. Rigidity is defined as the particle's momentum per charge. At each geographic location (latitude, longitude, altitude), there is a cutoff rigidity for each arrival direction (zenith and azimuth angles) of incoming charged particle such that the charged particle must have a rigidity greater than or equal to the cutoff rigidity to reach that location. Once the cutoff rigidity is known, the minimum access energy of any particle of charge number Z and mass number A can be determined from the relativistic energy equation (Mertens et al., 2010a, 2012).

The solution of charged particle motion in a pure dipole magnetic field was examined by Stormer (1965). The azimuthal angular momentum is conserved because of the symmetry of the dipole field (Stormer, 1965; Van Allen, 1968). This allows the directional cutoff rigidity to be derived analytically, which can be expressed in the following form:

$$R_{dc}(r,\psi,\varphi;\varepsilon,\beta)=\left(\frac{r_{ref}}{r}\right)^2\frac{4R_{vc}(r_{ref},\psi,\varphi)}{\left[1+\sqrt{1-\sin\varepsilon\sin\beta\cos^3\psi}\right]^2}\ . \tag{14}$$

In equation (14), the radial distance, magnetic latitude, and magnetic longitude are denoted r, ψ, and ϕ, respectively. The zenith direction of the arriving charged particle with respect to the local vertical direction is denoted ε, while β corresponds to the azimuthal direction of the arriving

charged particle with respect to the local north direction, and clockwise rotation from local north denotes a positive azimuth angle (Smart & Shea, 2005). The cutoff rigidity for vertically arriving particles, or vertical cutoff rigidity, is denoted R_{vc}, which is calculated at a reference altitude r_{ref}.

The Earth's magnetic field, however, is not a pure dipole. The internal magnetic field consists of dipolar and non-dipolar contributions. Furthermore, the dipole moment is off-center and tilted with respect to the Earth's rotational axis. The magnetospheric current systems generate their own magnetic fields which combine vectorially with the internal magnetic field. Thus, the complexities of the actual geomagnetic field require numerical methods to determine the cutoff rigidity (Mertens et al., 2012). The numerical solution, however, is computationally time-consuming. The approach in NAIRAS version 3 is to employ a numerical model to calculate the vertical cutoff rigidity and use the analytical Stormer equation in equation (14) to scale the numerically determined vertical cutoff rigidity to other arrival directions.

The NAIRAS geomagnetic vertical cutoff rigidity model is based on the CISM-Dartmouth model developed by Kress et al. (2004, 2010). The CISM-Dartmouth model calculates the vertical cutoff rigidity from numerical solutions of charged particle trajectories in a dynamically varying geomagnetic field that includes both the internal magnetic field and the magnetospheric magnetic field contributions (Mertens et al., 2012). The internal magnetic field model is the International Geomagnetic Reference Field (IGRF) model (Mertens et al., 2012). The magnetospheric magnetic field model is the semi-physics-based TS05 model (Tsyganenko & Sitnov, 2005). The main input data to the TS05 model are the solar wind plasma parameters and interplanetary magnetic field (IMF) components, which are obtained from the NASA ACE satellite, or the NOAA Deep Space Climate Observatory (DSCOVR) satellite, and the SYM-H or Kyoto Dst index. The CISM-Dartmouth model employs numerical procedures that provide reasonably accurate vertical cutoff calculations while also enabling the cutoffs to be calculated globally in real-time (Kress et al., 2010; Mertens et al., 2010a). The CISM-Dartmouth vertical cutoff model has been a component of the NAIRAS model from its inception.

Several extensions and updates to the CISM-Dartmouth cutoff model have been made in the development of NAIRAS version 3, which were motivated mostly by the development of the RoR capability. The cutoff model now includes an option to use the T89 magnetospheric magnetic field model (Tsyganenko, 1989), which uses only the Kp-index as the input quantity to capture the dynamical response to solar-geomagnetic variability. The T89 model does not represent the response of the magnetosphere to geomagnetic variably nearly as well as the TS05 model (see Figure 12), but prior to the real-time operation of the ACE satellite in 1995, there was arguably no better representation of the magnetospheric magnetic field. The T89 option allows historical solar-geomagnetic storm events to be analyzed prior to 1995.

Supporting software was developed to maintain the databases of the input solar-geomagnetic parameters required by the TS05 and T89 models. The archived ACE real-time 5-minute solar wind data products have large data gaps during SEP events. A data gap filling algorithm was developed and automated to pull from other sources to fill in the missing ACE solar wind data during SEP events. In addition, the input interface of the CISM-Dartmouth cutoff model was modified to allow the selection of global cutoff calculations or cutoff calculations at discrete geographic locations, significantly reducing the computational time for the RoR flight trajectory run option. The cutoff code was also modified to provide greater flexibility and efficiency in

parallelizing the vertical cutoff calculations for both the NAIRAS version 3 global and flight trajectory run options (see Table 1).

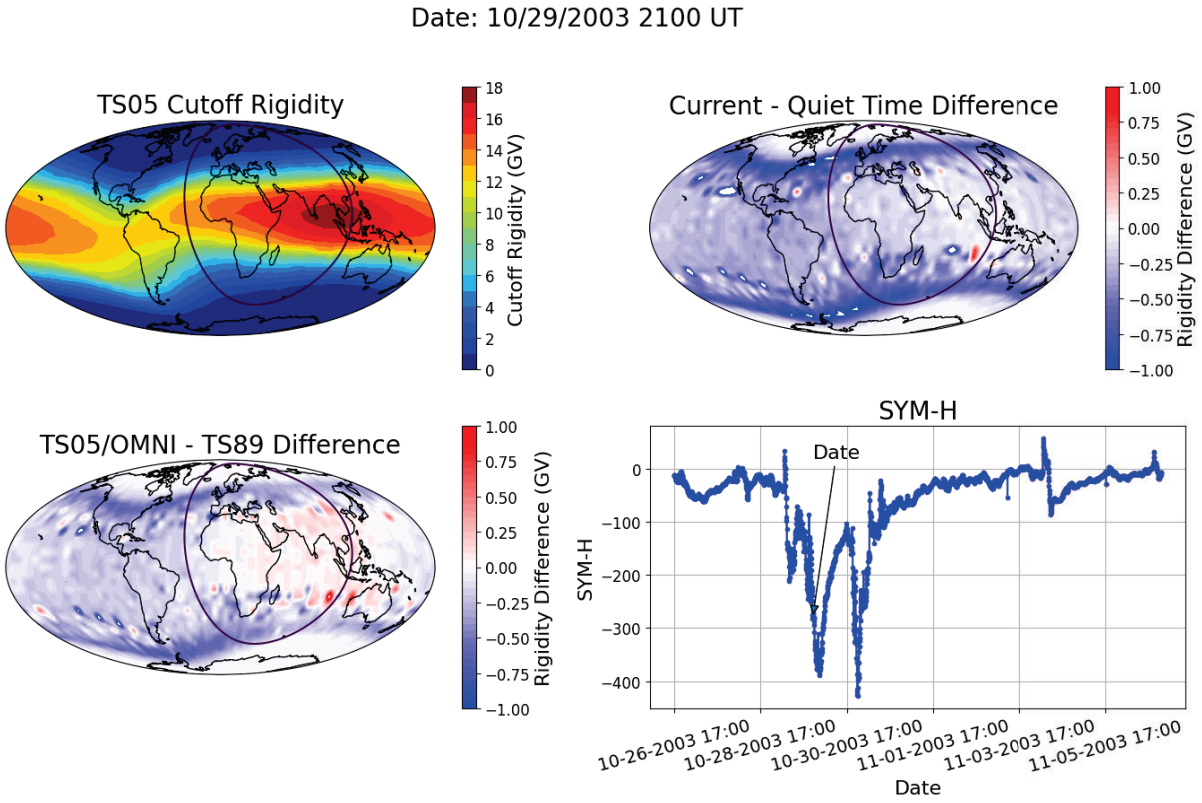

Figure 12. Vertical geomagnetic cutoff rigidity model calculations at 20 km for aviation radiation applications. The time period shown is during the maximum suppression of the cutoff for the Halloween 2003 solar-geomagnetic storm events. Top left: vertical cutoff using TS05 magnetospheric magnetic field model. Top right: cutoff differences between the geomagnetic storm and quiet-time period before the geomagnetic activity. Bottom left: cutoff differences between TS05 and T89 field models. Bottom right: SYM-H index. The arrow points to the time of maximum cutoff rigidity suppression. The circle in the cutoff panels encompasses the daytime region for 21:00 UT on October 29, 2003.

Moreover, in the geospace environment the vertical cutoff rigidity alone is not adequate to parameterize the geomagnetic transmission of GCR and SEP primary particle spectra through the magnetosphere, which is a customary approximation for the atmospheric ionizing radiation environment. Thus, the version 3 NAIRAS model was updated to include altitude-dependent and rigidity-dependent geomagnetic transmission function calculations.

The transport of free-space GCR and SEP ions through the magnetosphere can be described in terms of the geomagnetic transmission function such that:

$$\Phi_i(\mathbf{r},\mathbf{\Omega},R) = \int_{\Omega'}\int_{0}^{\infty} T(\mathbf{r};\mathbf{\Omega},R;\mathbf{\Omega}',R')J_i(\mathbf{\Omega}',R')d\mathbf{\Omega}'dR' \quad . \tag{15}$$

In equation (15), $\Phi_i(\mathbf{r},\boldsymbol{\Omega},R)$ is the directional-differential flux of GCR or SEP particle type i at location $\mathbf{r}$ moving in direction $\boldsymbol{\Omega}$ with rigidity R; $J_i(\boldsymbol{\Omega},R)$ is the free-space, directional-differential flux of GCR or SEP particle type i outside the magnetosphere at 1 AU.

The geomagnetic transmission function is independent of particle type in rigidity space and is approximated by the functional form:

$$T(\mathbf{r};\boldsymbol{\Omega},R;\boldsymbol{\Omega}',R') = H[R' - R_{dc}(\mathbf{r},\boldsymbol{\Omega}')]\delta(R - R') \tag{16}$$

where $H(x)$ is the Heavyside step function defined by $H(x) = 1$ if $x > 1$. Otherwise, $H(x) = 0$. The Dirac delta function in rigidity employs the assumption that there are no energy changing processes in the transport through the magnetosphere. The directional cutoff rigidity $R_{dc}(\mathbf{r},\boldsymbol{\Omega})$ is given by equation (14). The free-space GCR or SEP directional-differential flux is assumed to be directionally isotropic. Given these assumptions and by substituting equation (16) into equation (15), the magnetospheric transport equation in equation (15) is then approximated by:

$$\Phi_i(\mathbf{r},\boldsymbol{\Omega},R) \approx \overline{T}(\mathbf{r},R)J_i(R) \tag{17}$$

where $J_i(R)$ is the free-space, omni-directional GCR or SEP differential flux of particle type i. The directional-integrated geomagnetic transmission function in equation (17) is given by:

$$\overline{T}(\mathbf{r},R) = \int_{\boldsymbol{\Omega}'} H[R - R_{dc}(R,\boldsymbol{\Omega}')]d\boldsymbol{\Omega}' \tag{18}$$

where the integration over solid angle in equation (18) includes the Earth's shadow.

An example of NAIRAS version 3 magnetospheric transport is shown in Figures 13 and 14. The geomagnetic transmission function at an altitude in the LEO radiation environment is shown in Figure 13. The vertical dashed line denotes the vertical geomagnetic cutoff rigidity for this location. The effect of the altitude and rigidity dependences of the geomagnetic transmission function is that a unique, single value of the cutoff rigidity cannot be defined. The upper bound of the geomagnetic transmission function at high rigidity is not unity due to the Earth's shadow effect. The GCR differential flux at a location in the LEO radiation environment, after magnetospheric transport of the free-space GCR, is shown in Figure 14.

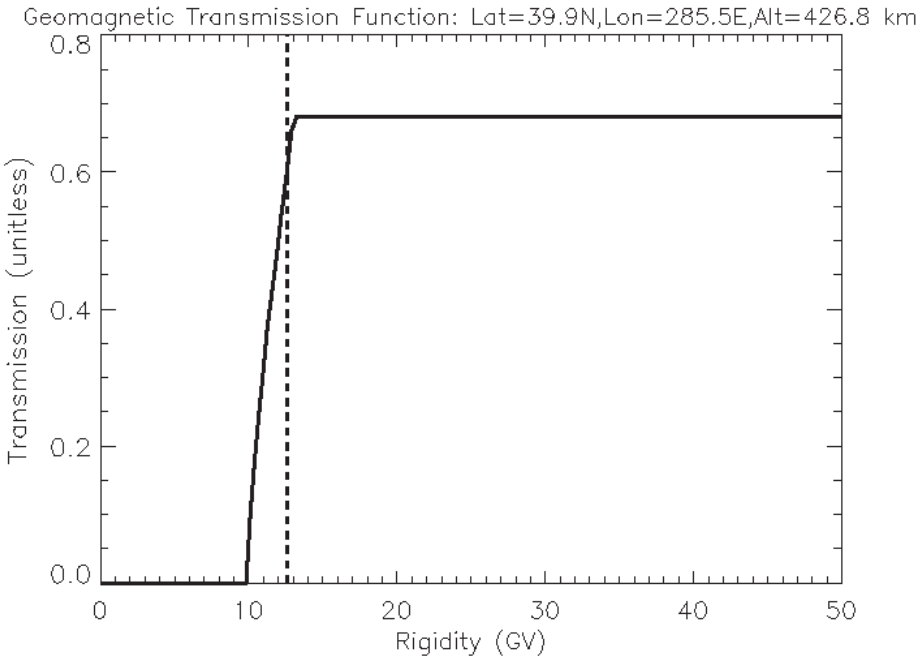

Figure 13. Geomagnetic transmission function at an altitude in the LEO radiation environment. The vertical dashed line denotes the vertical cutoff rigidity.

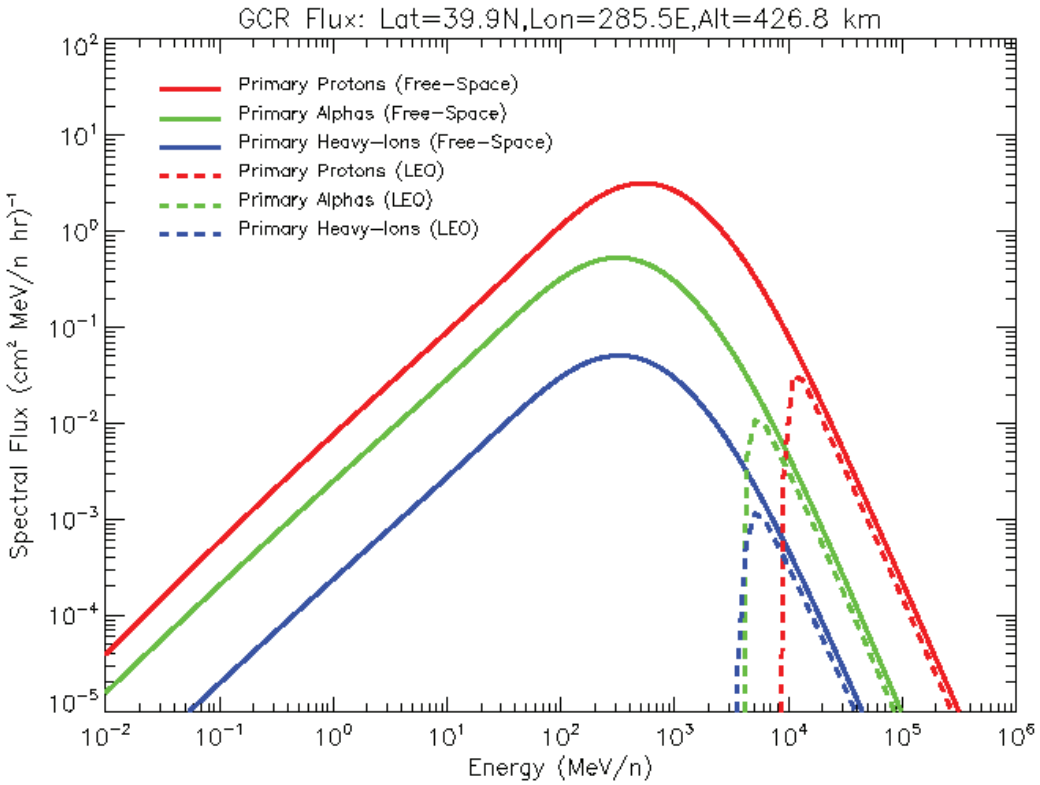

Figure 14. Free-space GCR spectral flux transported through the magnetosphere to an altitude in the LEO radiation environment via the geomagnetic transmission function (see Figure 13). Heavy-ion GCR spectral flux is a sum of GCR spectra for all ions with charge and mass number greater than helium.

8.3 Material Radiation Transport

The transport of ionizing radiation through the atmosphere and aircraft or spacecraft vehicle shielding is calculated using the HZETRN2015 deterministic transport code (Slaba and Stoffle, 2017; and references therein). HZETRN numerically solves the time-independent, coupled, linear Boltzmann transport equations. The transport interaction processes include energy slowing down of the incident projectile and fragmentation ions through ionization and atomic excitation of the material medium, nuclear scattering and attenuation, and the production of secondary particles from nuclear reactions between the projectile ions and the material of the target medium (Mertens et al., 2012). Heavy-ions, pions, muons, and electromagnetic cascade particles are treated within the straight-ahead approximation (Slaba et al., 2013a, 2013b). Neutrons and light-ion transport utilize a bi-directional transport approach in the atmosphere which incorporates albedo neutron contributions (Slaba et al., 2010).

In the previous version of NAIRAS, HZETRN solved coupled transport equations for 59 isotopes to calculate the radiation response functions along each ray direction from the GCR primary source ions. In NAIRAS version 3, the expanded GCR composition described in Section 8.1.1 to calculate LET spectra out to 100 MeV-cm^2/mg requires the solution of 116 coupled transport equations along each ray direction. The pre-computed atomic and nuclear databases utilized by HZETRN were updated to include the ultra-heavy GCR nuclear isotopes in the GCR transport. The transport procedure for SEP heavy-ions is identical to the NAIRAS version 3 GCR transport procedure described above.

The atmospheric ionizing radiation transport in the previous version of NAIRAS implemented a transport scheme along the vertical direction with the GCR or SEP differential flux at the top boundary of the neutral atmosphere approximated by a projection of the directionally isotropic GCR and SEP source differential flux along the vertical direction (Mertens et al., 2013). Measurements taken by the NASA RaD-X balloon flight showed that transport along a single direction in the atmosphere is insufficient at predicting dosimetric quantities at high-altitudes above the commercial aviation radiation environment (Norman et al., 2016). To better characterize the radiation environment of a spaceflight over the entire mission (i.e., from launch to orbit and return), the atmospheric transport in NAIRAS version 3 was updated to include multi-directional transport through the atmosphere. The number of ray directions were optimized by comparing model calculations with RaD-X dosimetric measurements (Mertens et al., 2016b).

The NAIRAS version 3 multi-directional atmospheric ionizing radiation transport approach can be summarized in terms of the directional-integrated flux. This quantity is required to compute the dosimetric quantities (Mertens et al., 2012, 2013) and the new output flux and fluence quantities listed in Table 1 for assessing SEE. In the atmosphere, assuming azimuthal symmetry, the directional-integrated flux for particle type i can be approximated by:

$$\phi_i(\mathbf{r},E) = \int \Phi_i(\mathbf{r},\mathbf{\Omega},E)d\mathbf{\Omega} \approx 2\pi\left[\frac{1}{N}\sum_j \Phi_i(\mathbf{r},u_j,E)\right], \tag{19}$$

where $u_j = \cos\varepsilon_j$ and ε_j is the zenith angle along ray direction j. The integral over zenith direction is discretized into a sum over equal segments in $\cos\varepsilon$. Thus, for N ray directions $\Delta u = 1/N$ such that:

$$\cos\varepsilon_{j+1} = \cos\varepsilon_j - \frac{1}{N} \tag{20}$$

and $\cos\varepsilon_1 = 1$ for the vertical direction. For a given number of ray directions, N, the radiation transport equations are solved along each ray direction given by the zenith angles computed from equation (20). At each altitude in the atmosphere, the differential fluxes along these rays directions are averaged, and including the 2π scale factor, to obtain the directional-integrated flux in equation (19).

The fundamental spatial coordinate in ionizing radiation transport is the areal depth in the material medium, in units of g/cm^2 (Mertens et al., 2012). For atmospheric transport in NAIRAS version 3, the depth at each altitude and ray direction in equation (19) is computed from the U.S. Standard Atmosphere (U.S. Standard Atmosphere, 1976). The thermodynamic variables of the U.S. Standard Atmosphere are shown in Figure 15.

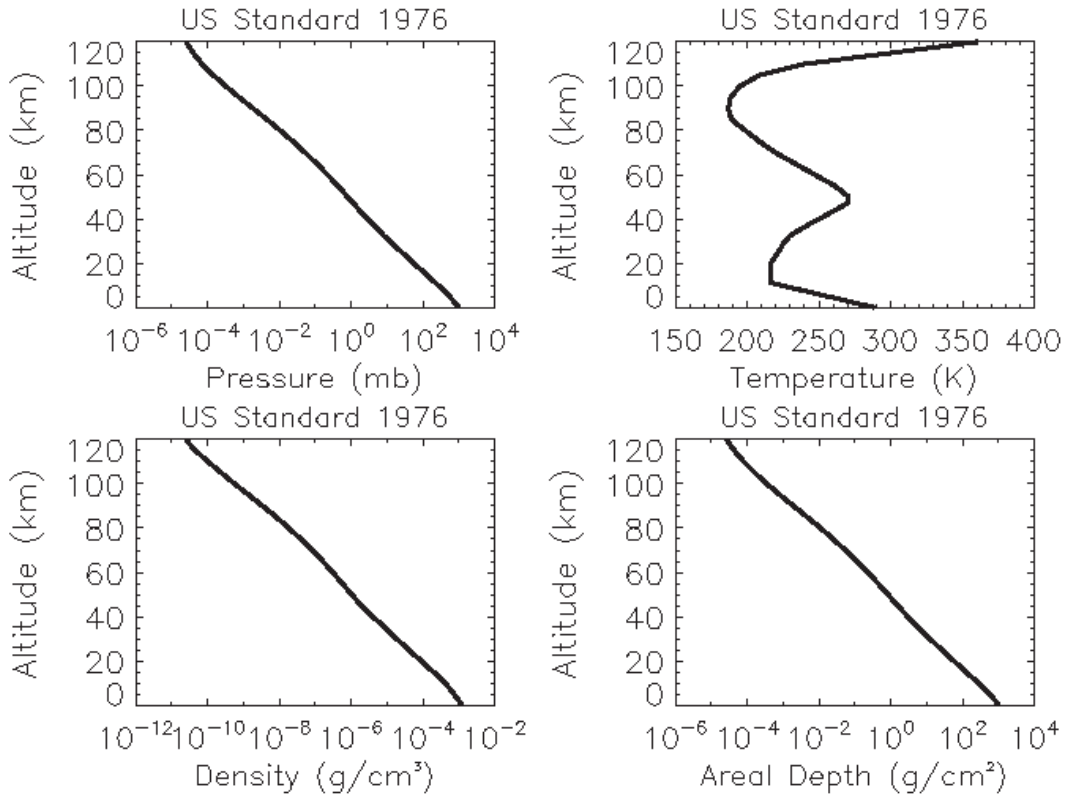

Figure 15. U.S. Standard Atmosphere thermodynamic variables. The areal depth was computed from the pressure, density, and temperature as described in the text.

Within each altitude layer of the U.S. Standard Atmosphere, the pressure is assumed to vary exponentially, the temperature is assumed to vary linearly, and the density is determined from

temperature and pressure at the layer boundary by the ideal gas law in the calculation of atmospheric depth. The atmospheric density is given by:

$$\rho(z) = C_1 \frac{P(z)}{r_a T(z)} \tag{21}$$

where $C_1 = 10^{-4}$ is a conversion factor so that the density, ρ, is in units of g/cm^3, pressure, P, in mbar, and temperature, T, in units of Kelvin. The specific gas constant of air, r_a, is 0.28706 J/K/g. The atmospheric depth at the top of the U.S. Standard Atmosphere is approximated (z_{top}) by:

$$d(z_{top}) = C_2 \rho(z_{top}) H(z_{top}) \ , \tag{22}$$

where H is the atmospheric scale height defined as:

$$H(z) = \frac{r_a T(z)}{g}, \tag{23}$$

and g is the gravitational acceleration 9.80665 m/s^2. The conversion factor $C_2 = 10^5$ in equation (22) ensures that the depth is in units of g/cm^2. Given the depth at the top of the atmosphere in equation (22), the depth at altitude z_N in the U.S. Standard Atmosphere is approximated by the sum of increments of depth for each subsequent vertical layer, such that:

$$d(z_N) = \sum_{i=2}^{N} \Delta d(z_i) + d(z_{top}) \tag{24}$$

where the increment in depth from an atmospheric layer is computed explicitly by:

$$\Delta d(z_i) = \int_{z_i}^{z_{i-1}} \rho(z) dz \tag{25}$$

and $z_{i-1} > z_i$.

Given the variation in the thermodynamic variables described is this section, the following expression for the incremental depth is derived:

$$\Delta d(z_i) = C_2 \frac{\rho(z_{i-1})(z_{i-1} - z_i)}{\gamma\left[1 - \left(T(z_i)/T(z_{i-1})\right)\right]}\left[\left(\frac{T(z_i)}{T(z_{i-1})}\right)^{-\gamma} - 1\right], \tag{26}$$

where:

$$\gamma = \frac{z_{i-1} - z_i}{H(z_{i-1}) - H(z_i)}. \tag{27}$$

Note that equation (26) becomes ill-defined in isothermal regions of the atmosphere. In the U.S. Standard Atmosphere shown in Figure 15, the isothermal regions are near the tropopause and

stratopause. The following expression is derived for the incremental depth of an isothermal atmospheric layer:

$$\Delta d(z_i) = C_2 \rho(z_{i-1}) H(z_{i-1}) \left[\exp\left(\frac{z_{i-1} - z_i}{H(z_{i-1})} \right) - 1 \right] . \tag{28}$$

The expressions for the atmospheric depth (i.e., equation (26) and equation (28)) were derived for vertical layers, or equivalently, for zenith angle equal to zero, $\varepsilon = 0$. For off-vertical ray directions, as is needed in computing the directional-integrated flux in equation (19), the layer thicknesses, $z_{i-1} - z_i$, in equations (26) to (28) are replaced by the layer slant path thickness Δs_i, which can be derived from geometry and given by:

$$\Delta s_i^2 = (\mathrm{Re} + z_i)^2 + (\mathrm{Re} + z_{i-1})^2 - 2(\mathrm{Re} + z_i)(\mathrm{Re} + z_{i-1}) \cos(\varepsilon - \eta) , \tag{29}$$

where:

$$\sin\eta = \sin\varepsilon \left(\frac{\mathrm{Re} + z_i}{\mathrm{Re} + z_{i-1}} \right) . \tag{30}$$

and Re is the average Earth radius (6371.2 km).

The multi-directional atmospheric ionizing radiation transport approach described is this section made a significant improvement in predicting the dosimetric quantities at altitudes above the commercial aviation radiation environment. A comparison between the NAIRAS model predictions of absorbed dose rate and corresponding measurements taken during the RaD-X high-altitude balloon flight is shown in Figure 16 (Mertens et al., 2016b). The NAIRAS version 3 model calculations of absorbed dose rate in tissue agree with the tissue-equivalent proportional counter (TEPC) instrument to within ~8% in RaD-X science region A (21 to 27 km) and within ~ 15% in region B (> 32.5 km). The RaD-X campaign consisted of a high-altitude balloon flight, NASA ER-2 and Cessna Conquest II aircraft flights, and coordinated aircraft measurements taken onboard a commercial Lufthansa flight (Mertens et al., 2016b). The RaD-X campaign flight measurements included absorbed dose in silicon, absorbed dose in tissue, dose equivalent, and ambient dose equivalent covering seven altitude regions from 0-40 km. Extensive NAIRAS/RaD-X comparisons showed that six ray directions, $N = 6$, provide sufficient accuracy in the multi-directional atmospheric ionizing radiation transport procedure to maintain the NAIRAS model dosimetric predictions to within 30% of the RaD-X flight measurements, which is within measurement uncertainty. The details of the NAIRAS/RaD-X validation study will be reported in a future publication.

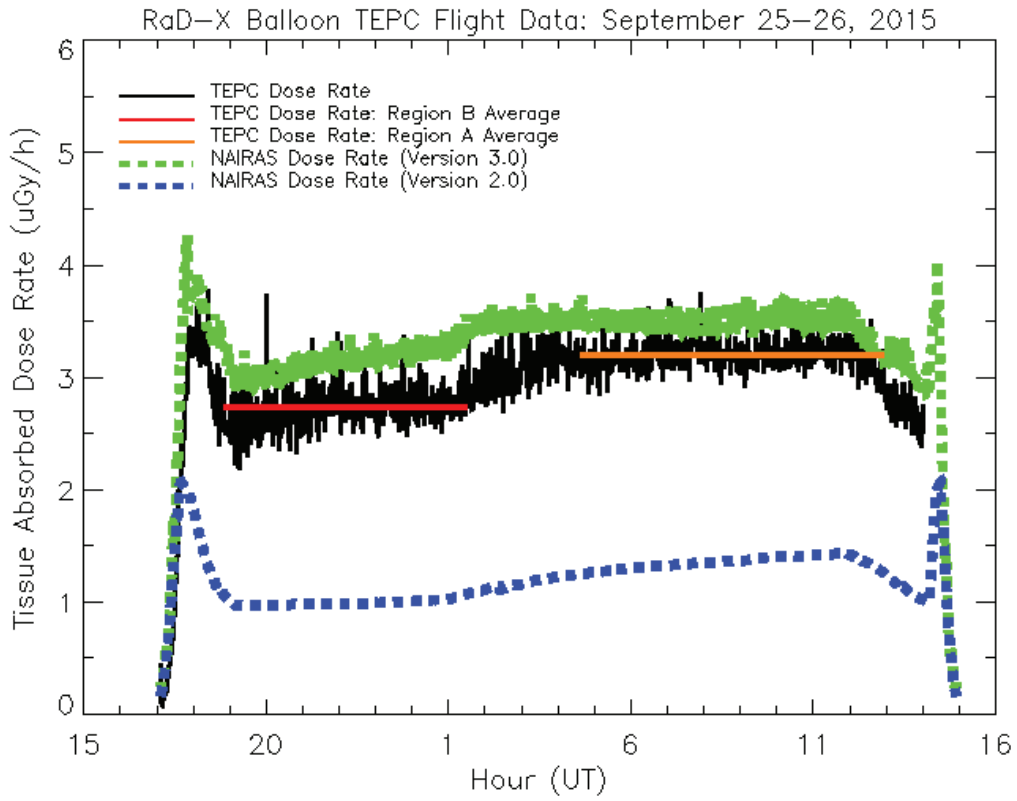

Figure 16. Comparison of NAIRAS predictions of absorbed dose rates in tissue with TEPC measurements taken during the NASA RaD-X high-altitude balloon flight.

9.0 NAIRAS Model RoR Output

Presented in this section are new NAIRAS version 3 results with emphasis on the extension of the model domain to the geospace and free-space radiation environments. Examples of the dosimetric and new radiative flux and fluence quantities at a LEO altitude and for the actual ISS trajectory are shown in Section 9.1. Dose comparisons between NAIRAS and the Automated Radiation Measurements for Aerospace Safety (ARMAS) dosimeter on ISS are also shown in Section 9.1. Dose comparisons between NAIRAS predictions and NASA Exploration Flight Test 1 (EFT-1) flight measurements at MEO are presented in Section 9.2. Preliminary results of NAIRAS predictions in cislunar orbit during the recent NASA Artemis 1 flight mission are shown in Section 9.3.

9.1 Low-Earth Orbit

A LEO flight trajectory comparable to the ISS orbit was constructed to benchmark the new features of NAIRAS version 3, especially the extension of the model from the atmosphere to the geospace environment. The example flight trajectory has an orbital inclination of 51.6° and an altitude of 400 km. The datetime of the trajectory is the 24-hour period from November 2, 2003, 16:00 UT to November 3, 2003, 16:00 UT. This time period is during the Halloween 2003 SEP events and includes GLE 67 and a geomagnetic storm for testing a wide range of space weather phenomena in the NAIRAS RoR flight trajectory run option. The flight trajectory as a function of geographic latitude and longitude for the 24-hour period is shown in Figure 17. The trajectory points have a uniform 1-minute time resolution.

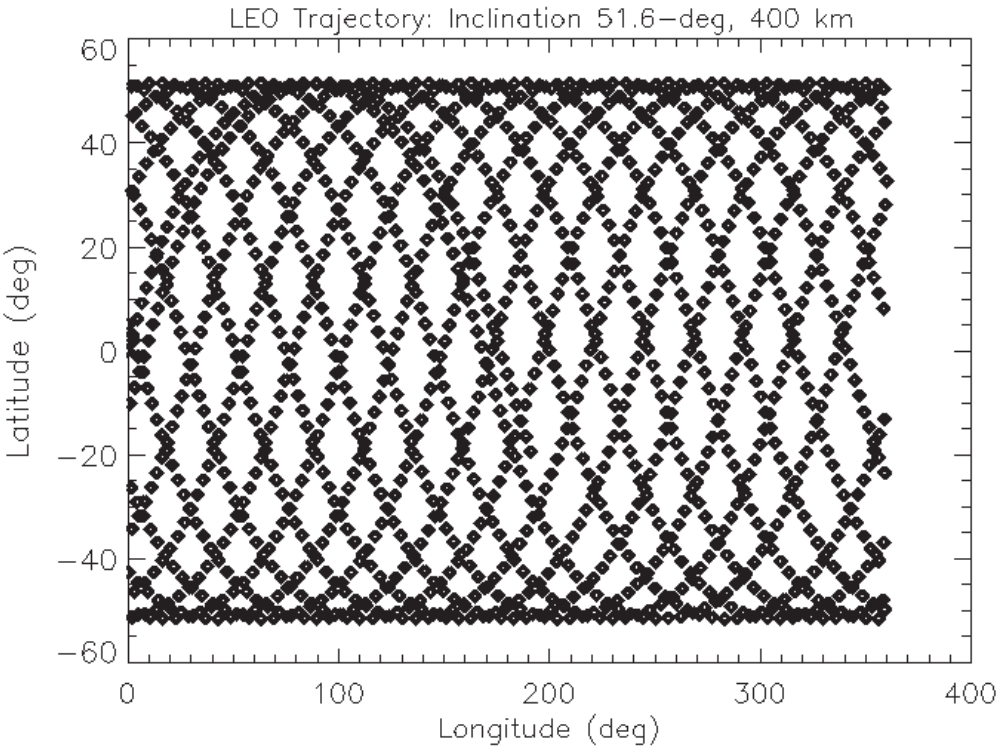

Figure 17. Example LEO flight trajectory points used to test the new NAIRAS version 3 output products for the RoR flight trajectory run option. The figure shows the trajectory points for a 24-hour period with uniform 1-minute temporal resolution.

The effective dose rates for the example LEO flight trajectory are shown in Figure 18. A fictitious launch phase for the trajectory was added at the beginning of the example flight to test the new atmospheric ionizing radiation transport procedures discussed in Section 8.3. This launch phase can be seen in the effective GCR dose rates in Figure 18. The example LEO flight trajectory passes through the SAA five times in the 24-hour period and crosses the edge of the SAA near the end of the orbit period, which is evident in the effective dose rates from TRP-p. The SEP dose is also evident at the highest latitude points along the trajectory. The dose rates were calculated for a spacecraft shielding of 50 g/cm^2 aluminum, which is consistent with the median aluminum-equivalent shielding distributions surrounding ISS radiation detectors (Badavi et al., 2011; Slaba et al., 2020b). The dose from TRP-e is too small to be seen in this figure or detected by dosimeters at a shielding depth of 50 g/cm^2. The time-integrated flight effective dose for the 24-hour period for the GCR and TRP-p sources are 223 μSv and 139 μSv, respectively, with a GCR + TRP combined total of 362 μSv. The NAIRAS model results in Figure 18 are for one day in the downward side of solar cycle 23, which included a recovering Forbush decrease during GLE 67 (Mertens et al., 2010a, 2012). Nevertheless, these results are consistent with solar cycle averaged daily total effective dose of 438 μSv reported by Cucinotta et al. (2008), and the GCR and TRP-p daily total effective doses of 233 μSv and 166 μSv, respectively, near solar cycle minimum reported by Wu et al. (1996). The total SEP effective dose computed by NAIRAS for this 24-hour period is 35 μSv. The SEP heavy-ions ($Z \geq 2$) increased the SEP total effective dose for this benchmark trajectory and time period by over 40% compared to SEP total effective dose from SEP protons only (Mertens et al., 2024).

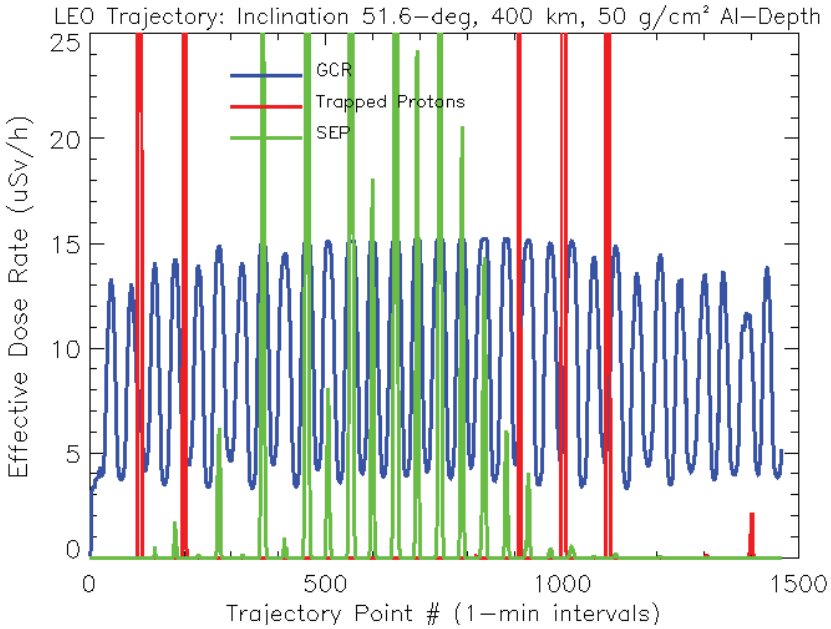

Figure 18. NAIRAS version 3 calculations of effective dose rates for the LEO flight trajectory shown in Figure 17. The datetime of the trajectory at the altitude of 400 km is the 24-hour period from November 2, 2003 16:00 UT to November 3, 2003 16:00 UT. A fictitious launch phase was added to the beginning of this example flight. The spacecraft shielding is 50 g/cm^2 aluminum.

The effective dose rates for 2 g/cm^2 aluminum shielding are shown in Figure 19. The dose rates were calculated for the same example LEO trajectory shown in Figure 17. Recall from Section 8.1.2.2 that a shielding thickness of 2 g/cm^2 aluminum-equivalent is representative of spacesuit shielding of an astronaut performing an ISS EVA. At this depth, the effective dose in Figure 19 is dominated by TRP-p and SEP, although an actual EVA would be scheduled to avoid passages through the SAA where exposure from the TRP-p source is received. Exposure from TRP-e is evident in Figure 19 at certain passages through the SAA and at certain high-latitude crossings. The time-integrated flight effective dose for the 24-hour period for the GCR and TRP-p sources are 355 µSv and 1.1 mSv, respectively. The total SEP flight effective dose computed by NAIRAS for this 24-hour period is 4.4 mSv. The total flight effective dose from TRP-e is 81 µSv.

Vertical cutoffs shown in Figure 20 at the example flight trajectory points in Figure 17 are computed in two ways: 1) using just the IGRF, and 2) the internal magnetic field plus the magnetospheric magnetic field contributions using the TS05 model (IGRF + TS05). Recall from Section 8.2 that the spectral filtering of GCR and SEP ions by the geomagnetic field is a function of the vertical cutoff rigidity. The time period for the cutoff calculations is the same as for the effective dose rates shown in Figures 17 and 18. During this time, the geospace environment is recovering from the enhanced geomagnetic activity from the Halloween 2003 storm events. The effect of geomagnetic storm activity is to suppress the cutoff rigidity (Kress et al., 2010; Mertens et al., 2010a), which in turn increases the GCR and SEP dosimetric and flux and fluence quantities. The cutoff rigidity suppression is greatest at high latitudes and varies with each geomagnetic storm. All the NAIRAS version 3 output products presented in Section 9.0 are based on including the dynamical response of the geomagnetic field by computing vertical cutoff rigidities using the internal field plus the TS05 magnetospheric magnetic field model, as described in Section 8.2.

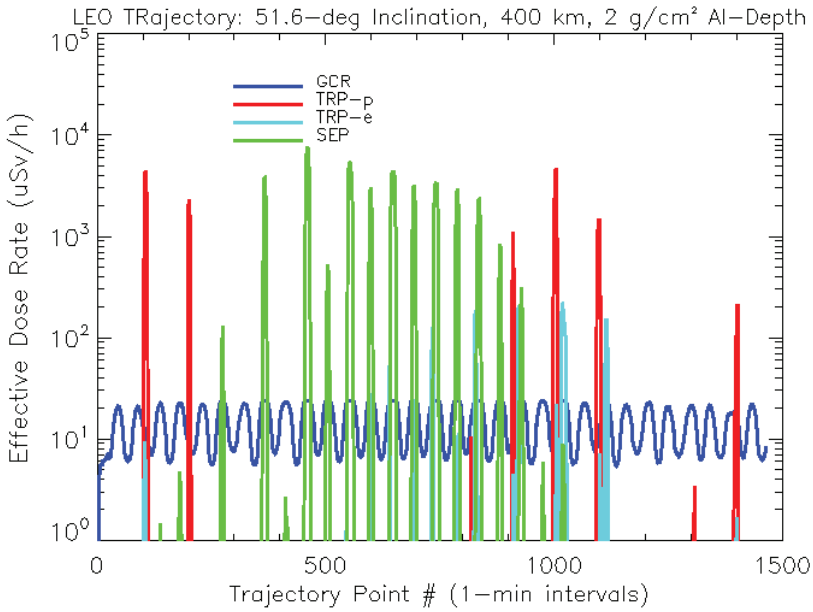

Figure 19. NAIRAS version 3 calculations of effective dose rates for the LEO flight trajectory shown in Figure 17. The datetime of the trajectory at the altitude of 400 km is the 24-hour period from November 2, 2003 16:00 UT to November 3, 2003 16:00 UT. A fictitious launch phase was added to the beginning of this example flight. The spacecraft shielding is 2 g/cm² aluminum.

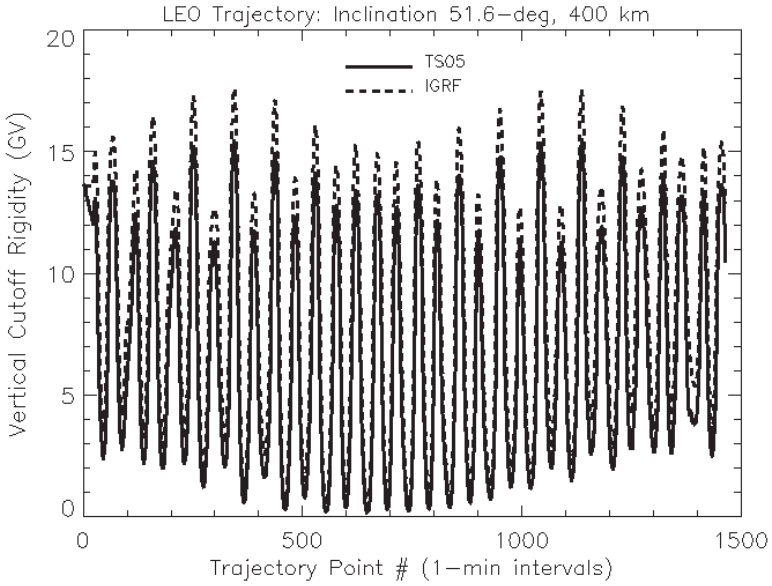

Figure 20. NAIRAS version 3 vertical geomagnetic cutoff rigidities for the LEO flight trajectory shown in Figure 17. The datetime of the trajectory at the altitude of 400 km is the 24-hour period from November 2, 2003 16:00 UT to November 3, 2003 16:00 UT. The dashed line shows cutoff rigidities computed using the internal Earth magnetic field only (IGRF). The solid line shows cutoff rigidities computed using both internal and dynamic magnetospheric magnetic field models (IGRF + TS05).

The next three figures are examples of NAIRAS version 3 differential and integral flux and fluence quantities that are used in radiation effects models to assess SEE. The differential GCR, SEP, and TRP-p LET fluence for the example LEO flight trajectory are shown in Figure 21. Recall from Section 8.1.1 that the ultra-heavy ion composition of the GCR spectrum is

responsible for the flux contributions at LET greater than 31.9 MeV-cm^2/mg, which includes energy deposit contributions of copper to uranium GCR nuclear isotopes. This is true for the ultra-heavy ion composition of the SEP spectrum, as seen in Figure 21. Predicting the LET spectrum of the radiation environment is an important capability of the NAIRAS model because SEE heavy-ion cross sections are parameterized by LET (European Cooperation for Space Standardization, 2010). The NAIRAS model output also includes differential LET spectra from the TRP sources. The TRP differential LET output flux and fluence quantities enable model validation comparisons against LET spectrometer measurements, as shown in Section 9.2. The differential TRP-e LET fluence was also calculated for the LEO flight trajectory of Figure 17, but the LET from the TRP-e source is less than 0.1 MeV-cm^2/mg and the fluence is orders of magnitude less than the three other sources shown in Figure 21.

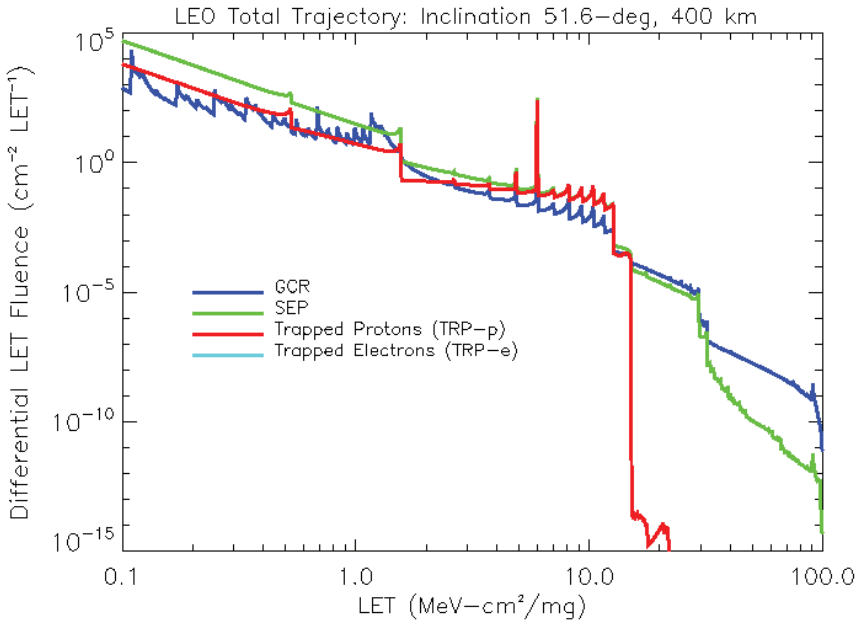

Figure 21. NAIRAS version 3 calculation of GCR, SEP, and TRP-p differential LET fluence for the LEO flight trajectory shown in Figure 17. The datetime of the trajectory at the altitude of 400 km is the 24-hour period from November 2, 2003 16:00 UT to November 3, 2003 16:00 UT. The spacecraft shielding is 4 g/cm^2 aluminum. The TRP-e LET fluence was calculated too but doesn't contribute to LET greater than 0.1 MeV-cm^2/mg.

The typical variation of SEE heavy-ion cross sections with LET is characterized by a distinct LET threshold followed by a rapid increase in cross section value which saturates to a constant value as a function of LET (European Cooperation for Space Standardization, 2010). In this case, integral LET flux and fluence quantities are sufficient to characterize SEE. As an example, the GCR and SEP integral LET flux are shown in Figure 22 for the flight trajectory of Figure 17. The user-input, threshold LET for this integral flux quantity is >1 MeV-cm^2/mg. The spacecraft shielding in these examples is 4 g/cm^2 aluminum (i.e., Figures 21 through 23), consistent with a lightly shielded aircraft or spacecraft (Singleterry et al., 1999). The SEP integral flux exceeds the GCR integral flux by a maximum factor of 115 over the 24-hour period shown in Figure 22.

SEE proton cross sections are parameterized as a function of proton energy (European Cooperation for Space Standardization, 2010). Thus, the NAIRAS model predictions of SEP and

TRP-p differential fluence for the example LEO flight trajectory are shown in Figure 23. The TRP-e differential fluence is also shown in this figure for comparison.

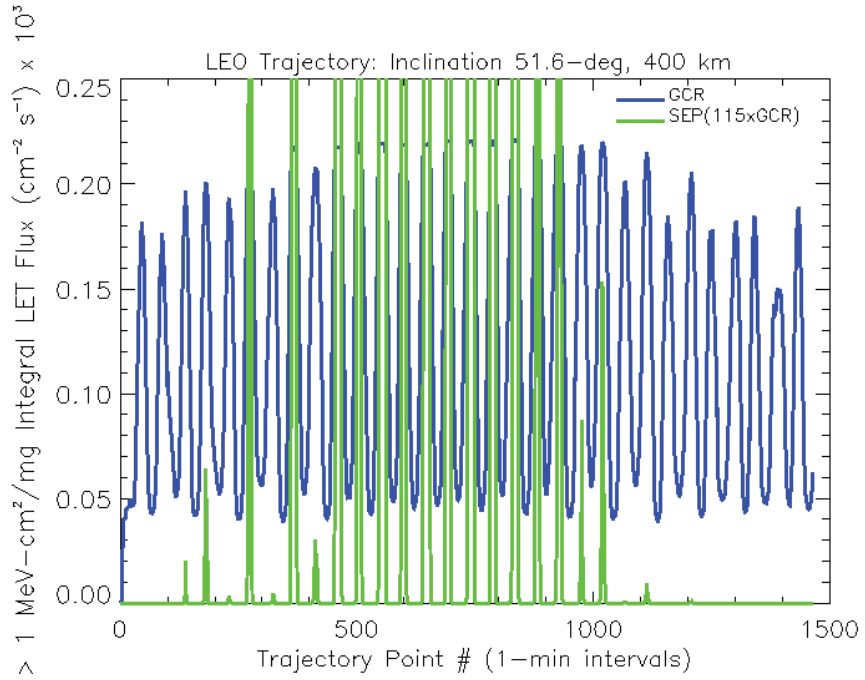

Figure 22. NAIRAS version 3 calculation of GCR and SEP integral LET flux for the LEO flight trajectory shown in Figure 17. The datetime of the trajectory at the altitude of 400 km is the 24-hour period from November 2, 2003 16:00 UT to November 3, 2003 16:00 UT. The spacecraft shielding is 4 g/cm² aluminum. The SEP integral flux exceeds the GCR integral flux by a maximum factor of 115.

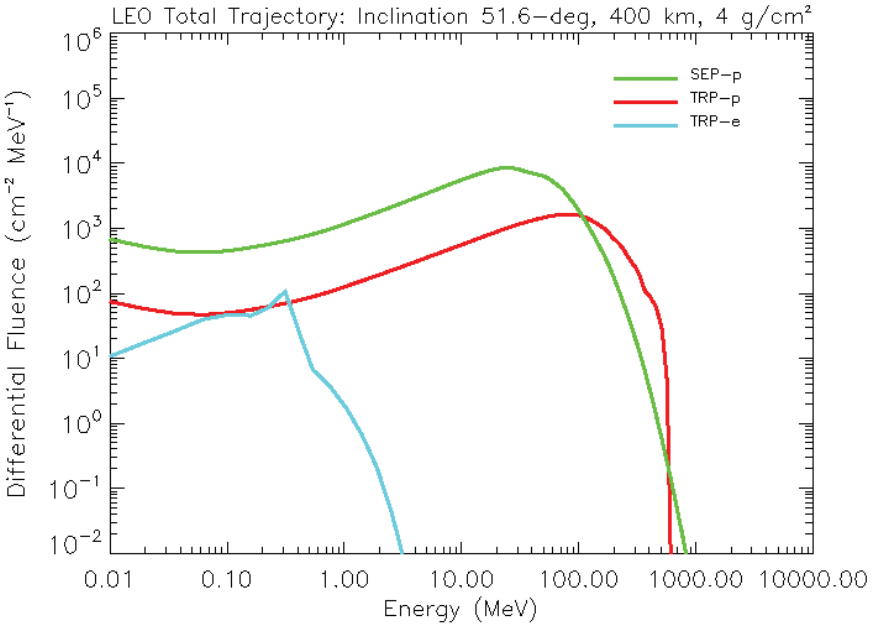

Figure 23. NAIRAS version 3 calculation of SEP, TRP-p, and TRP-e differential fluence spectra for the LEO flight trajectory shown in Figure 17. The datetime of the trajectory at the altitude of 400 km is the 24-hour period from November 2, 2003 16:00 UT to November 3, 2003 16:00 UT. The spacecraft shielding is 4 g/cm² aluminum.

The next phase in the testing and verification of the model updates in NAIRAS version 3 is to characterize the LEO radiation environment for the actual ISS trajectory and for more extended time periods. Thus, the next series of figures are NAIRAS version 3 predictions calculated at the ISS orbit during the December 13 through 16, 2006, SEP events. The ISS trajectory was constructed using python-spg4 and the orbital parameters obtained from the two-line element (TLE) database (space-track.org). The ISS altitude varied between 330 and 360 km over this 4-day period. These SEP events occurred during the annual Fall American Geophysical Union (AGU) meeting and are often referred to the AGU 2006 SEP events. This time period is interesting because ISS experienced a significant attitude control anomaly on December 15, 2006, due to space weather phenomena associated with the AGU 2006 SEP events. The anomaly was attributed to increased atmospheric drag which exceeded the capability of the Control Moment Gyroscope (CMG) system, requiring thrusters to be used instead. There is no reported evidence of increased SEE rates due to the AGU 2006 SEP radiation enhancement (Koontz et al., 2018). Nevertheless, this event is a good test case to demonstrate the capability of NAIRAS to capture the temporal-spatial variability of the actual space radiation environment, which is needed to quantitatively characterize and assess spacecraft system anomalies.

The effective dose rates for 50 g/cm^2 aluminum shielding at the ISS orbit during the AGU 2006 SEP events are shown in Figure 24 for a 4-day period between December 13 and 16, 2006. GLE 70 occurred on December 13, 2006 (https://gle.oulu.fi), which corresponds to the largest SEP doses in Figure 24. The largest TRP-p dose rates occur when the ISS orbit crosses the SAA region. The low-frequency modulations in the GCR dose rates are due to the disturbed interplanetary plasma and IMF (e.g., data from King and Papatashvilli (2013)). The total GCR and TRP-p effective doses over the 4-day period are 1.5 mSv and 259 µSv, respectively, with the combined total effective dose (GCR + TRP-p) of 1.8 mSv. The total SEP effective dose over the 4-day period is 436 µSv, which is roughly 25% of the combined GCR + TRP-p dose. The TRP-e effective dose rates are negligible at a shielding depth of 50 g/cm^2 aluminum-equivalent.

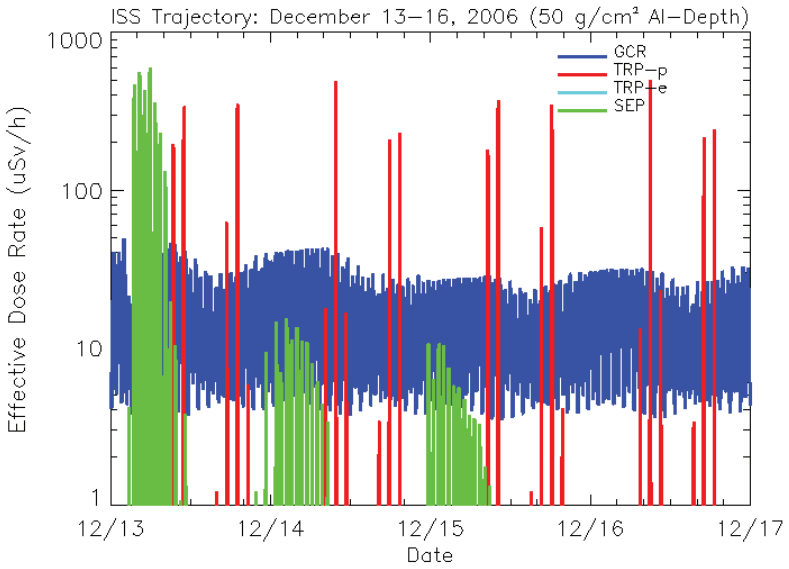

Figure 24. NAIRAS version 3 calculation of effective dose rates at the ISS orbit from December 13 through 16, 2006. The spacecraft shielding is 50 g/cm^2 aluminum.

The effective dose rates representative of astronaut EVA exposure (2 g/cm^2 aluminum-equivalent shielding) are shown in Figure 25 at the ISS orbit for the AGU 2006 SEP events. The

contributions from the TRP-e source are now discernable in the figure for certain passages through the SAA and for certain high-latitude crossings. The total GCR and TRP-p effective doses over the 4-day period between December 13 and 16, 2006, are 2.5 mSv and 3.3 mSv, respectively. The total TRP-e effective dose is approximately 5% of the total TRP-p effective dose. The combined background (GCR + TRP-p + TRP-e) total effective dose is 6.0 mSv. The total SEP effective dose over the 4-day period is 15 mSv.

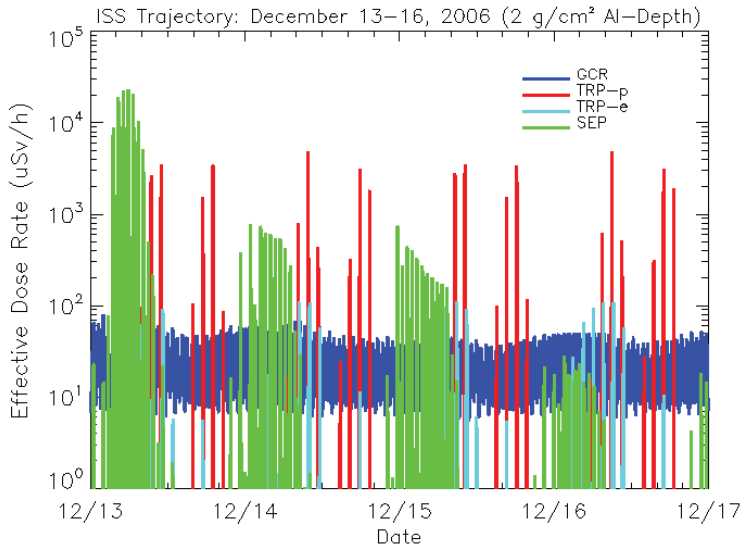

Figure 25. NAIRAS version 3 calculation of effective dose rates at the ISS orbit from December 13 through 16, 2006. The shielding thickness is 2 g/cm² aluminum.

Integral GCR and SEP LET flux are shown in Figure 26 at the ISS orbit for December 13 through 16, 2006, during the AGU 2006 SEP events. This quantity is an example integral flux quantity that is needed for assessing SEE rates in some space vehicle systems. The integral SEP LET flux is elevated above the integral GCR flux for most high-latitude crossings of the ISS. The maximum enhancement of the integral SEP LET flux above the integral GCR flux is a factor of 90. One of the important features of the NAIRAS model is the ability to capture the actual dynamical variability of the ionizing radiation environment. The integral LET flux has the same low-frequency modulations as the GCR effective dose rates in the previous plots. This appears to be the consequence of a combination of the arrival of an interplanetary shock late on December 14, 2006, and the large scale variability in the IMF components which were also associated with a Forbush decrease (e.g., data from King and Papatashvilli, (2023)).

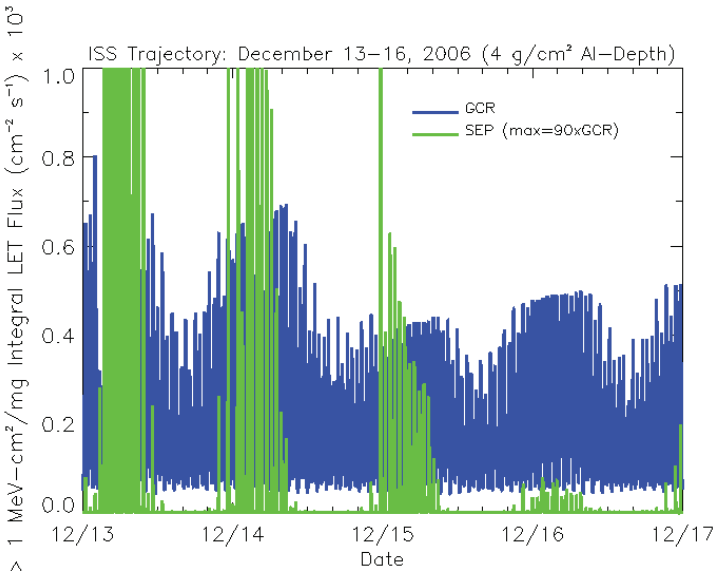

Figure 26. NAIRAS version 3 calculation of integral LET flux at the ISS orbit from December 13 through 16, 2006. The spacecraft shielding is 4 g/cm² aluminum. The SEP integral flux exceeds the GCR integral flux by a maximum factor of 90.

The SEP integral proton flux is shown in Figure 27 at the ISS orbit during the AGU 2006 SEP events. The SEP integral proton flux quantities are useful inputs to radiation effects models for predicting SEE rates from protons during SEP events. The user-input, threshold energy levels were chosen to match GOES integral proton flux channels. The results in Figure 27 show that the high-energy tail of the SEP spectrum (> 500 MeV) was elevated during the first SEP event in the series of events that occurred over this 4-day storm period, corresponding to GLE 70, and subsequently decayed quite rapidly thereafter.

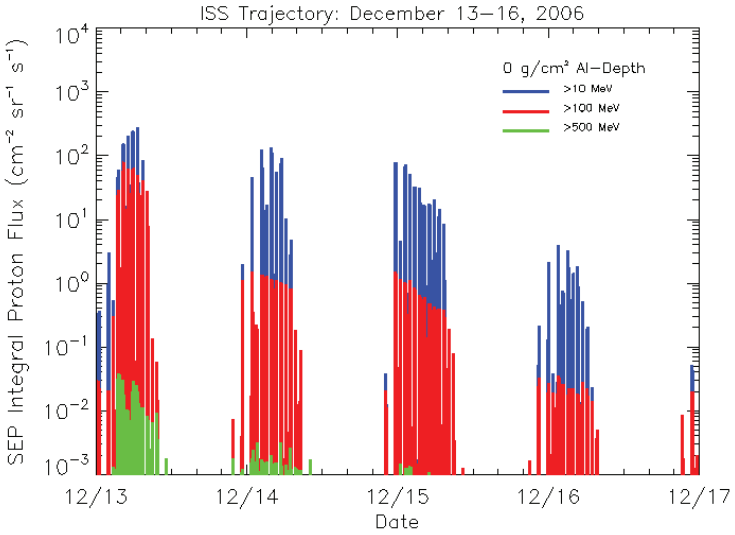

Figure 27. NAIRAS version 3 calculation of SEP integral proton flux at the ISS orbit from December 13 through 16, 2006. The integral flux is shown at several threshold energies and at zero shielding depth.

The SEP proton, TRP-p, and TRP-e differential fluence are shown in Figure 28 at the ISS orbit over the 4-day period from December 13 through 16, 2006, during the AGU 2006 SEP events.

The peak SEP proton and TRP-p fluence both occur at an energy of about 100 MeV. The SEP proton and TRP-p fluence spectra are quite similar in shape with the SEP proton fluence exhibiting a slightly harder spectrum at relativistic energies (> 500 MeV). The TRP-e fluence spectrum peaks at about 0.3 MeV, and the fluence of relativistic electrons (> 0.5 MeV) decrease rapidly. These features are comparable to the Halloween 2003 SEP event (GLE 69) benchmark case shown in Figure 23.

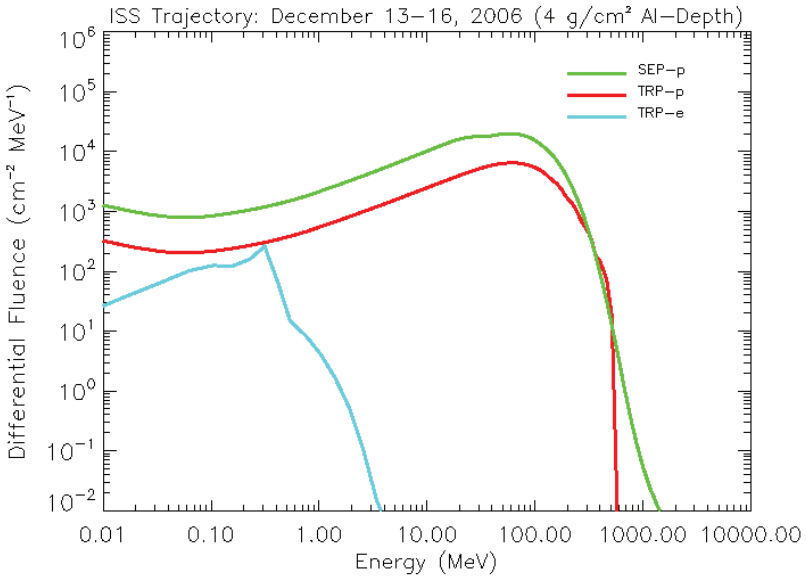

Figure 28. NAIRAS version 3 calculation of SEP proton, TRP-p, and TRP-e differential fluence spectra at the ISS orbit from December 13 though 16, 2006. The spacecraft shielding is 4 g/cm² aluminum.

The ARMAS dosimeter flight unit, originally developed for continuous aircraft radiation monitoring, was recently deployed on the ISS (cf., Tobiska et al., 2016; Tobiska et al., 2018), which uses calibrations to ground-based beam lines (Gersey et al., 2020). The dosimeter was placed outside the Japanese Experiment Module (JEM) and collected data from March 3, 2002, through December 12, 2022. The shielding thickness of the dosimeter is 100 mils (0.1 inch) of aluminum. The initial comparisons between the ARMAS ISS measurements and NAIRAS version 3 predictions are shown in Figure 29 for October 6, 2022 (Mertens et al. 2024). The accumulated total (GCR + TRP) dose over this 24-hour period is 992.4 µGy and 621.4 µGy as determined by NAIRAS and ARMAS, respectively. The NAIRAS model overpredicts the accumulated dose by about 60%. The comparisons in Figure 29 are representative of the other 207 days for which ARMAS operated on ISS. The trajectory point-by-point differences in Figure 29 show that NAIRAS overestimates the TRP-p exposure and underestimates the GCR exposure at high latitudes. The NAIRAS high-latitude underestimation, of what appears to be GCR exposure, is by as much as an order of magnitude for orbital passes after 15:00 UT.

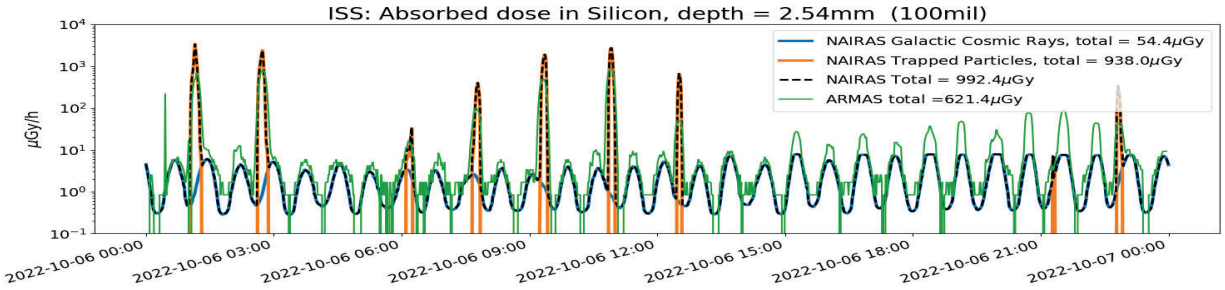

Figure 29. NAIRAS version 3 dose calculations and comparisons to ARMAS measurements at ISS from October 6, 2022. ARMAS dosimeter shielding is 0.1 inch of aluminum. The radiation sources included in NAIRAS for this calculation are GCR and TRP-p.

The NAIRAS model underestimation of absorbed dose in silicon compared to the lightly shielded ARMAS dosimeter attached to the ISS JEM, as shown in Figure 29, was identified as due to the TRP-e source. Achieving agreement between NAIRAS predictions and 2022 ARMAS ISS measurements was the primary motivation for integrating the TRP-e model into NAIRAS version 3, as previously discussed in Section 8.1.4. It was also shown in this section that the TRP-e source contributes on the order of 5% to the effective dose received by astronauts on EVA. The updated comparison between NAIRAS and ARMAS on ISS is presented in Figure 30. The NAIRAS predictions with the TRP-e model included have improved agreement with ARMAS at the ISS high-latitude crossings after 15:00 UT. The outer belt TRP-e flux is highly variable, which is evident in the ARMAS dosimeter measurements at the high-latitude crossings. The GEOFFB TRP-e model does not capture short-time scale dynamical processes. Future work will explore improving the dynmical response of TRP-e model at short time scales. Overall, the NAIRAS model now overpredicts the accumulated daily dose by 20%, reducing the model uncertainty by 40%. By comparing NAIRAS predictions with the dose measurements for the entire 208 days of ARMAS operations on ISS, the scale factor of 0.1 applied to the AE8 TRP-e flux presented in Section 8.1.4 was determined.

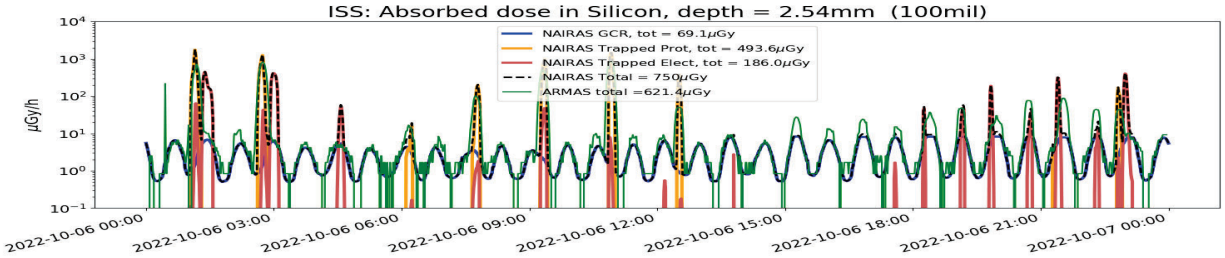

Figure 30. NAIRAS version 3 dose calculations and comparisons to ARMAS measurements at ISS for October 6, 2022. ARMAS dosimeter shielding is 0.1 inch of aluminum. The radiation sources included in NAIRAS for this calculation are GCR, TRP-p, and TRP-e.

The R3DR2 instrument, which is a Liulin-type dosimeter-spectrometer, also obtained measurements outside the ISS on the European Space Agency (ESA) EXPOSE-R2 platform (Dachev et al., 2016). The detector shielding is roughly 0.1 inch of aluminum. The R3DR2 operated on ISS from October 24, 2014, through January 11, 2016. R3DR2 observed a S2-class SEP event in June 2015. The SEP absorbed doses in silicon were elevated by several orders of magnitude above GCR levels. The SEP event was spectrally soft since none of the dosimeters within the ISS, including another Liulin-type dosimeter, detected an enhancement in the ionizing radiation environment above the background GCR. The NAIRAS model predictions are

compared to the R3DR2 measurements during the June 2015 SEP event, as shown in Figure 31. This comparison is the first validation of the NAIRAS model during a SEP event. The agreement is quite good, which requires both an accurate SEP spectral fitting algorithm and an accurate dynamical geomagnetic cutoff rigidity model.

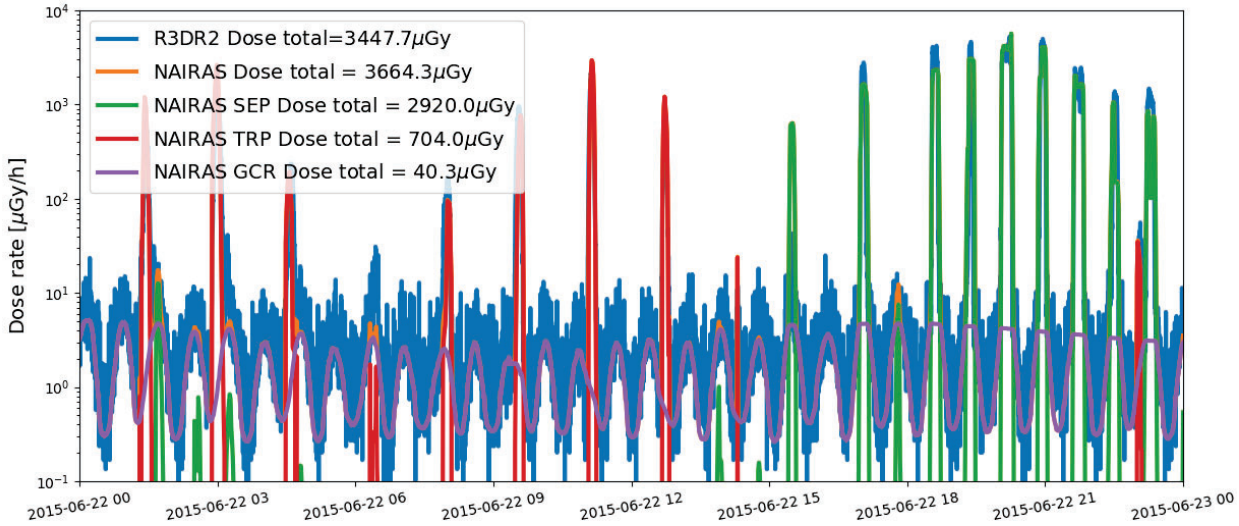

Figure 31. NAIRAS version 3 dose calculations and comparisons to R3DR2 measurements at ISS for June 2015. R3DR2 dosimeter shielding is 0.1 inch of aluminum. The radiation sources included in NAIRAS for this calculation are GCR, TRP-p, TRP-e, and SEP. The SEP event validation is ascertained by comparing the NAIRAS green line with the R3DR2 blue line.

9.2 Medium-Earth Orbit

The NASA MPCV Program EFT-1 was the first unmanned flight (Gaza et al., 2017). EFT-1 was launched on December 5, 2014, into a high eccentricity orbit through the radiation belts with a high apogee of ~6000 km, orbital inclination of 28.6°, and a total mission duration of 4.5 hours. One of the radiation detector systems flown on EFT-1 was a pair of identical active semiconductor detectors, based on imaging radiation Timepix technology, which was integrated into the Battery-operated Independent Radiation Detector (BIRD) system. The two identical detectors, which are housed within the same mechanical enclosure, are referred to as BIRD Left and BIRD Right (Gaza et al., 2017). Postflight analysis algorithms and calibration factors were applied to convert the raw Timepix pixel measurements to absorbed dose in silicon (Bahadori et al., 2015). An additional energy-dependent calibration factor was applied to convert absorbed dose in silicon to absorbed dose in water (Bahadori et al., 2015), which is a proxy for absorbed dose in tissue.

The two BIRD detector measurements of absorbed dose rate in water during the EFT-1 flight are shown in Figure 32 along with corresponding NAIRAS version 3 dosimetric results. NAIRAS absorbed dose rate in tissue is the quantity most directly comparable to the BIRD absorbed dose rates in water. The altitude profile of the EFT-1 flight is shown in Figure 33. The average difference between the NAIRAS predictions of absorbed dose in tissue and the BIRD measurements of absorbed dose in water is 60%. The radiation environment for the time period before 14:00 UT on December 5, 2014, is GCR. The flight altitudes prior to 14:00 UT vary between approximately 300 km and 1000 km, as indicted by the flight altitudes shown in Figure 33. For time periods later than 14:00 UT, the spacecraft passes through the peak flux intensity of

the TRP-p source on the ascent phase of the flight before reaching an apogee of approximately 6000 km. On the decent phase, the spacecraft passes through the TRP-p source again. The two peak dose rates in Figure 32 correspond to the two flight passes through the TRP-p source, which is evident by comparing the dose rates in Figure 32 with the dose-altitude results in Figure 33. The 60% difference between the NAIRAS predictions and the BIRD measurements occurs in both the GCR radiation environment of the flight (time-periods earlier than 14:00 UT) and the TRP-p radiation environment of the flight (time-periods later than 14:00 UT). NAIRAS agrees with previous measurements to within 30% for GCR conditions (Mertens et al., 2013; Meier et al., 2018). The BIRD measurements of accumulated flight dose in water are about 20% higher than other dosimeter systems onboard the EFT-1 flight (Gaza et al., 2017). Considering this as a systematic bias in the BIRD measurements, NAIRAS predictions underestimate BIRD dose data by about 40%. This is very close to the known 30% uncertainty in the NAIRAS GCR dose predictions.

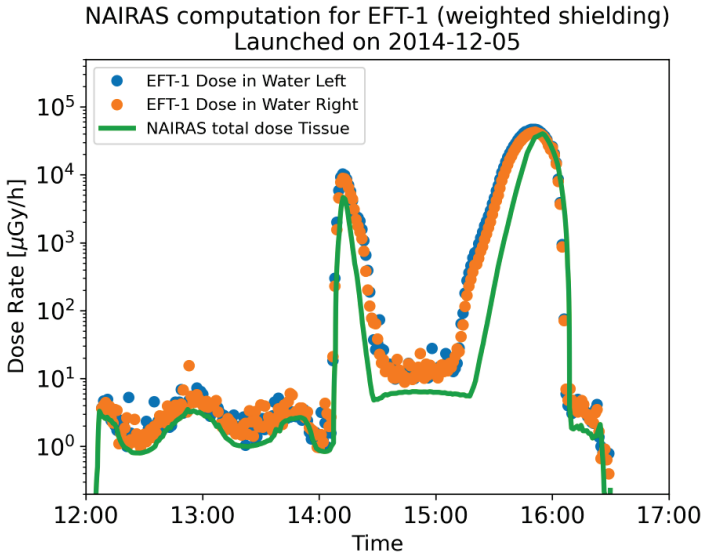

Figure 32. NAIRAS version 3 dose calculations and comparisons to BIRD (Left and Right detectors) measurements at NASA EFT-1 trajectory points on December 5, 2014. The median shielding thickness of the BIRD system is 25 g/cm^2 aluminum-equivalent.

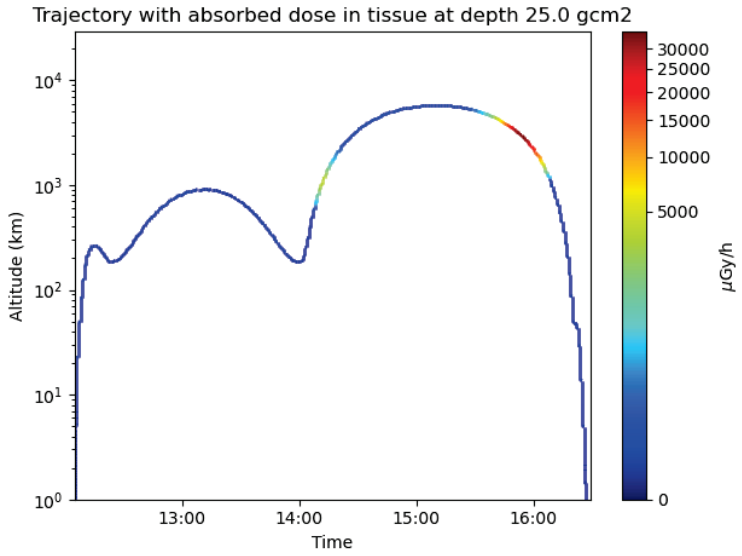

Figure 33. Altitude profile of the NASA EFT-1 flight trajectory. The color bar denotes the level of absorbed dose rate in tissue (μGy/h) calculated by NAIRAS during the flight.

The accumulated differential LET fluence spectrum measured by BIRD for the EFT-1 flight was reported by Bahadori et al. (2015). The NAIRAS differential LET fluence computed for EFT-1 is compared to the BIRD measurements in Figure 34. From the NAIRAS calculations, the differential LET fluence for the flight is dominated by the TRP-p contribution, as expected. The NAIRAS calculations differ most from the BIRD measurements at low LET (~ 1 keV/μm) and at high LET (> 100 keV/μm). In the middle LET region, the agreement is good.

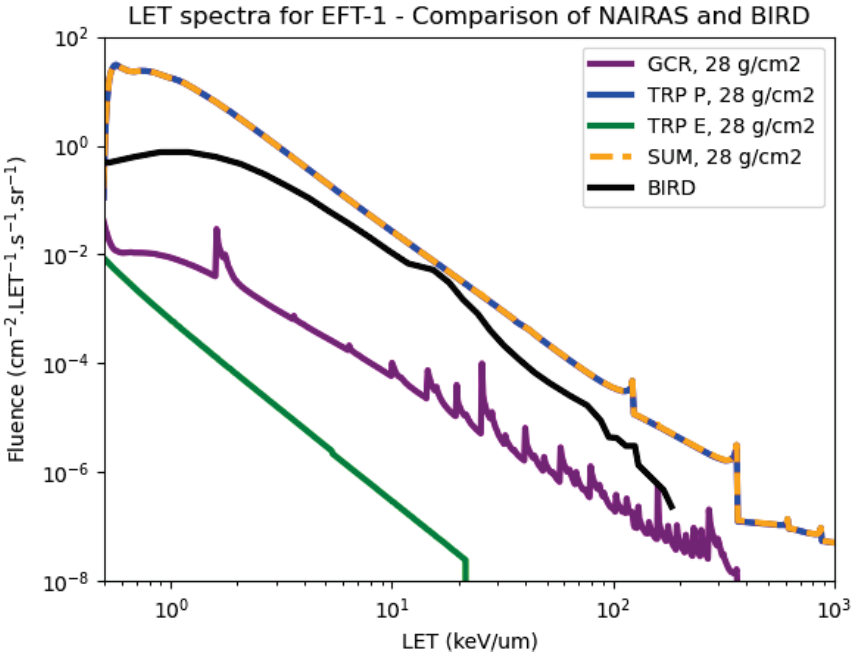

Figure 34. Accumulated differential LET fluence for the NASA EFT-1 flight. The black line denotes the BIRD measurement and the colored lines show results of NAIRAS version 3 calculations, with separate color lines for each contribution (GCR, TRP-p, and TRP-e) and the sum of the contributions.

9.3 Cislunar Orbit

The Artemis 1 mission launched on November 16, 2022, was the first spaceflight of NASA's Artemis Program. Artemis 1 was a 25-day, uncrewed Moon-orbiting mission, which returned to Earth on December 11, 2022. Using the TLE database, NAIRAS version 3 predicted the space radiation environment for the Artemis 1 mission in near real-time. The MPCV was equipped with the HERA, which is a distributed dosimeter system based on the coupling of a solid-state silicon detector with a Timepix chip (Kroupa et al., 2015). Future work will involve detailed comparisons between NAIRAS version 3 results and HERA measurements along the Artemis 1 flight trajectory. The results shown in Figure 35 are graphical products of the near real-time NAIRAS version 3 dosimetric predictions during the Artemis 1 flight computed at the median shielding thicknesses of the HERA dosimeters on the MPCV (Mertens et al., 2018), focusing on the launch to free-space phase of the flight trajectory.

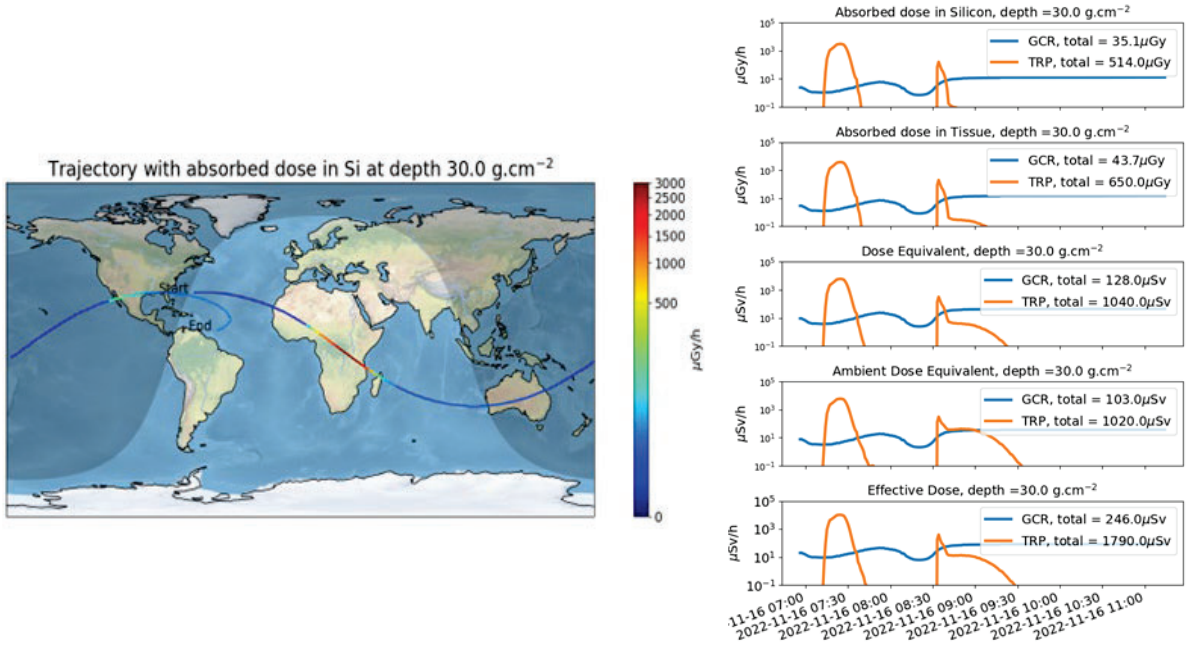

Figure 35. NAIRAS version 3 dosimetric predictions (dose rate as a function of time) during the NASA Artemis 1 flight mission on November 16, 2022. The results focus on the launch to free-space phase of the flight trajectory. The dosimetric quantities are shown for 50 g/cm² aluminum shielding.

10.0 Conclusions

The NAIRAS version 3 RoR capability allows end-users to run the model for customized scenarios and to perform scientific and engineering analysis of the atmospheric and space radiation environments. The global dosimetric run option provides context and situational awareness of the atmospheric ionizing radiation environment. The flight trajectory run option allows detailed human radiation flight exposure characterization, detailed comparisons to onboard dosimeters, and the assessment of SEE in aircraft and spaceflight electronic systems. The NAIRAS RoR service is now available to the space weather science and engineering community (Mertens et al., 2023a).

NAIRAS version 3 developments also included important model extensions and improvements. The domain of the model was extended from the atmosphere to free-space. This included

integrating TRP-p and TRP-e models into the NAIRAS modeling framework. The multi-directional transport procedure implemented for atmospheric ionizing radiation modeling significantly improved the accuracy of the dosimetric quantities at altitudes above 15 km. Analysis of the dosimetric measurements taken during the RaD-X campaign and measurements from the 1000+ ARMAS aircraft flights over the last decade show that the NAIRAS version 3 predictions agree with measurement to within 30% from 0 to 40 km. Publications of these results are in preparation. The robustness and fidelity of the SEP proton spectral fitting algorithm has been significantly improved by fitting to the GOES integral proton flux measurements. A SEP heavy-ion model was added to provide LET spectra for SEE assessment during SEP events. The geomagnetic vertical cutoff rigidity model was extended to include the option of two magnetospheric magnetic field models. This update facilitates intercomparisons between different cutoff and radiation models and provides a modeling framework for developing a cutoff rigidity forecast model. The improvements in the computational efficiency of the SEP proton spectral fitting algorithm and the vertical cutoff model enables NAIRAS version 3 predictions to be performed at 5-minute time intervals with reasonable and practical turnaround times.

The outcome of this study also led to the following topics that may be considered for future work:

1. Develop a hybrid version of the BON2020 GCR model, which can be used in real-time and RoR applications, and integrate it into NAIRAS to improve the specification of GCR primary proton flux.
2. Extend the analysis using the SEP spectral fitting algorithm to a large sample size event to empirically infer characteristics of SEP origin, acceleration, and transport.
3. Update the input DRNM and F10.7 data monthly and rescale the remaining forecast period to reduce the solar modulation extrapolation error to the TRP-p model.
4. Conduct additional validation studies at LEO and higher altitudes for different time periods to assess and improve the TRP-e model solar modulation correction accuracy.
5. Investigate the impact of range straggling in the electron transport code on geospace environment dose measurements.
6. Investigate improving the short-time scale variability in the outer belt TRP-e model.

Especially, the next phase of NAIRAS model development could focus on providing a real-time capability to support ISS operations for astronaut EVA, especially during SEP events. Future efforts could also be directed at extensive validation studies, with the aim of improving the various model components of NAIRAS. The preliminary validation results shown in this paper for LEO and MEO are encouraging. Different approaches to improving the trapped proton and electron environments have been identified. Validation studies and analysis in future work could also include comparing NAIRAS to the HERA dose measurements onboard the Artemis 1 flight.

11.0 Findings, Observations, and NESC Recommendations

11.1 Findings

F-1. The current NAIRAS GCR model (H-BON2010) is based on limited primary proton flux data and solar cycle variation from recent, high-quality space-based instrument

observations (e.g., PAMELA, AMS-02). Integrating the new BON2020 GCR model into NAIRAS would overcome this deficiency. (Section 8.1.1)

F-2. The new SEP heavy-ion model showed that heavy-ions make significant contributions to human radiation exposure in the geospace and free-space environments during SEP events, and quantified the significant enhancement of the geospace and free-space LET spectrum during SEP events, which is important for SEE assessment. (Section 8.1.2.2)

F-3. Modeling TRP-e is important for predicting astronaut radiation exposure during EVA in LEO, and validating the NAIRAS model against the most widely accessible spacebased dosimeter measurements. (Sections 8.1.4 and 9.1)

F-4. Extensive testing showed that the new SEP spectral fitting algorithm, which fits to GOES integral flux channels, is robust against numerical instability and free from erroneous, non-physical fits while simultaneously consistent with GOES differential flux measurement. (Section 8.1.2.1)

F-5. Analysis of the new SEP spectral fitting algorithm of a limited sample of SEP events at 1 AU reveal new characteristics. For example, different spectral shapes tend to dominate the event rise, peak, and decay phases. And DP spectrum tends to dominate strong to moderate GLEs, weak GLEs are a mixture of spectral shapes. (Sections 8.1.2.1 and 9.1)

F-6. The maximum monthly error in the TRP-p model solar cycle modulation correction is around 20% for the period between 2021 and 2022. (Section 8.1.3)

F-7. The 0.1 scale factor applied to the TRP-e model based on LEO dosimeter measurements may indicate that the solar modulation correction and transport code range straggling needs to be improved. (Section 8.1.4)

F-8. The steep decrease in the outer belt TRP-e flux occurs at energies greater than about 5 to 6 MeV. (Section 8.1.4)

F-9. The NAIRAS multi-directional transport procedure significantly improved the dosimetric quantities predictions above commercial aviation altitudes. (Section 8.3)

F-10. The current TRP-e model captures the high variability of the outer belt TRP-e flux , hence integrating the TRP-e model into NAIRAS improved the overall agreement between model predictions and LEO dosimeter measurements. (Section 9.1) .

F-11. Analysis of dosimetric measurements taken during the NASA RaD-X campaign and measurement from 1000+ ARMAS aircraft flights over the last decade show that NAIRAS version 3 predictions agree with the 0 to 40 km measurements to within 30%. (Section 8.3)

F-12. Measurements taken from the NASA RaD-X balloon flight showed that transport along the vertical direction in the atmospheric is insufficient for predicting dosimetric quantities for altitudes above commercial aircraft. (Section 8.3)

11.2 Observations

O-1. The heavy-ion sensor on GOES-R SEISS is an important measurement asset for improving the NAIRAS SEP heavy-ion model and refining its uncertainty assessment. (Section 8.1.2.2)

O-2. The inner belt TRP-e flux is orders of magnitude greater than the TRP-p flux for energies less than about 1 MeV and decreases drastically below the TRP-p flux for energies greater than about 3 MeV. (Section 8.1.4)

12.0 No recommendations have been identified. Alternate Technical Opinion(s)

No alternate technical opinions were identified during the course of this assessment by the NESC assessment team or the NRB.

13.0 Other Deliverables

In addition to the real-time and RoR versions of the NAIRAS software deployed at the CCMC, the team generated multiple publications, technical reports, and workshop and conference presentations based on the assessment work.

Mertens, C.J., G.P. Gronoff, Y. Zheng, J. Buhler, E. Willis, I. Jun, and J. Minow, NAIRAS Model Characterization of the LEO Environment for the Assessment of SEE Radiation Risks, Single Event Effects (SEE) Symposium and Military and Aerospace Programmable Logic Devices (/MAPLD) Workshop, virtual, 31 August – 2 September 2021.

Zheng, Y., C.J. Mertens, G.P. Gronoff, M. Petrenko, D.B Phoenix, J. Buhler, I. Jun, J. Minow, E. Willis, and M.M. Kuznetsova, Realtime and Tailored NAIRAS Products for Assessment of Aviation Radiation Risks and SEE Radiation Risks for LEO Space Assets, 17th European Space Weather Week, Glasgow, UK, 25 – 29 October 2021.

Mertens, C., G. Gronoff, Y. Zheng, J. Buhler, E. Willis, I. Jun, and J. Minow, NAIRAS Model Extension to the LEO Environment and New Products for Characterization of Single Event Effects, Applied Space Environments Conference 2021, virtual, 1 – 5 November 2021.

Minow, J.I., NESC Space Environments Activities, 12th NASA Space Exploration & Space Weather Workshop, virtual, 3 December 2021. (invited)

Gronoff, G.P., C.J. Mertens, D.B. Phoenix, Y. Zheng, J. Buhler, E. Willis, I. Jun, and J. Minow, NAIRAS Model Transition to the CCMC: Real-Time Dosimetric Output and Low-Earth Orbit Applications, 19th Conference on Space Weather, Houston, TX, 23 – 27 January 2022.

Mertens, C., NAIRAS Version 3.0: Atmospheric/Geospace Ionizing Radiation Environment Model, Community Coordinated Modeling Center 2022 Workshop, College Park, MD, 6-10 June 2022.

Mertens, C.J., G.P. Gronoff, Y. Zheng, J. Buhler, E. Willis, M. Petrenko, I. Jun, and J. Minow, NAIRAS Model Predictions of the Ionizing Radiation Environment from the Surface to Low-Earth Orbit, COSPAR 2022, 44TH Scientific Assembly, Athens, Greece, 16 – 24 July 2022.

Gronoff, G.P., C.J. Mertens, D.B. Phoenix, Y. Zheng, J. Buhler, E. Willis, I. Jun, and J. Minow, NAIRAS Model Transition to the CCMC: Real-Time Dosimetric Output and Low—Earth Orbit Applications, COSPAR 2022, 44TH Scientific Assembly, Athens, Greece, 16 – 24 July 2022.

Minow, J.I., NASA Use of Charged Particle Environments and Effects Engineering Tools, Space Environmental Effects and Science Applications Workshop, Johns Hopkins University, Applied Physics Laboratory, Laurel, MD, 12 – 16 September 2022. (invited)

Minow, J.I., NESC Space Environments Activities, Space Environmental Effects and Science Applications Workshop, Johns Hopkins University, Applied Physics Laboratory, Laurel, MD, 12 – 16 September 2022. (invited)

Mertens, C.J., G. Gronoff, Y. Zheng, J. Buhler, E.M. Willis, M. Petrenko, D. Phoenix, I. Jun, and J.I. Minow, NAIRAS Model Updates and Improvements to the Prediction of the Ionizing Radiation Environment from the Earth's Surface to Geospace, Abstract SM35C-1769, AGU Fall Meeting 2022, Chicago, IL, 12-16 December 2022.

Mertens, C.J., G. Gronoff, D. Phoenix, S.N. Paul, P.M. Mehta, Y. Zheng, and M. Nunez, NAIRAS Model Nowcasting and Forecasting of the Aviation Radiation Environment, 20th Conference on Space Weather, American Meteorological Society, 103rd Annual Meeting, Denver, CO, 8 – 12 January 2023.

Mertens, C.J., G. Gronoff, Y. Zheng, J. Buhler, E.M. Willis, M. Petrenko, D. Phoenix, I. Jun, and J. Minow, NAIRAS Model Updates and Improvements to the Prediction of Ionizing Radiation from Earth's Surface to Cislunar Environment, NOAA Space Weather Workshop, Boulder, CO, 17 – 21 April 2023.

Mertens, C. J., G.P. Gronoff, Y. Zheng, M. Petrenko, J. Buhler, D. Phoenix, E. Willis, I. Jun, and J. Minow. (2023). NAIRAS model run-on-request service at CCMC. *Space Weather*, 21, e2023SW003473. https://doi.org/10.1029/2023SW003473

Mertens, C.J., G. Gronoff, Y. Zheng, J. Buhler, E.M. Willis, M. Petrenko, D. Phoenix, I. Jun, and J.I. Minow, NAIRAS Atmospheric and Space Radiation Environment Model, IEEE Nuclear and Space Radiation Effects Conference, Kansas City, MO, 24 – 28 July 2023.

Mertens, C.J., G.P. Gronoff, D. Phoenix, Y. Zheng, M. Petrenko, J. Buhler, I. Jun, J. Minow, and E. Willis, NAIRAS Ionizing Radiation Model: Extension from Atmosphere to Space, NASA/TP-20230006306, May 2023.

Mertens, C.J., G.P. Gronoff, Y. Zheng, J. Buhler, E. Willis, M. Petrenko, D. Phoenix, I. Jun, and J. Minow, NAIRAS Atmospheric and Space Radiation Environment Model, *IEEE Transactions on Nuclear Science*, vol. 71, no. 4, pp. 618-625, April 2024, doi: 10.1109/TNS.2023.3330675.

Phoenix, D. B., Mertens, C. J., Gronoff, G. P., & Tobiska, K. (2024). Characterization of radiation exposure at aviation flight altitudes using the Nowcast of Aerospace Ionizing Radiation System (NAIRAS). *Space Weather*, 22, e2024SW003869.

Mertens, C.J., G.P. Gronoff, Y. Zheng, M. Petrenko, D. Phoenix, J. Buhler, E. Willis, I. Jun, and J. Minow, NAIRAS Atmospheric and Space Radiation Environment Model, Applied Space Environments Conference 2023, 9 – 13 October 2023, Huntsville, AL.

Mertens, C.J., G. Gronoff, Y. Zheng, J. Buhler, E.M. Willis, M. Petrenko, D. Phoenix, I. Jun, and J. Minow, NAIRAS Ionizing Radiation Environment Model, Space Environment Applications Systems and Operations for National Security (SEASONS), The Johns Hopkins University, Applied Physics Laboratory, Laurel, MD, 7 – 9 November 2023.

Gronoff, G., C.J. Mertens, D. Phoenix, K. Tobiska, Y. Zheng, I. Jun, and J. Minow, Comparison of the Nowcast of Aerospace Ionizing Radiation System (NAIRAS) with ISS Measurements, Abstract SH21E-2931, American Geophysical Union Fall Meeting 2023, 11- 15 December 2023, San Francisco, CA.

Mertens, C.J., G.P. Gronoff, D. Phoenix, Y. Zheng, I. Jun, J. Minow, and M. Nunez, Advances in NAIRAS Atmospheric and Space Radiation Nowcast and Forecast, American Meteorological Society 104st Annual Meeting, 21st Conference on Space Weather, 28 January – 1 February 2024, Baltimore, MD.

Gronoff, G., C.J. Mertens, D. Phoenix, K. Tobiska, Y. Zheng, I. Jun, and J. Minow, The Effect of an SEP Event on Astronauts Doing a Spacewalk as Computed by the Nowcast of Aerospace Ionizing Radiation System (NAIRAS), American Meteorological Society 104st

Annual Meeting, 21st Conference on Space Weather, 28 January – 1 February 2024, Baltimore, MD.
Mertens, C., Nowcast of Aerospace Ionizing RAdiation System (NAIRAS) Model, NOAA Space Weather Workshop, 15 – 19 April 2024, Boulder, CO. (invited)
Minow, J., NESC Space Environments Technical Discipline Team Activities, 13th NASA Space Exploration & Space Weather Workshop, 29 – 30 April 2024, GSFC, Greenbelt, MD.
Mertens, C. J., Gronoff, G. P., Phoenix, D., Zheng, Y., Petrenko, M., Buhler, J., et al. (2023). NAIRAS ionizing radiation model: Extension from atmosphere to space (NASA/TP- 2023-0006306). Hampton, VA: NASA Langley Research Center. https://ntrs.nasa.gov/citations/20230006306
Mertens, C. J., Gronoff, G. P., Zheng, Y., Buhler, J., Willis, E., Petrenko, M., et al. (2023). NAIRAS atmospheric and space radiation environment model. *IEEE Transactions on Nuclear Science*,71(4), 618-625. doi: 10.1109/TNS.2023.3330675
Phoenix, D. B., Mertens, C. J., Gronoff, G. P, and Tobiska, K. W. (2024). Characterization of radiation exposure at aviation flight altitudes using the Nowcast of Aerospace Ionizing Radiation System (NAIRAS), *Space Weather*, 22, e2024SW003869. https://doi.org/10.1029/2024SW003869

14.0 Recommendations for the NASA Lessons Learned Database

No recommendations for NASA lessons learned were identified as a result of this assessment.

15.0 Recommendations for NASA Standards, Specifications, Handbooks, and Procedures

No recommendations for NASA standards, specifications, or procedures were identified as a result of this assessment.

16.0 Definition of Terms

Finding	A relevant factual conclusion and/or issue that is within the assessment scope and that the team has rigorously based on data from their independent analyses, tests, inspections, and/or reviews of technical documentation.
Lesson Learned	Knowledge, understanding, or conclusive insight gained by experience that may benefit other current or future NASA programs and projects. The experience may be positive, such as a successful test or mission, or negative, as in a mishap or failure.
Observation	A noteworthy fact, issue, and/or risk, which is not directly within the assessment scope, but could generate a separate issue or concern if not addressed. Alternatively, an observation can be a positive acknowledgement of a Center/Program/Project/Organization's operational structure, tools, and/or support.
Recommendation	A proposed measurable stakeholder action directly supported by specific Finding(s) and/or Observation(s) that will correct or mitigate an identified issue or risk.

Root Cause	One or multiple causes (including adverse or unplanned events, conditions, or organizational factors) that contributed to or created the proximate cause(s) and subsequent undesired outcome and, if eliminated or modified, should have prevented the undesired outcome.

17.0 Acronyms and Nomenclature List

3D	Three-Dimensional
ACE	Advanced Composition Explorer
AE8	NASA standard trapped electron model
AE8MAX	AE8 trapped electron model, solar maximum version
AE8MIN	AE8 trapped electron model, solar minimum version
AGU	American Geophysical Union
AMS	Alpha Magnetic Spectrometer
AP8	NASA standard trapped proton model
AP8MAX	AP8 trapped proton model, solar maximum version
AP8MIN	AP8 trapped proton model, solar minimum version
ARMAS	Automated Radiation Measurements for Aerospace Safety
AU	Astronomical Units
BIRD	Battery-Operated Independent Radiation Detector
BON	Badhwar-O'Neill (galactic cosmic ray model)
CCMC	Community Coordinated Modeling Center
CCP	Commercial Crew Program
CISM	Center for Integrated Space Weather Modeling (at Dartmough College)
CME	Coronal Mass Ejection
CMG	Control Moment Gyroscope
CRAND	Cosmic Ray Albedo Neutron Decay
DP	Double Power-Law
DRNM	Deep-River Neutron Monitor
DSCOVR	Deep Space Climate Observatory
Dst	Storm-time geomagnetic disturbance index
EFT-1	Exploration Flight Test 1
EHIS	Energetic Heavy Ion Sensor
ER	Ellison-Ramaty
ESA	European Space Agency
EVA	Extravehicular Activity
F10.7	10.7 cm radio flux index
FIP	First Ionizing Potential
FOV	Field of View
GCR	Galactic Cosmic Ray
GEOFFB	Trapped proton (TRP-p) and electron (TRP-e) models
GLE	Ground-Level Enhancement
GOES	Geostationary Operational Environmental Satellite
GSFC	Goddard Space Flight Center
HEAO	High Energy Astrophysical Observatory
HERA	Hybrid Electronic Radiation Assessor
HRO	High Resolution OMNI
HZETRN	High Charge (Z) and Energy Transport
IGRF	International Geomagnetic Reference Field

IMF	Interplanetary Magnetic Field
ISEE-3	International Sun-Earth Explorer-3
ISS	International Space Station
iSWA	Integrated Space Weather Analysis System
JEM	Japanese Experiment Module
JPL	Jet Propulsion Laboratory
JSON	Javascript Object Notation
Kp	Midlatitude geomagnetic disturbance index
KSC	Kennedy Space Center
LaRC	Langley Research Center
LEO	Low Earth Orbit
LET	Linear Energy Transfer
MEO	Medium Earth Orbit
MPCV	Multipurpose Crew Vehicle
MSFC	Marshall Space Flight Center
NAIRAS	Nowcat of Aerospace Ionizing Radiation System
NCEI	National Centers for Environmental Information
NESC	NASA Engineering and Safety Center
NM	Neutron Monitor
NMDB	Neutron Monitor Database
NOAA	National Oceanic and Atmospheric Administration
NRB	Nesc Review Board
PAMELA	Payload for Antimatter Exploration and Light-Nuclei Astrophysics
RaD-X	Radiation Dosimetry Experiment
RoR	Run-on-Request
R_{ve}	Vertical Cutoff
SAA	South Atlantic Anomaly
SEE	Single Event Effect
SEISS	Series Space Environment In-Situ Suite
SEM	Space Environment Monitor
SEP	Solar Energetic Particle
SIS	Solar Isotope Spectrometer
SMP	Solar Modulation Potential
SSN	Sunspot Number
STS	Space Transportation System
Sv	Sievert
SWEPAM	Solar Wind Electron, Proton, And Alpha Monitor
SWICS	Solar Wind Ion Composition Spectrometer
SWPC	Space Weather Prediction Center
SYM-H	Longitudinally symmetric horizontal component magnetic disturbance index
T89	Tsyganenko semi-physics based geomagnetic field model, 1989
TEPC	Tissue-Equivalent Proportional Counter
TID	Total Ionizing Dose
TLE	Two-Line Element
TRP	Trapped
TRP-e	Trapped Electron
TRP-p	Trapped Proton
TS05	Tsyganenko semi-physics based geomagnetic field model, 2005
UT	Universal Time

WB	Weibull
WDC	World Data Center
WSO	Wilcox Solar Observatory

18.0 References

Adriani, O., Barbarino, G. C., Bazilevskaya, G. A., Bellotti, R. Boizio, M., Bogomolov, E. A., et al. (2013). Time dependence of the proton flux measured by PAMELA during the 2006 July – 2006 December Solar Minimum. *The Astrophysical Journal*, 765(91), doi:10.1088/0004-637X/765/2/91

Adriani, O., Barbarino, G. C., Bazilevskaya, G. A., Bellotti, R. Boizio, M., Bogomolov, E. A., et al. (2016). Measurements of cosmic-ray hydrogen and helium isotopes with the PAMELA experiment. *The Astrophysical Journal*, 818(68), doi:10.3847/0004-637X/818/1/68

Badavi, F. F., Nealy, J. E., & Wilson, J. W. (2011). The low earth orbit validation of a dynamic and anisotropic trapped radiation model through ISS measurements. *Advances in Space Research*, 48, 1441-1458.

Bahadori, A. A., Semones, E. J., Gaza, R., Kroupa, M., Rios, R. R., Stoffle, N. N., et al. (2015). Battery-operated Independent Radiation Detector Data Report from Exploration Flight Test 1 (NASA/TP-2015-218575). Houston, TX: NASA Johnson Space Center.

Binns, W. R., Fickle, R. K., Garrard, T. L., Israel, M. H., Klarmann, J., Stone, E. C., & Waddington, C. J. (1982). The abundance of the actinides in the cosmic radiation as measured on HEAO 3. *The Astrophysical Journal*, 261, L117-L120.

Brandt, S. (1999). Data analysis, statistical and computational methods for scientists and engineers. New York, New York: Springer-Verlag.

Cucinotta, F. A., Kim, M.-H. Y., Willingham, V., & George, K. A. (2008). Physical and biological organ dosimetry analysis for International Space Station astronauts. *Radiation Research*, 170, 127-138, doi:10.1667/RR1330.1

Dachev, T. P., Tomov, B. T., Matviichuk, Yu. N., Dimitrov, PI. G., & Bankov, N. G. (2016). High dose rates obtained outside ISS in June 2015 during SEP event. *Life Science in Space Research*, 8, 84-92. http://dx.doi.org/10.1016/j.lssr.2016.03.004

Daly, E. J., & Evans, H. D. R. (1996). Problems in radiation environment models at low altitudes. *Radiation Measurements*, 26(3), 263-368.

Ellison, D. C., & Ramaty, R. (1985). Shock acceleration of electrons and ions in solar flares. *The Astrophysical Journal*, 298, 400-408.

European Cooperation for Space Standardization (2010). Space engineering: Calculation of radiation and its effects and margin policy handbook (ECSS Working Group Report ECSS-E-HB-10-12A). The Netherlands: ESA Requirements and Standards Division.

Fowler, P. H., Walker, R. N. F., Masheder, M. R. W., Moses, R. T., Worley, A., & Gay, A. M. (1987). Ariel 6 measurements of the fluxes of ultraheavy cosmic rays. *The Astrophysical Journal*, 314, 739-746.

Gaza, R., Kroupa, M., Rios, R., Stoffle, N., Benton, E. R., & Semones, E. J. (2017). Comparison of novel active semiconductor pixel detector with passive radiation detectors during the NASA Orion Exploration Flight Test 1 (EFT-1). *Radiation Measurements*, 106, 290-297. http://dx.doi.org/10.1016/j.radmeas.2017.03.041

Gersey, B., W.K. Tobiska, W. Atwell, D. Bouwer, L. Didkovsky, K. Judge, S. Wieman, and R. Wilkins (2020), Beamline and flight comparisons of the ARMAS flight module with the

tissue equivalent proportional counter for improving atmospheric radiation monitoring accuracy. *Space Weather,* 18, e2020SW002599. https://doi.org/ 10.1029/2020SW002599
Grevesse, N. (2019). The solar chemical composition: Past and present. *Bulletin de la Societe Royale de Sciences des Liege*, 88, 5-14. https://doi.org/10.25518/0037-9565.9235
Heynderickx, D., Lemaire, J., & Daly, E. J. (1996). Historical review of the different procedures used to compute the L-parameter. *Radiation Measurements*, 26(3), 325-331.
Hu, S., Kim, M.-H. Y., McClellan, G. E., & Cucinotta, F. A. (2009). Modeling the acute health effects of astronauts from exposure to large solar particle events. *Health Physics*, 96(4), 1-12.
Hildebrand, F. B. (1974). *Introduction to numerical analysis*. New York: Dover Publications, Inc.
King, J. H., & Papatashvilli, N. (2023). OMNI Combined, Definitive, 5-minute IMF and Plasma, and Energetic Proton Fluxes., Time-Shifted to the Nose of the Earth's Bow Shock, Plus Magnetic Indices. OMNI_HRO_5MIN [Dataset]. AdnetSystems, NASA Goddard Space Flight Center and CDAWeb (select OMNI and select OMNI_HRO_5MIN). SPDF - Coordinated Data Analysis Web (CDAWeb) (nasa.gov)
Koontz, S., Suggs, R., Alred, J., Worthy, E., Boeder, P., Steagall, C., et al. (2018). The International Space Station space radiation environment: Avionics systems performance in low-Earth orbit single event effects environments (SEE). Paper presented at the 48th International Conference on Environmental Systems (ICES-2018-69), Albuquerque, New Mexico.
Kress, B. T., Hudson, M. K., Perry, K. L., & Slocum, P. L. (2004). Dynamic modeling of geomagnetic cutoff for the 23-24 November 2001 solar energetic particle event. *Geophysical Research Letters*, 31, L04808, doi:10.1029/2003GL018599
Kress, B. T., Mertens, C. J., & Wiltberger, M. (2010). Solar energetic particle cutoff variations during the 28-31 October 2003 geomagnetic storm. *Space Weather*, 8, S05001, doi:10.1029/2009SW000488
Kress, B. T., Rodriquez, J. V., & Onsager, T. G. (2019). The GOES-R space environment in situ suite (SEISS): Measurement of energetic particles in geospace. In S. J. Goodman, T. J. Schmit, J. Daniels, and R. J. Redmon (Eds), *The GOES-R Series: A New Generation of Geostationary Environmental Satellite* (ch. 20, pp. 243-250). Cambridge, MA: Elsevier.
Kress, B. T., Rodriguez, J. V., Boudouridis, A., Onsager, T. G., Dichter, B. K., Galica, G. E., et al. (2021). Observations from NOAA's newest solar proton sensor. *Space Weather*, 19, e2021SW002750. https://doi.org/10.1029/2021SW002750
Kroupa, M., Bahadori, A., Campbell-Ricketts, T., Empl, A., Hoang, S. M., Idrraga-Munoz, J, et al. (2015). A semiconductor radiation imaging detector for space radiation dosimetry. *Life Sciences in Space Research*, 6, 69-78.
Meier, M. M., Copeland, K., Matthia, D., Mertens, C. J., & Schennetten, K. (2018). First steps toward the verification of models for the assessment of the radiation exposure at aviation altitudes during quiet space weather conditions. *Space Weather*, 16, 1269-1276. https://doi.org/10.1029/2018SW001984
Mertens, C. J., Wilson, J. W., Walker, S. A., & Tweed, J. (2007). Coupling of multiple Coulomb scatter with energy loss and straggling in HZETRN. *Advances in Space Research*, 40, 1357-1367.
Mertens, C. J., Kress, B. T., Wiltberger, M., Blattnig, S. R., Slaba, T. S., Solomon, S. C., & Engel, M. (2010a). Geomagnetic influence on aircraft radiation exposure during a solar

energetic particle event in October 2003. *Space Weather,* 8, S03006, doi:10.1029/2009SW000487
Mertens, C. J., Moyers, M. F., Walker, S. A., & Tweed, J. (2010b). Proton lateral broadening distribution comparisons between GRNTRN, MCNPX, and laboratory beam measurements. *Advances in Space Research*, 45, 884-891.
Mertens, C.J., Kress, B. T., Wiltberger, M., Tobiska, W. K., Grajewski, B., & Xu, X. (2012). Atmospheric ionizing radiation from galactic and solar cosmic rays. In M. Nenoi (Ed.), *Current topics in ionizing radiation research* (pp. 683-738). Rijeka, Croatia: InTech Publisher.
Mertens, C. J., Meier, M. M., Brown, S., Norman, R. B., & Xu, X. (2013). NAIRAS aircraft radiation model development, dose climatology, and initial validation. *Space Weather*, 11, 603–635, doi:10.1002/swe.20100
Mertens, C. J. (2016a). Overview of the Radiation Dosimetry Experiment (RaD-X) flight mission. *Space Weather*, 14, doi:10.1002/2016SW001399
Mertens, C. J., Gronoff, G. P., Norman, R. B., Hayes, B. M., Lusby, T. C., Straume, T., et al. (2016b). Cosmic radiation measurements from the RaD-X flight campaign. *Space Weather*, 14, 874-898, doi:10.1002/2016SW001407
Mertens, C. J., Slaba, T. C., & Hu, S. (2018). Active dosimetric-based estimate of astronaut acute radiation risk for real-time solar energetic particle events. *Space Weather*, 16, 1291-1316. https://doi.org/10.1029/2018SW001971
Mertens, C. J., & Slaba, T. C. (2019). Characterization of solar energetic particle radiation dose to astronaut crew on deep-space exploration mission. *Space Weather*, 14. https://doi.org/10.1029/2019SW002363
Mertens, C. J., Gronoff, Phoenix, D., G. P., Zheng, Y., Petrenko, M., Buhler, J., et al. (2023a). NAIRAS ionizing radiation model: Extension from atmosphere to space (NASA/TP- 2023-0006306). Hampton, VA: NASA Langley Research Center. https://ntrs.nasa.gov/citations/20230006306
Mertens, C. J., Gronoff, G. P., Zheng, Y., Petrenko, M., Buhler, J., Phoenix, D., et al. (2023b). NAIRAS model run-on-request service at CCMC. *Space Weather*, 21, e2023SW003473. https://doi.org/10.1029/2023SW003473
Mertens, C. J., Gronoff, G. P., Zheng, Y., Buhler, J., Willis, E., Petrenko, M., et al. (2024). NAIRAS atmospheric and space radiation environment model. *IEEE Transactions on Nuclear Science*, 71(4), 618-625. doi: 0.1109/TNS.2023.3330675
Mewaldt, R. A. (1988). Elemental composition and energy spectra of galactic cosmic rays. In *Interplanetary Particle Environment* (JPL Publication 88, pp. 121-132). Pasadena, CA: Jet Propulsion Laboratory, California Institute of Technology.
Mewaldt, R. A., Cohen, C. M. S., Labrador, A. W., Leske, R. A., Mason, G. M., Desai, M. I., et al. (2005). Proton, helium, and electron spectra during the large solar particle events of October-November 2003. *Journal of Geophysical Research*, 110(A09S10), doi:10.1029/2005JA011038
Minow, J. I., Mertens, C. J., Parker, L. N., Allen, J. R., Fry, D. J., Semones, E. J., et al. (2020). Space weather architecture options to support human and robotic deep space exploration (NASA/TM-2020-5000837). Hampton, VA: NASA Langley Research Center.
Norman, R. B., Mertens, C. J., & Slaba, T. C. (2016). Evaluating galactic cosmic ray environment models using RaD-X flight data. *Space Weather*, 14, 764-775, doi:10.1002/2016SW001401

O'Neill, P. M., (2010). Badhwar-O'Neill 2010 galactic cosmic ray flux model – Revised. *IEEE Transactions on Nuclear Science*, 57(6), 3148-3153.
Press, W. H., Teukolsky, S. A., Vettering, W. T., & Falnnery, B. P. (1992). *Numerical recipes in Fortran: The art of scientific computing (2nd ed.)*. New York: Cambridge Press.
Reames, D. V. (1998). Solar energetic particles: Sampling coronal abundances, *Space Science Review*, 85, 327-340.
Rodriguez, J. V., Sandberg, I., Mewaldt, R. A., Daglis, I. A., & Jiggens, P. (2017). Validation of the effect of cross-calibrated GOES solar proton effective energies on derived integral fluxes by comparison with STEREO observations. *Space Weather*, 15, 290–309, doi:10.1002/2016SW001533.
Singleterry Jr., R. C., Shinn, J. L., Wilson, J. W., Maiden, D. L., Thibeault, S. A., Badavi, F. F., et al. (1999). Aircraft radiation shield experiments – preflight laboratory testing (NASA/TM-1999-209131). Hampton, VA: NASA Langley Research Center.
Slaba, T. C., Blattnig, S. R., Clowdsley, M. S., Walker, S. A., & Badavi, F. F. (2010). An improved neutron transport algorithm for HZETRN (NASA/TP-2010-216199). Hampton, VA: NASA Langley Research Center.
Slaba, T. C. (2013a). Faster heavy ion transport for HZETRN (NASA/TP-2013-217803). Hampton, VA. NASA Langley Research Center.
Slaba, T. C., Blattnig, S. R., Reddell, B., Bahadori, A., Norman, R. B., & Badavi, F. F. (2013b). Pion and electromagnetic contribution to dose: Comparisons of HZETRN to Monte Carlo and ISS data. *Advances in Space Research*, 52, 62-78.
Slaba, T. C., & Stoffle, N. N. (2017). Evaluation of HZETRN on the Martian Surface: Sensitivity tests and model results. *Life Science and Space Research*, 14, 29-35.
Slaba, T. C., & Whitman, K., (2020a). The Badhwar-O'Neill 2020 GCR model, *Space Weather*, 18, e2020SW002456. https://doi.org/10.1029/2020SW002456
Slaba, T. C., Wilson, J. W., Werneth, C. M., & Whitman, K., (2020b). Updated deterministic radiation transport for future deep space mission. *Life Sciences in Space Research*, 27, 6-18.
Smart, D. F., & Shea, M. A. (2005). A review of geomagnetic cutoff rigidities for earth-orbiting satellites. *Advances in Space Research*, 36, 2012-2020.
Stone, E. C., Cohen, C. M. S., Cook, W. R., Cummings, A. C., Gauld, B., Kecman, B., et al. (1998). The Solar Isotope Spectrometer on for the Advanced Composition Explorer, *Space Science Reviews*, 86, 357-408.
Stormer, C. (1965). *The polar aurora*. Oxford: Clarendon Press.
Tobiska, W. K., Bouwer, D., Smart, D., Shea, M., Bailey, J., Didkovsky, L., et al., (2016). Global real-time dose measurements using the Automated Radiation Measurements for Aerospace Safety (ARMAS) system. *Space Weather*, 14, 1053-1080, doi:10.1002/2016SW001419
Tobiska, W.K., L. Didkovsky, K. Judge, S. Wieman, D. Bouwer, J. Bailey, B. Atwell, M. Maskrey, C. Mertens, Y. Zheng, M. Shea, D. Smart, B. Gersey, R. Wilkins, D. Bell, L. Gardner, and R. Fuschino (2018), Analytical representations for characterizing the global aviation radiation environment based on model and measurement databases. *Space Weather,* 16, 1523–1538. https://doi.org/ 10.1029/2018SW001843.
Townsend, L. W., Zapp, E. N., & Hoff, J. L. (2003). Carrington flare of 1859 as a prototypical worst-case solar energetic particle event. *IEEE Transactions on Nuclear Science*, 50(6), 2307-2309.

Townsend, L. W., Stephens Jr., D. L., Hoff, J. L., Zapp, E. N., Moussa, H. M., Miller, T. M., et al. (2006). The Carrington event: Possible doses to crews in space from a comparable event. *Advances in Space Research*, 38, 226-231.

Townsend, L. W., Adams, J. H., Blattnig, S. R., Clowdsley, M. S., Fry, D. J., McLeod, C. D., et al. (2018). Solar particle event storm shelter requirements for mission beyond low Earth orbit. *Life Sciences in Space Research*, 17, 32-39. https://doi.org/10.1016/j.lssr.2018.02.002

Tsyganenko, N. A. (1989). Determination of magnetic current system parameters and development of experimental geomagnetic field models based on data from IMP and HEOS satellite. *Planetary and Space Science*, 37, 5-20.

Tsyganenko, N. A. & Sitnov, N. I. (2005). Modeling the dynamics of the inner magnetosphere during strong geomagnetic storms. *Journal of Geophysical Research*, 110, A03208, doi:10.1029/2004JA010798

Tylka, A. J., Cohen, C. M. S., Dietrich,W. F., Lee, M. A., Maclennan, C. G., Mewaldt, R. A., et al. (2005). Shock geometry, seed populations, and the origin of variable elemental composition at high energies in large gradual solar particle events. *The Astrophysical Journal*, 625, 474-495.

Tylka, A. J., & Lee, M. A. (2006). Spectral and compositional characteristics of gradual and impulsive solar energetic particle events, in solar eruptions and energetic particles. In N. Gopalswamy, R. Mewaldt, & Torsi, J. (Eds), *Solar Eruptions and Energetic Particles*, *Geophysical Monograph Series* (Vol.165, pp. 263-274). Washington, DC: American Geophysical Union.

U. S. Standard Atmosphere, 1976 (1976). NASA-TM-X-74335. Washington, DC: National Oceanic and Atmospheric Administration, National Aeronautics and Space Administration, and United States Airforce.

Van Allen, J. A. (1968). Particle description of the magnetosphere. In *Physics of the Magnetosphere* (Vol. 10, pp. 147-217). New York, NY: Springer-Verlag.

Vette, J. I. (1991). The NASA/National Space Science Data Center Trapped Radiation Environmental Model Program (1964–1991) (Tech. Rep. NSSDC/ WDC-A-R&S 91-29). Greenbelt, MD: NASA Goddard Space Flight Center. https://ntrs.nasa.gov/api/citations/19930001815/downloads/19930001815.pdf

Wilson, J. W., Townsend, L. W., Schimmerling, W., Khandelwal, G. S., Khan, F., Nealy, J. E., et al. (1991). Transport methods and interactions for space radiation (NASA RP-1257). Washington, DC: NASA.

Wilson, J. W., Badavi, F. F., Kim, M.-H. Y., Clowdsley, M. S., Heinbockel, J. H., Cucinotta, F. A., et al. (2002). Natural and induced environment in low earth orbit (NASA/TM-2002-211668). Washington, DC: NASA.

Wilson, J. W., Tripathi, R. K., Mertens, C. J., Blattnig, S. R., Clowdsley, M. S., Cucinotta, F. A., et al. (2005). Verification and validation of High charge and Energy (HZE) transport codes and future development (NASA/TP-2005-213784). Washington, DC: NASA.

Wu, H., Atwell, W., Cucinotta, F. A., & Wang, C.-H. (1996). Estimate of space radiation-Induced cancer risks for International Space Station orbits (NASA TM-104818). Linthicum Heights, MD: NASA Center for AeroSpace Information.

Xapsos, M. A., Barth, J. L., Stassionopoulos, E. G., Messenger, S. R., Walters, R. J., Summers, G. P., & Burke, E. A. (2000). Characterizing solar proton energy spectra for radiation effects applications. *IEEE Transactions on Nuclear Science*, 47(6), 2218-2223.

Xapsos, M. A., Stauffer, C., Jordan, T., Barth, J. L., & Mewaldt, R. A. (2007). Model for cumulative solar heavy ion energy and linear energy transfer. *IEEE Transactions on Nuclear Science*, 54(6), 1985-1989.

Zhang, S., & Jin, J. (1996). *Computation of special functions*. New York: John Wiley and Sons, Inc.

Appendix A: Model Input Data

The NAIRAS model input data fields are described in this appendix. All input data are obtained in real-time for the NAIRAS real-time run mode. The real-time data fields are saved locally and archived daily using SQLite database management. The daily updated model input database allows the NAIRAS RoR run mode to be utilized in near real time. In addition to daily updates of the real-time data streams, a separate input database is maintained which is updated monthly using definitive archived data provided by the instrument science teams. For the NAIRAS RoR run mode, the user can select either source of input data: 1) real-time (i.e., operational quality) or 2) definitive (i.e., science quality). The input data quality option allows the user to reproduce the NAIRAS real-time output products and evaluate the quality of the real-time data streams on NAIRAS model nowcasts and forecasts. The subsections below organize the input model data descriptions with respect to the corresponding NAIRAS model component.

A.1 GCR Model

The Neutron monitor (NM) data used by the NAIRAS H-BON10 GCR model are from the Izmiran, Oulu, Lomnicky, and Thule site locations. The pressure-corrected 1-minute NM count rates from these four sites are obtained in real-time from the NMDB (Neutron Monitor database)[1]. The NMDB provides instructions for automatic NM data retrieval[2]. Science quality NM data are obtained from Oulu. The other three NM locations no longer provide a data product different from what is available through the NMDB.

For time periods after 1976, the solar polar magnetic field polarity states are determined by field measurements taken by the Wilcox Solar Observatory (WSO)[3]. The WSO provides science quality data for the solar polar magnetic field measurements. WSO data are updated every few weeks. Since WSO is used only to determine field polarity, data persistence is assumed in the WSO data for real-time NAIRAS run mode or quasi real-time NAIRAS RoR run mode applications.

A.2 SEP Model

GOES 5-minute differential and integral proton flux and differential alpha flux data are used to infer the SEP proton and heavy-ion spectra. The real-time proton flux data from the current GOES SEISS are available from the NOAA SWPC in JavaScript Object Notation (JSON) format[4]. As of the date of this publication, NOAA SWPC has not provided GOES SEISS particle flux data that are corrected for GCR background and out-of-band contributions (Kress et al., 2021). Moreover, NOAA SWPC has not provided real-time differential alpha flux data. Currently, a daily aggregate of GOES SEISS alpha flux data are provided once a day from the Energetic Heavy Ion Sensor (EHIS) Level 1B data product[5]. If the GOES alpha flux data are not

[1] NMDB Data: nmdb.eu/nest/

[2] NMDB Data Retrieval: nmdb.eu/nest/help.php#howto

[3] WSO solar polar magnetic field measurements: http://wso.stanford.edu/Polar.html

[4] GOES SEISS Real-Time Data: https://services.swpc.noaa.gov/json/goes/

[5] GOES SEISS Daily Differential Alpha Flux Data: a) GOES-16 https://data.ngdc.noaa.gov/platforms/solar-space-observing-satellites/goes/goes16/l1b/seis-l1b-ehis/ and GOES-18 https://data.ngdc.noaa.gov/platforms/solar-space-observing-satellites/goes/goes18/l1b/seis-l1b-ehis/

available for a NAIRAS real-time run, the SEP heavy-ion model specifies the alpha spectrum by scaling the GOES-inferred proton spectrum by an empirically determined factor (0.056), based on analyzing SEP events observed in the GOES particle flux measurement data from 1997 to 2017.

GOES 5-minute proton and alpha flux data from the Space Environment Monitor (SEM) are available from January 1, 1976 through March 4, 2020. The NAIRAS SEP spectral fitting module uses the corrected GOES 5-minute particle flux data. The corrected flux data are based on a processing algorithm that removes GCR background and corrections for out-of-band contributions (Rodriquez et al., 2017). These data are obtained from the NOAA National Centers for Environmental Information (NCEI) website in the csv file format[6]. Since May 2010, the SEM system has included two identical particle flux detector systems, one with an east-facing field-of-view (FOV) and the other with a west-facing FOV. In the NAIRAS SEP spectral fitting algorithm, the particle flux data are selected from the detector system that has the largest flux, as this is the FOV that is best connected magnetically to interplanetary space and most representative of the free-space SEP particles.

The archived GOES SEISS data begins on November 1, 2020 and extends to the present. These data are obtained from the NOAA/NCEI website only in netcdf file format[7]. From March through November 2020 there are no NOAA/NCEI archived GOES SEISS data. The NAIRAS input database, however, has the GOES SEISS data during this gap period, which were obtained from the NAIRAS daily archival of the real-time model input data streams. From November 2020 onwards the GOES SEISS data are archived at NCEI in netcdf format. However, most of the integral flux data are absent in the NCEI archive data. Thus, the NAIRAS input database of GOES SEISS integral proton flux data is built from the real-time JSON files of GOES SEISS integral proton flux data from NOAA/SWPC. Furthermore, as discussed at the beginning of this section, the archived GOES SEISS differential alpha flux data in the NAIRAS input database is built from the daily aggregate of EHIS Level 1B alpha data.

A.3 Geomagnetic Cutoff Rigidity Model

The input data to the geomagnetic cutoff rigidity model are input data fields required for the magnetospheric magnetic field models: TS05 and T89. The inputs to the TS05 model are 5-minute solar-wind velocity, temperature, density, and the IMF components. The SYM-H index is also an input to TS05. Operational quality solar wind plasma parameters and IMF components are provided by NOAA/SWPC in JSON format from the NASA ACE[8] and NOAA DSCOVR[9] satellites. In real-time, NOAA SWPC decides which satellite source, ACE or DSCOVR, is the source of the solar wind plasma parameters and IMF components at each time step in the real-

[6] GOES SEM Data: https://www.ncei.noaa.gov/data/goes-space-environment-monitor/access/avg/

[7] GOES SEISS Archive Data: https://data.ngdc.noaa.gov/platforms/solar-space-observing-satellites/goes/goes16/l2/data/sgps-l2-avg5m/

[8] ACE Real-time Data: http://services.swpc.noaa.gov/json/ace/

[9] DSCOVR Real-Time Data: https://services.swpc.noaa.gov/json/dscovr/

time data stream[10]. The real-time input to the T89 model is the Kp-index. Both the SYM-H and Kp indices are obtained from the World Data Center (WDC) on Geomagnetism[11].

The science quality TS05 input data are obtained from the high-resolution OMNI (HRO) dataset which is accessible from NASA OMNIWeb[12]. The HRO 5-minute solar wind plasma and IMF data are averages of the 1-minute data from NASA ACE (1998 to present), Wind (1995 to present), IMP-8 (1973 to 2000), and Geotail (1995 to 2006), which have been time-shifted to Earth's bow nose[13]. The OMNIWeb SYM-H and Kp indices are also obtained from the WDC. Fortran codes are available to read the dynamical input data to the TS05 model downloaded from OMNIWeb and to further format them for input to the TS05 model[14]. The formatting code also fills in data gaps in the solar wind plasma and IMF data that are less than 3 hours. However, there are larger gaps in the solar wind plasma data during strong SEP events. These gaps are filled by interpolation from 12-minute average ACE Solar Wind Electron, Proton, and Alpha Monitor (SWEPAM) and Solar Wind Ion Composition Spectrometer (SWICS), which have been merged into a Level 3 data product[15]. This processing step is part of the regular procedure to update the NAIRAS model science quality input database. However, the large data gap filling technique using ACE SWEPAM and SWICS is not possible after 2021 as the ACE science team is no longer providing Level 2 and Level 3 data products after this date.

A.4 Radiation Belt Models

The input data fields to the trapped proton model are the Oulu NM count rates and the F10.7 index. The NM data were discussed in Section A.1. Daily average F10.7 index is provided by the Canadian Government[16]. The science quality F10.7 index data are obtained from the GFZ German Research Center for Geosciences[17].

The input data field to the trapped electron model is the F10.7 index. The real-time and science quality sources for this parameter are the same as those for the trapped proton model.

[10] NOAA SWPC Real-time Solar Wind and IMF: https://services.swpc.noaa.gov/json/rtsw/

[11] WDC Data: https://wdc.kugi.kyoto-u.ac.jp/wdc/Sec3.html

[12] NASA HRO Dataset: https://omniweb.gsfc.nasa.gov/form/omni_min.html

[13] NASA HRO Data Preparation: https://omniweb.gsfc.nasa.gov/html/HROdocum.html

[14] TS05 Input Data Build: https://geo.phys.spbu.ru/~tsyganenko/TS05_data_and_stuff/

[15] NASA ACE SWEPAM/SWICS Level 3 Data: https://izw1.caltech.edu/ACE/ASC/level2/sweswi_l3desc.html

[16] Canadian Government Daily-Average F10.7 Data: https://spaceweather.gc.ca/forecast-prevision/solar-solaire/solarflux/sx-5-en.php

[17] GFZ Kp Index: https://kp.gfz-potsdam.de/en/

Appendix B: SEP Spectral Fitting Algorithm

The objective of the SEP proton spectral fitting algorithm is to determine the free parameters of the analytical forms in equations (5) through (8) that optimally estimate the GOES proton flux measurements to within measurement uncertainty. The problem statement can be formally expressed as

$$\mathbf{y} = \mathbf{F}(\mathbf{x}) + \boldsymbol{\varepsilon}, \tag{31}$$

where $\mathbf{y}$ is the vector of GOES proton flux measurements, $\mathbf{F}(\mathbf{x})$ is the model of the measurements, or the so-called forward model, which depends on the parameter vector $\mathbf{x}$, and $\boldsymbol{\varepsilon}$ is the vector of measurement errors. Assuming Gaussian noise statistics for $\boldsymbol{\varepsilon}$, a maximum likelihood solution for the free parameters $\mathbf{x}$ can be found by solving a Bayesian statistical inverse problem (e.g., Mertens et al., 2018). This is equivalent to finding a solution $\mathbf{x}_s$ that minimizes the cost function $\Phi(\mathbf{x})$, such that

$$\nabla\Phi(\mathbf{x}_s) = 0, \tag{32}$$

with the cost function given by

$$\Phi(\mathbf{x}) = \left(\mathbf{y} - \mathbf{F}(\mathbf{x})\right)^T \tilde{\mathbf{S}}_\varepsilon^{-1} \left(\mathbf{y} - \mathbf{F}(\mathbf{x})\right), \tag{33}$$

and the measurement error covariance matrix denoted $\tilde{\mathbf{S}}_\varepsilon$. The forward model can be expanded in a Taylor series to first order about an initial guess for the model parameters $\mathbf{x_0}$, such that

$$\mathbf{F}(\mathbf{x}) = \mathbf{F}(\mathbf{x}_0) + \frac{\partial \mathbf{F}}{\partial \mathbf{x}}\left(\mathbf{x} - \mathbf{x}_0\right) + \cdots \tag{34}$$

$$\mathbf{F}(\mathbf{x}) \approx \mathbf{F}(\mathbf{x}_0) + \tilde{\mathbf{K}}(\mathbf{x} - \mathbf{x}_0), \tag{35}$$

where $\tilde{\mathbf{K}}$ is the Jacobian matrix, or sometimes referred to as the measurement weighting function (Mertens et al., 2018). For a linear problem, the solution for the free parameters $\mathbf{x}_s$ can be obtained in one solution step by solving equation (32) and equation (33) with the forward model given by equation (35). However, for forward models with a nonlinear dependence on the model parameters, a Newtonian iteration of the linear solution is typically employed until convergence is reached. For moderately nonlinear problems, a Marquardt-Levenberg approach improves the convergence of the Newtonian iteration method by introducing an optimally determined parameter λ into the solution equation (Press et al., 1992). Thus, the Marquardt-Levenberg solution of equation (32) and equation (33) can be expressed in the following form:

$$\mathbf{x}_i = \mathbf{x}_{i-1} + \left(\tilde{\mathbf{K}}_{i-1}^T \tilde{\mathbf{S}}_\varepsilon^{-1} \tilde{\mathbf{K}}_{i-1} + \lambda_{i-1} \tilde{\mathbf{I}}\right)^{-1} \left[\tilde{\mathbf{K}}_{i-1}^T \tilde{\mathbf{S}}_\varepsilon^{-1} \tilde{\mathbf{K}}_{i-1} \left(\mathbf{y} - \mathbf{F}(\mathbf{x}_{i-1})\right)\right], \tag{36}$$

where the subscript denotes the iteration step. The Marquardt-Levenberg algorithm determines the λ parameter at each iteration step to give a steepest descent increment when far from the solution and an inverse Hessian increment when near the solution (Press et al., 1992). The Marquardt-Levenberg algorithm used in the NAIRAS version 3 SEP spectral fitting code is an adaptation of the routines reported by Brandt (1999).

The application of the general expression in equation (36) to SEP proton spectral fitting to GOES differential proton flux measurements is described as follows. The measurement vector $\mathbf{y}$ is the GOES differential proton flux measurements. The number of GOES differential proton channels used in the SEP proton spectral fit is typically around seven with average channel energies varying between 25 MeV and 600 MeV, depending on the specific GOES series and its particle flux detector system. The forward model $\mathbf{F}(\mathbf{x})$ is the analytical SEP proton spectral forms in equations (5) through (8) evaluated at the geometric average energy of the GOES differential proton flux channels. The measurement error covariance matrix $\tilde{\mathbf{S}}_{\varepsilon}$ is prescribed by uncorrelated Poisson statistics. Computational efficiency and numerical accuracy and stability are maximized when the Jacobian matrix is computed analytically. Thus, the Jacobian matrices for the four analytical representations of the SEP proton spectral flux are given below.

For the single power-law representation of the SEP proton spectral flux in equation (5), let the parameter vector be defined as $\mathbf{x} = \left(C, \gamma\right)^T$. The Jacobian matrix elements for the fit to GOES differential proton flux are:

$$\begin{aligned} \tilde{\mathbf{K}}_{1,j} &= E_j^{-\gamma} \\ \tilde{\mathbf{K}}_{2,j} &= -CE_j^{-\gamma} \ln E_j . \end{aligned} \tag{37}$$

For the Ellison-Ramaty representation of the SEP proton spectral flux in equation (6), let the parameter vector be defined as $\mathbf{x} = \left(C, \gamma, E_0\right)^T$. The Jacobian matrix elements for the fit to GOES differential proton flux are:

$$\begin{aligned} \tilde{\mathbf{K}}_{1,j} &= E_j^{-\gamma} \exp(-E_j / E_0) \\ \tilde{\mathbf{K}}_{2,j} &= -CE_j^{-\gamma} \exp(-E_j / E_0) \ln E_j \\ \tilde{\mathbf{K}}_{3,j} &= C\left(E_j / E_0\right)^2 E_j^{-\gamma-1} \exp(E_j / E_0). \end{aligned} \tag{38}$$

For the Ellison-Ramaty double power-law representation of the SEP proton spectral flux in equation (7), let the parameter vector be defined as $\mathbf{x} = \left(C, \gamma_a, E_0, \gamma_b\right)^T$. The Jacobian matrix elements for the fit to GOES differential proton flux are:

$$\begin{aligned}
\tilde{\mathbf{K}}_{1,j} &= E_j^{-\gamma_a} \exp(-E_j / E_0) \text{ for } E_j \le \left(\gamma_b - \gamma_a\right) E_0 \\
&= E_j^{-\gamma_b} \left\{ \left[\left(\gamma_b - \gamma_a\right) E_0 \right]^{\left(\gamma_b - \gamma_a\right)} \exp\left(\gamma_a - \gamma_b\right) \right\} \text{ for } E_j > \left(\gamma_b - \gamma_a\right) E_0 \\
\tilde{\mathbf{K}}_{2,j} &= -C E_j^{-\gamma_a} \exp\left(-E_j / E_0\right) \ln E_j \text{ for } E_j \le \left(\gamma_b - \gamma_a\right) E_0 \\
&= -C E_j^{-\gamma_b} \left\{ \left[\left(\gamma_b - \gamma_a\right) E_0 \right]^{\left(\gamma_b - \gamma_a\right)} \exp\left(\gamma_a - \gamma_b\right) \right\} \ln\left[\left(\gamma_b - \gamma_a\right) E_0 \right] \text{ for } E_j > \left(\gamma_b - \gamma_a\right) E_0 \\
\tilde{\mathbf{K}}_{3,j} &= C \left(E_j / E_0\right)^2 E_j^{-\gamma_a - 1} \exp\left(E_j / E_0\right) \text{ for } E_j \le \left(\gamma_b - \gamma_a\right) E_0 \\
&= C E_j^{-\gamma_b} \left\{ \left[\left(\gamma_b - \gamma_a\right) E_0 \right]^{\left(\gamma_b - \gamma_a\right)} \exp\left(\gamma_a - \gamma_b\right) \right\} \left\{ \frac{\left(\gamma_b - \gamma_a\right)}{E_0} \right\} \text{ for } E_j > \left(\gamma_b - \gamma_a\right) E_0 \\
\tilde{\mathbf{K}}_{4,j} &= 0 \text{ for } E_j \le \left(\gamma_b - \gamma_a\right) E_0 \\
&= C E_j^{-\gamma_b} \left\{ \left[\left(\gamma_b - \gamma_a\right) E_0 \right]^{\left(\gamma_b - \gamma_a\right)} \exp\left(\gamma_a - \gamma_b\right) \right\} \ln\left[\frac{\left(\gamma_b - \gamma_a\right) E_0}{E_j} \right] \text{ for } E_j > \left(\gamma_b - \gamma_a\right) E_0.
\end{aligned} \tag{39}$$

For the Weibull representation of the SEP proton spectral flux in equation (8), let the parameter vector be defined as $\mathbf{x} = \left(C, k, \gamma\right)^T$. The Jacobian matrix elements for the fit to GOES differential proton flux are:

$$\begin{aligned}
\tilde{\mathbf{K}}_{1,j} &= k\gamma E_j^{\gamma - 1} \exp\left(-k E_j^{\gamma}\right) \\
\tilde{\mathbf{K}}_{2,j} &= Ck\gamma E_j^{\gamma - 1} \exp\left(-k E_j^{\gamma}\right) \left[\frac{1}{k} - E_j^{\gamma} \right] \\
\tilde{\mathbf{K}}_{3,j} &= Ck\gamma E_j^{\gamma - 1} \exp\left(-k E_j^{\gamma}\right) \left[\frac{1}{\gamma} + \ln E_j - k E_j^{\gamma} \ln E_j \right].
\end{aligned} \tag{40}$$

The convergence of the Marquardt-Levenberg algorithm for the solution of the parameter vector in equation (36) is based on the difference in the chi-square solution residual χ^2 between successive iteration steps (Brandt, 1999). The convergence criterion on the successive chi-square residuals is explicitly

$$\left| \chi_i^2 - \chi_{i-1}^2 \right| < \varepsilon \left| \chi_{i-1}^2 \right| + \delta \tag{41}$$

where $\varepsilon = 10^{-8}$ and $\delta = 10^{-15}$.

The NAIRAS version 3 SEP spectral fitting algorithm fits all four analytical representations of the SEP proton spectrum in equations (5) through (8) using the methodology described in this section. The analytical form that has the minimum chi-square residual out of the four spectral representations is selected as the potential optimal solution spectrum. One further test criterion is applied. If the reduced chi-square residual is less than 1.0, then the selected potential spectrum is

the final optimal solution for the SEP proton spectrum used in the subsequent NAIRAS SEP transport and response function calculations. If the solution spectrum does not pass the final goodness test, the SEP proton spectrum is formed by log-log interpolation and extrapolation of the GOES differential proton flux measurements. A hard limit on the extrapolated flux at high energy is also set. Based on experience and numerous SEP event test cases, if the extrapolated flux at 10 GeV is greater than 10^{-7} $(cm^2\text{-MeV-sr-s})^{-1}$, then the SEP spectral flux is set to a numerically small value at all energies greater than or equal to the highest energy GOES differential proton channel.

The SEP proton spectral fitting approach to GOES integral proton flux measurements is described next. The measurement vector $\mathbf{y}$ is the vector of GOES integral proton flux measurements. The number of GOES integral proton channels used in the SEP proton spectral fit is six or seven, depending on the specific GOES series and its particle flux detector system, with threshold energies between >10 MeV and >700 MeV. The measurement error covariance matrix $\tilde{\mathbf{S}}_{\varepsilon}$ is prescribed by uncorrelated Poisson statistics. The forward model $\mathbf{F}(\mathbf{x})$ is the analytical SEP proton spectral forms in equations (5) through (8) integrated from the threshold energies of the GOES integral proton flux channels to infinity. Thus, the analytical representations of SEP integral proton flux for single power-law, Ellison-Ramaty, Ellison-Ramaty double power-law, and Weibull spectral forms are given, respectively, by

$$J_{SP}(E) = \left(\frac{C}{\gamma - 1}\right) E^{1-\gamma} \tag{42}$$

$$J_{ER}(E) = C E_0^{1-\gamma} \Gamma(1-\gamma, E/E_0) \tag{43}$$

$$\begin{aligned} J_{DP}(E) &= C E_0^{1-\gamma_a} \left[\Gamma(1-\gamma_a, E/E_0) - \Gamma(1-\gamma_a, \gamma_b - \gamma_a)\right] \\ &\quad + \left(\frac{C}{\gamma_b - 1}\right) \left[\left(\gamma_b - \gamma_a\right) E_0\right]^{1-\gamma_b} \left\{\left[\left(\gamma_b - \gamma_a\right) E_0\right]^{(\gamma_b - \gamma_a)} \exp\left(\gamma_a - \gamma_b\right)\right\} \text{ for } E \le \left(\gamma_b - \gamma_a\right) E_0 \\ &= \left(\frac{C}{\gamma_b - 1}\right) E^{1-\gamma_b} \left\{\left[\left(\gamma_b - \gamma_a\right) E_0\right]^{(\gamma_b - \gamma_a)} \exp\left(\gamma_a - \gamma_b\right)\right\} \text{ for } E > \left(\gamma_b - \gamma_a\right) E_0 \end{aligned} \tag{44}$$

$$J_{WB}(E) = C \exp\left(-kE^{\gamma}\right). \tag{45}$$

In equations (43) and (44), $\Gamma(a,x)$ is the complement of the incomplete gamma function, which is defined as

$$\Gamma(a,x) = \int_x^{\infty} t^{a-1} e^{-t} dt. \tag{46}$$

Equation (46) can be expressed in terms of the gamma function and the incomplete gamma function, such that

$$\Gamma(a,x) = \Gamma(a) - \gamma(a,x), \tag{47}$$

where the gamma function and incomplete gamma function are defined by

$$\Gamma(a) = \int_0^{\infty} t^{a-1} e^{-t} dt \quad [\mathrm{Re}(a) > 0] \tag{48}$$

and

$$\gamma(a,x) = \int_0^x t^{a-1} e^{-t} dt \quad [\mathrm{Re}(a) > 0], \tag{49}$$

respectively. The NAIRAS version 3 SEP spectral fitting algorithm uses the computationally efficient numerical algorithms for evaluating the complement of the incomplete gamma function developed by Zhang and Jin (1996), which are based on the relationships in equations (46)-(49). Another property of the complement of the incomplete gamma function important for deriving analytical expressions for the Jacobian matrix is the derivative with respect to its variable argument, which is given by (Zhang & Jin, 1996)

$$\frac{d\Gamma(a,x)}{dx} = -x^{a-1} e^{-x}. \tag{50}$$

Analytical computation of the Jacobian matrix in spectral fitting to GOES integral proton flux measurements is essential to the computational efficiently necessary to fit the SEP proton spectrum at 5-minute time intervals throughout the time evolution of a SEP event. Thus, the Jacobian matrices for the four analytical representations of the SEP integral proton flux are described below.

For the single power-law representation of the SEP integral proton flux in equation (42), let the parameter vector be defined as $\mathbf{x} = \left(C, \gamma\right)^T$. The Jacobian matrix elements for the fit to GOES integral proton flux are:

$$\begin{aligned} \tilde{\mathbf{K}}_{1,j} &= J_{SP}(E_j) / C \\ \tilde{\mathbf{K}}_{2,j} &= -J_{SP}(E_j) \left[\frac{1}{\gamma - 1} + \ln E_j \right] \end{aligned} \tag{51}$$

For the Ellison-Ramaty representation of the SEP integral proton flux in equation (43), let the parameter vector be defined as $\mathbf{x} = \left(C, \gamma, E_0\right)^T$. The Jacobian matrix elements for the fit to GOES integral proton flux are:

$$\begin{aligned} \tilde{\mathbf{K}}_{1,j} &= J_{ER}(E_j) / C \\ \tilde{\mathbf{K}}_{2,j} &= -J_{ER}(E_j) \ln E_0 + \frac{J_{ER}(E_j)}{\Gamma(1-\gamma, E_j / E_0)} \left[\frac{\Gamma(1-\gamma-\Delta\gamma, E_j / E_0) - \Gamma(1-\gamma, E_j / E_0)}{\Delta\gamma} \right] \\ \tilde{\mathbf{K}}_{3,j} &= \left(\frac{J_{ER}(E_j)}{E_0} \right) \left[(1-\gamma) + \frac{\left(E_j / E_0\right)^{(1-\gamma)}}{\Gamma(1-\gamma, E_j / E_0)} \exp\left(-E_j / E_0\right) \right]. \end{aligned} \tag{52}$$

The derivative of the complement of the incomplete gamma function with respect to the parameter argument for the $\tilde{\mathbf{K}}_{2,j}$ elements is computed numerically where $\Delta\gamma = 0.1\gamma$ in the code.

For the Weibull representation of the SEP integral proton flux in equation (45), let the parameter vector be defined as $\mathbf{x} = \left(C, k, \gamma\right)^T$. The Jacobian matrix elements for the fit to GOES integral proton flux are:

$$\begin{aligned} \tilde{\mathbf{K}}_{1,j} &= J_{WB}(E_j) / C \\ \tilde{\mathbf{K}}_{2,j} &= -J_{WB}(E_j) E_j^{\gamma} \\ \tilde{\mathbf{K}}_{3,j} &= -J_{WB}(E_j) k E_j^{\gamma} \ln E_j . \end{aligned} \tag{53}$$

The analytical expression for the Jacobian matrix for the forward model of integral flux of the Ellison-Ramaty double power-law spectral form is quite complex. In fact, the number of evaluations of the complement of the incomplete gamma function and its numerical derivative with respect to the parameter argument offset the computational advantage of an analytical Jacobian matrix evaluation. Thus, for this case the Jacobian matrix is evaluated numerically, which requires a numerical evaluation of the derivative of the forward model with respect to the fit parameters, according to the definition of the Jacobian matrix in equations (34) and (35). The derivative is computed very accurately by employing a Richardson extrapolation technique, which successively reduces term-by-term the truncation error (Hildebrand, 1974). Note, the evaluation of the forward model is still computed using the analytical representation in equation (44). The convergence criterion of the numerical calculation of the Jacobian matrix elements is

$$\left|\Delta\tilde{\mathbf{K}}_{i,j}\right| \le \varepsilon \text{ or } \left|\Delta\tilde{\mathbf{K}}_{i,j}\right| \le \delta\left|\tilde{\mathbf{K}}_{i,j}\right| \tag{54}$$

where $\varepsilon = 10^{-10}$ and $\delta = 5\text{x}10^{-8}$. In the equation (54), $\Delta\tilde{\mathbf{K}}_{i,j}$ is the difference in the numerical computation of the Jacobian matrix element between successive iterations in the Richardson extrapolation method (cf., Brandt, 1999).

Analogous to SEP spectral fitting to the GOES differential proton flux channels, the NAIRAS version 3 algorithm fits all four analytical representations of the SEP proton spectrum in equations (5) through (8) to the GOES integral proton flux channels using the approach described in the previous paragraphs. The analytical form that has the minimum chi-square residual out of the four spectral representations is selected as the potential optimal solution for the SEP proton spectrum. An additional goodness criterion is applied. If the reduced chi-square residual is less than 1.0, then the selected potential spectrum is the final optimal solution for the SEP proton spectrum used in the subsequent NAIRAS SEP transport and response function calculations. If the solution spectrum does not pass the final goodness test, the SEP proton spectrum is approximated using an integral flux derivative approach.

The integral flux derivative approach is described as follows. The GOES integral proton flux measurements are spline interpolated to a high-resolution energy grid (20 points per decade in energy). Numerical first-order derivatives of the integral flux data are computed on the high-resolution energy grid to convert integral flux to differential (spectral) flux. A box car smoothing is applied to remove numerical ringing from the derivative calculation. The calculated spectrum is then interpolated to the (courser) internal NAIRAS SEP transport energy grid. As a standalone method, this approach is accurate and robust for large SEP events, as verified by comparisons of the derived SEP proton spectrum from this approach with the GOES differential proton flux measurements. The disadvantage of this approach is that it does not permit estimates of solution

error characteristics like the Bayesian statistical inverse method does. On the other hand, from numerous SEP event test cases spanning the range of quiet conditions (no SEP) to weak and strong SEP events, one of the four analytical representations of the SEP proton spectrum in equations (5) through (8) has never failed to meet the convergence and goodness criteria described in this Appendix when fitting to the GOES integral proton flux measurements.

REPORT DOCUMENTATION PAGE

Form Approved
OMB No. 0704-0188

1. REPORT DATE *(DD-MM-YYYY)*	2. REPORT TYPE	3. DATES COVERED *(From - To)*
10/02/2024	Technical Memorandum	

4. TITLE AND SUBTITLE
Commercial Crew Program (CCP) Post-flight Reference Radiation Environments

5a. CONTRACT NUMBER

5b. GRANT NUMBER

5c. PROGRAM ELEMENT NUMBER

6. AUTHOR(S)
Mertens, Christopher J.; Gronoff, Guillaume P.; Zheng, Yihua; Buhler, Janessa; Willis, Emily; Petrenko, Maksym; Phoenix, Daniel; Didigu, Chinwe; Jun, Insoo; Minow, Joseph I.

5d. PROJECT NUMBER

5e. TASK NUMBER

5f. WORK UNIT NUMBER
869021.01.23.01.01

7. PERFORMING ORGANIZATION NAME(S) AND ADDRESS(ES)
NASA Langley Research Center
Hampton, VA 23681-2199

8. PERFORMING ORGANIZATION REPORT NUMBER
NESC-RP-19-01468

9. SPONSORING/MONITORING AGENCY NAME(S) AND ADDRESS(ES)
National Aeronautics and Space Administration
Washington, DC 20546-0001

10. SPONSOR/MONITOR'S ACRONYM(S)
NASA

11. SPONSOR/MONITOR'S REPORT NUMBER(S)
NASA/TM-20240012670

12. DISTRIBUTION/AVAILABILITY STATEMENT
Unclassified - Unlimited
Subject Category Space Radiation
Availability: NASA STI Program (757) 864-9658

13. SUPPLEMENTARY NOTES

14. ABSTRACT
The Nowcast of Aerospace Ionizing RAdiation System (NAIRAS) model version 3 is a coupled physics-based model that transports ionizing radiation through the heliosphere, Earth's magnetosphere, the neutral atmosphere, and aircraft and spacecraft shielding. Ionizing radiation sources included in the model are: 1) galactic cosmic rays, 2) solar energetic particles including protons and heavy ions, and 3) the inner radiation belt trapped protons and electrons. NAIRAS predicts dosimetric quantities and differential and integral flux and fluence quantities for assessing human radiation exposure and single event effects in vehicle electronic systems from the Earth's surface to the space environment.

15. SUBJECT TERMS
Space Radiation; Atmospheric Radiation; Real-Time; Flight Environment; NAIRAS; Solar Particle Event; Galactic Cosmic Ray; Trapped Radiation

16. SECURITY CLASSIFICATION OF:			17. LIMITATION OF ABSTRACT	18. NUMBER OF PAGES	19a. NAME OF RESPONSIBLE PERSON
a. REPORT	b. ABSTRACT	c. THIS PAGE			STI Help Desk (email: help@sti.nasa.gov)
					19b. TELEPHONE NUMBER *(Include area code)*
U	U	U	UU	81	(443) 757-5802